Quantum gate optimisation in stoichiometric rare-earth ensembles

Matthew Pearce

A thesis submitted for the degree of
Master of Philosophy at
The Australian National University

August 2022

Declaration

This thesis is an account of research undertaken between August 2016 and December 2021 at The Department of Physics, Research School of Physics, The Australian National University, Canberra, Australia.

Except where acknowledged in the customary manner, the material presented in this thesis is, to the best of my knowledge, original and has not been submitted in whole or part for a degree in any university.

Matthew Pearce
January, 2022

Acknowledgments

Firstly, I would like to thank my primary supervisor Matt Sellars. His insight and guidance over the past five years has been invaluable.

Secondly, I would like to thank Rose Ahlefeldt for the time and energy that she devoted to this project. This thesis would not have been possible with her countless hours dedicated to helping with experiments and critiquing my writing over its many iterations.

I would be remiss not to mention the contribution of the Laser Physics technical staff, John Bottega and Craig Macleod. Their technical expertise and the equipment constructed over the course of this degree were of immeasurable assistance.

Thank you to all the past and present research students and postdoctoral researchers whom I had the pleasure of overlapping with in the Rare Earth Group: Adam, Charlotte, Grace, James, Kate, Kieran, Matt, Miloš, Morgan and Paul. It has been a delight working with all of you over the course of this work.

Finally, I would like to thank my friends and family for their endless support and encouragement that they have given me over the course of this project.

Abstract

This thesis is an investigation into implementing quantum computing in stoichiometric rare-earth systems, with the crystal $EuCl_3 \cdot 6D_2O$ used as an example system.

In a stoichiometric satellite system, a crystal stoichiometric in one rare-earth species is doped with a second rare-earth. The ions around a dopant experience shifts in their optical and hyperfine transition frequencies uniquely determined by their location relative to the dopant. This creates an ensemble of identical spin clusters with strong and consistent local interactions between ions in spin clusters. Ensembles of ions in the unique positions around the dopant can be used as qubits, enabling the creation of small quantum systems of 5-10 high-quality qubits for use in a small quantum processor.

This thesis investigates the conditions necessary for implementation of a quantum processor in $EuCl_3 \cdot 6D_2O$ and other stoichiometric rare-earth systems. The primary factors explored in this thesis are the manipulation of system parameters and the implementation and optimisation of quantum gates in $EuCl_3 \cdot 6D_2O$ to minimise gate error.

The quantum gate error of $EuCl_3 \cdot 6D_2O$ with Gaussian pulse shapes was first explored. It was determined that the oscillator strengths of $EuCl_3 \cdot 6D_2O$ are too unequal to be able to perform low error quantum operations at zero-field. The use of applied magnetic fields to manipulate the oscillator strengths and hyperfine splittings of $EuCl_3 \cdot 6D_2O$ was explored. It was found that broad magnetic field regions exist in which the parameters of $EuCl_3 \cdot 6D_2O$ can be manipulated to be closer to an ideal Λ system. Through the application of an 8T field, it was found that a three-qubit bit-flip error correction sequence could potentially be implemented with an error as low as 0.022.

The optimisation of the optical pulses used to perform quantum gates in $EuCl_3 \cdot 6D_2O$ was investigated. It was determined that standard Gaussian pulses were sufficient to perform gates of a sufficiently low error for quantum error correction. Simulations of a NOT gate on an inhomogeneously broadened ensemble were performed with both a compensated pulse sequence and direct rotations. It was determined that compensated pulses do not reduce gate error over direct pulses in $EuCl_3 \cdot 6D_2O$. The use of arbitrary pulse shapes was investigated and it was determined that a reduction of approximately 37% in gate error could be achieved by using optimised pulses of arbitrary shape.

It was determined that the quantum gate error in europium systems is fundamentally limited by the size of the europium hyperfine splittings relative to the optical coherence time. The rare-earth species erbium and holmium were proposed for computing due to their large hyperfine structure, and it was established that there is potential for up to a 100-fold reduction in quantum gate error by moving to these host ions.

Contents

Chapter 1

Introduction

Quantum mechanics began as a field in the late 19th century with work such as Kirchoff's 1859 description of the Blackbody effect [1], Boltzmann's 1877 hypothesis about discrete states of physical systems[2] and Hertz's 1887 discovery of the photoelectric effect [3]. In the early 20th century, the groundwork of quantum theory was laid with results such as Planck's 1900 quantum hypothesis [4], Einstein's 1905 explanation of the photoelectric effect [5] and de Broglie's 1923 theory of wave-particle duality [6–8]. As the framework for quantum theory started to take shape, it became clear that quantum systems exhibit unique phenomena that have no classical analogues: such as quantum superposition where a system inhabits multiple states simultaneously, or entanglement where system states can be correlated in ways that classical physics is unable to explain.

In 1982, Richard Feynman first proposed the use of quantum mechanical effects to perform computations that would be intractable on a classical computing architecture [9]. In the paper, he discusses the idea of a *universal quantum simulator* that would use quantum phenomena to simulate quantum systems. This idea remained an interesting curiosity for several years, as it was thought that any non-trivial use of quantum effects would require infeasibly low error rates. Quantum computing was truly born as a field with the publication of two papers by Peter Shor. In 1994 he showed that a quantum computer could efficiently find prime factors (with complexity $\mathcal{O}((\log N)^2(\log\log N)(\log\log\log N))$), a problem that is intractable for large numbers on a classical computer [10]. In 1995 he addressed the problem that had been thought to render quantum computing impossible, showing that it was possible to create quantum error-correcting codes, allowing for arbitrarily long quantum computations [11]. In the time since these foundational papers, there have been several areas that have been identified as benefiting from quantum information, such as provably secure communication, finding prime factors [12, 13] and database searching [14].

Applying quantum computing to problems with practical application requires large numbers of qubits, far beyond what has been demonstrated to date. In order to scale quantum computing to the required numbers of qubits, it is necessary to be able to reliably correct errors in the computing system. To date, there has been no demonstration of full quantum error correction (QEC) and even small quantum computing systems have high error rates [15, 16]. Reliable error correction will require knowledge of the kinds of errors that occur to qubits. A small quantum processor

with a low error rate would be a useful tool for studying the effect of real-world errors on error correction. These errors may be correlated between qubits, a circumstance that current error correction implementations cannot account for. For the application of studying the nature of system errors, such a system does not need to be scalable — the primary concern with such a system is the error rate when performing quantum operations.

Rare-earth ion systems are one potential candidate for the construction of such a small quantum processor. The rare-earths have long coherence times, allowing for the storage of quantum states for a long time and it is possible to perform low error quantum operations [17–20]. These are both properties desirable for a small quantum processor. In addition, rare-earth devices are compatible with existing telecommunication technologies.

This thesis is a description of how quantum operations for quantum computing could be performed on rare-earth systems and in particular $EuCl_3 \cdot 6D_2O$. In particular, the experimental parameters needed to perform controlled gates on two and three-qubit rare-earth satellite systems are outlined, with a view towards the use of this system for quantum error correction.

$EuCl_3 \cdot 6D_2O$ was chosen as an example system due to its low inhomogeneous linewidth and its large number of potentially addressable rare-earth ion qubits. This material was previously characterised in [21]. The conclusions reached for $EuCl_3 \cdot 6D_2O$ serve as a guide for the performance in rare-earth systems and the areas that should be focused on to decrease error in these systems. To date, $EuCl_3 \cdot 6D_2O$ is the only stoichiometric rare-earth system in which implementing quantum gate operations has been researched and it is possible that other crystals will be more suited for quantum computing applications.

1.1 Quantum computing

As with classical computing, a quantum computer operates on a basis of states $\{|0\rangle, |1\rangle\}$. The fundamental difference between quantum and classical computing is that the quantum unit of information (the qubit) is not restricted to being $|0\rangle$ or $|1\rangle$ but can exist as a superposition $A|0\rangle + Be^{i\phi}|1\rangle$ of the two states, as displayed in Figure 1.1. Due to the existence of superposition states, an N-qubit quantum computer operates on a 2^N dimensional Hilbert space. Due to this, it quickly becomes intractable to simulate quantum computing on a classical computer.

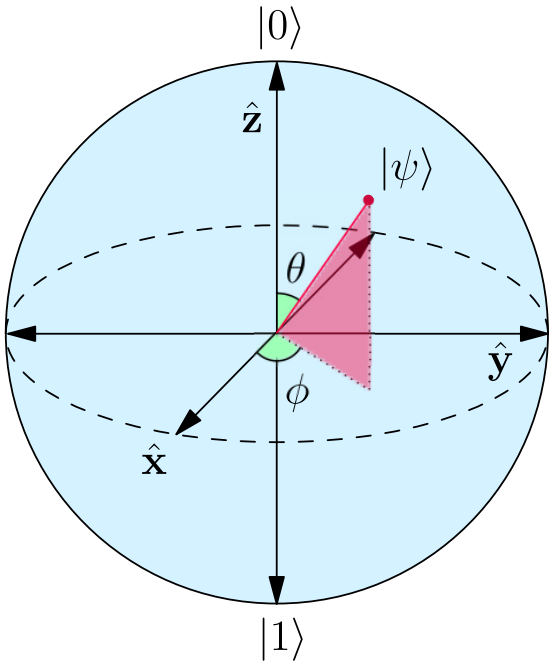

Figure 1.1: The Bloch sphere representation of a quantum state $|\psi\rangle = A|0\rangle + Be^{i\phi}|1\rangle = \cos\left(\frac{\theta}{2}\right)|0\rangle + e^{i\phi}\sin\left(\frac{\theta}{2}\right)|1\rangle$, where A, B and ϕ are real numbers with $\|A\|^2 + \|B\|^2 = 1$. The displayed Bloch vector representation of this state is obtained by taking ϕ as the azimuthal angle for a spherical representation and θ as the polar angle, yielding Bloch vector $(u, v, w) = (\sin(\theta)\cos(\phi), \sin(\theta)\sin(\phi), \cos(\theta))$.

The requirements for the construction of a quantum computer are given by the DiVincenzo criteria, discussed in Chapter 3. Of relevance to the current discussion is that a general-purpose quantum computer needs some way of scaling qubit number, while still having the qubits behave in a predictable fashion. Without this property, the error in a quantum computer quickly becomes too high to allow for useful calculations.

1.1.1 Contemporary implementations of quantum computing

There are several quantum computing systems currently in active development, with examples including superconducting microwave systems, ion traps and spin qubits in silicon. At the time of writing, the system with the most well-developed architecture was superconducting microwave qubits, with quantum supremacy recently demonstrated in a 54-qubit superconducting system [15]. Superconducting qubits consist of circuits of type-II superconducting material, with the quantisation of magnetic flux used to create qubits and qubit interactions mediated by microwave fields.

The microwave superconducting system is currently well-positioned to enter the Noisy Intermediate Scale Computing (NISQ) regime [22], with low error single-qubit and multi-qubit gates [23], well-characterised qubits and the ability to currently scale to moderate numbers of qubits [15]. Small quantum algorithms [24, 25] have been implemented in such systems along with basic error correction demonstrations

[26–28].

Despite the success of superconducting computing systems for qubit numbers up to $\mathcal{O}(50)$ qubits, scaling such systems past this has proven problematic to date. One of the major issues preventing scaling of superconducting qubit systems is crosstalk between qubits, where manipulating the state of one qubit inadvertently changes the state of nearby qubits. For low qubit numbers, the effects of crosstalk can be mitigated by characterising the dynamics of the entire system and tuning gates to minimise error. This has allowed gate fidelities high enough to perform simple calculations in such systems. As the qubit number is increased, the system errors can become sufficiently complicated such that the system can not be fully characterised and the gate fidelities decrease to an unacceptable level, which has prevented scaling of microwave systems past 100 qubits to date. Error correction protocols in which correlated errors could be accounted for would help to mitigate the effects of qubit crosstalk and potentially allow microwave computing systems to be scaled to greater numbers of qubits.

1.2 Rare-earth quantum computing

Rare-earth ions in solids have long coherence times on both optical and spin levels at cryogenic temperatures, with coherence times up to 6 hours having been previously realised [29]. Rare-earth based systems are well established as quantum memories [30] and quantum sources [31]. To date, there has been much less investigation of their use as a computing platform.

This work concerns an ensemble rare-earth system, with properties uniquely suited for the creation of a small quantum processor. The system is briefly described in Figure 1.2. The hyperfine qubit states can be addressed using an auxiliary optical transition, allowing for read-in and read-out of optical photons in this system. Additionally, ensemble rare-earth systems have a strong optical coupling due to the high optical depth, making them exemplary systems for quantum memories.

As stated earlier, qubit-qubit crosstalk is a major problem in quantum computing systems, causing decoherence and gate-errors. In a rare-earth satellite system, the hyperfine transitions experience minimal perturbation due to excitation of surrounding qubits [32], so unless performing a controlled gate, the state of one qubit has a minimal effect on the behaviour of other qubits. Due to this, crosstalk between qubits is minimal. Having an inherently low crosstalk system with a controllable interaction between qubits allows for crosstalk to be induced between qubits to study error correction algorithms under different regimes.

Despite these advantages over other computing systems, the ensemble rare-earth satellite system is currently unsuitable as a general-purpose computing system as it is limited to $5-10$ qubits. Distinct qubits are created from the optical shifts of a dopant ion, limiting the sites that can be addressed to the $\mathcal{O}(20)$ sites close to the dopant. The need to perform spectral preparation on qubits then further reduces the number of usable qubits to $5-10$.

The potential for being able to perform high fidelity quantum gates in a quantum

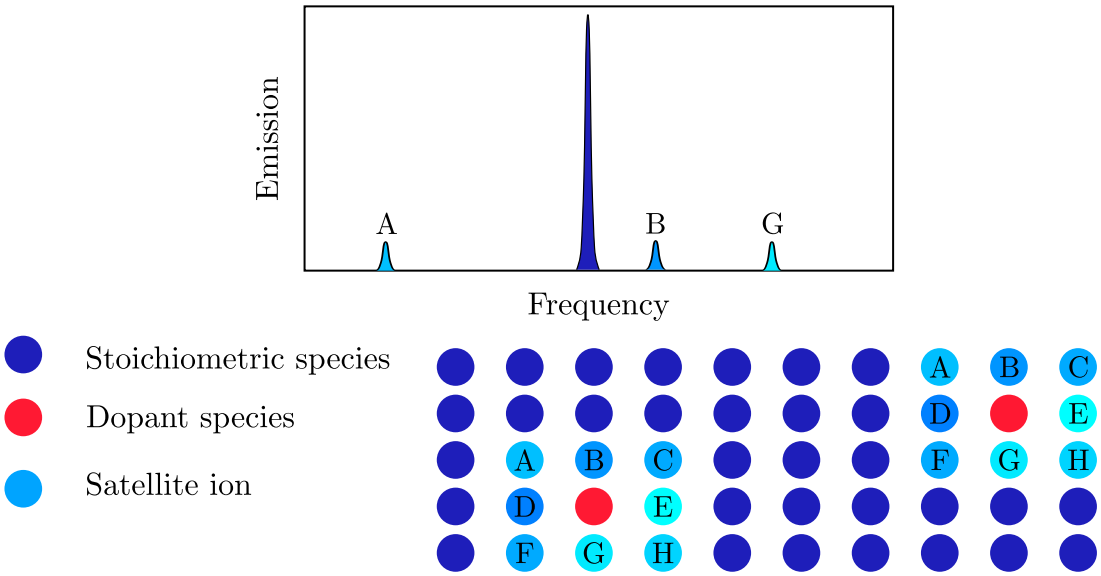

Figure 1.2: The rare-earth satellite system. A crystal stoichiometric with the computing rare-earth element (dark blue) is dilutely doped with a second rare-earth (red). The transitions of the ions around the dopant (light blue) are perturbed, allowing them to be addressed separately from the bulk, as shown in the example spectrum. This is an ensemble system, so every satellite qubit consists of multiple ions from different spin clusters distributed across the crystal. Satellite ions have a consistent position in each spin cluster and so the interaction strength between satellite ions is consistent across the ensemble.

system with minimal crosstalk and a strong optical coupling makes this an attractive system for tests of quantum protocols and use in quantum information networks, despite this inherent lack of scalability. The attributes of this class of quantum systems are given in greater detail in Section 4.

Schemes for quantum computing in rare-earth materials date back to the early 2000s [33] with proposals for the use of doped systems. The most complete demonstration of quantum computation in a rare-earth system was performed by Longdell in 2003 [34], where a two-qubit system was created and a low-fidelity CROT gate implemented. There have been further proposals on the implementation of high fidelity gates in such systems [35]. There are currently no demonstrations of quantum operations in a rare-earth satellite system.

The optical frequency shifts on nearby satellite ions from optical excitation of satellite sites in $EuCl_3{\cdot}6D_2O$ were measured in [21], allowing for the potential implementation of controlled quantum gates in this system with an appropriate experimental setup. In this work, I explore the experimental parameters needed to implement quantum logic in a rare-earth satellite system and how error correction could be implemented in such a system.

1.3 Direction taken in this thesis

Efficient implementation of quantum operations, whether for quantum computing or communication, requires that we have the ability to manipulate quantum states with a low error rate. There are several factors that must be considered in order to minimise gate error, which can be divided into the following groups:

Energy level structure:
Gates in this system are performed via an auxiliary optical transition, which has a coherence time short ($\mathcal{O}$(1ms)) compared to achievable hyperfine coherence times ($\mathcal{O}$(hours)). The short relative coherence time of the optical transition means that gates must be performed rapidly enough that we do not see significant decoherence. Balancing this consideration is that there are additional hyperfine levels near the levels used as computing states, in order to minimise gate error excitation to both these levels and the other hyperfine level must be minimised. This limits the maximum Rabi frequencies that can be used when driving the system.

Inhomogeneities:
The rare-earth satellite system is an ensemble system and as with all ensemble systems, inhomogeneities limit the system quality. There are two major sources of inhomogeneity in this system: inhomogeneous broadening of the qubit optical transitions and spatial inhomogeneity. The inhomogeneous broadening of the optical transition causes each ion to be driven at a slightly different rate by applied pulses, creating errors. The crystals used for these experiments are macroscopic, so ions at different spatial positions will experience a different pulse intensity. Additionally, the pulse will be absorbed as it propagates through the sample, decreasing the pulse intensity.

Experimental considerations:
In constructing an experiment to implement quantum logic into these systems, the practical realities of experimental setups must also be considered. We can subdivide such considerations further into two categories, those affecting gate fidelity and those affecting measurement fidelity. Gate fidelity is affected by errors in pulses applied to the system. The ability to differentiate signals from our ensemble over background noise limits the minimum signal from the ensemble. As the signal from the ensemble decreases closer to the measurement floor of the detection scheme used, the measurement fidelity will decrease. This limits the minimum ensemble sizes that can be used.

In general, these considerations are conflicting. For example, a small ensemble size will reduce the effect of inhomogeneities but must be balanced by the need for the ensemble to be still detectable. To maximise the performance of a quantum system, it is necessary to balance the relative errors due to all of the different parameters of the system, while remaining in a regime that is feasible to prepare and read-out in a realistic experimental setup.

This thesis focuses on implementing quantum experiments in rare-earth satellite systems, with $EuCl_3{\cdot}6D_2O$ as an example system. Necessary parameter regimes in order to implement high fidelity quantum operations are discussed, with the possible applications for different levels of system quality discussed. This is considered in the context of a quantum computer, where the initial quantum state is prepared in the quantum system. The parameter regime required for a quantum computer is different from that of a quantum memory, where the initial state is a weak optical pulse read into the system. This thesis will not consider the parameters required for a quantum memory.

1.4 Outline of the thesis

Chapter 2 first gives a brief introduction to the properties of the rare-earth materials relevant to this thesis. It focuses on the factors affecting rare-earth coherence times, level structure and inhomogeneous broadening. The specific properties of europium and the crystal $EuCl_3{\cdot}6D_2O$ are detailed. The chapter concludes with a discussion on ensemble quantum systems and similar systems to rare-earth satellite systems.

Chapter 3 introduces the concepts relevant to quantum computing. The basic properties of a quantum computer are detailed and the idea of a quantum gate is introduced, with notable examples given. The chapter finishes with an introduction to the concept of quantum error correction in single-instance and ensemble computing schemes.

Chapter 4 is concerned with the implementation of quantum computing in rare-earth systems and what has been achieved in previous work. The problems inherent to quantum computing in the doped rare-earth systems and the rare-earth satellite systems are detailed in this chapter.

In the remaining chapters, the optimisation of the $EuCl_3{\cdot}6D_2O$ system and rare-earth satellite systems, in general, are explored. The optimisation of the parameters of the crystal system is first discussed, followed by optimisation of the optical pulses used to implement gates.

Chapter 5 describes the manipulation of system parameters to improve the performance of gates in rare-earth systems. The performance of $EuCl_3{\cdot}6D_2O$ at zero-field is first discussed, followed by the results of simulations at an applied field to find points in which a lower gate error can be achieved. The nature of low error regions in this system is then discussed. The chapter concludes with a discussion on potential other rare-earth systems with more favourable parameters.

Chapter 6 explores the optimisation of the optical pulses used to perform gates in rare-earth crystal systems. The factors affecting pulse performance are first discussed, along with a comparison of the performance of pulse shapes commonly seen in the literature. This is followed by an investigation into the use of arbitrary pulse shapes and the regimes in which different forms of pulses are optimal.

Chapter 2

Rare-earth ion ensembles

This chapter introduces the properties of the rare-earth materials relevant to this thesis and the concept of ensemble quantum computing. The chemistry of the rare-earth ions, along with the origin of their coherence times and level structure, is first discussed. The concept of an ensemble quantum computer is then introduced and the properties of the europium ion and the $EuCl_3 \cdot 6D_2O$ system are described. The chapter concludes with a comparison between rare-earth satellite systems, nitrogen-vacancy (NV) and liquid-state nuclear magnetic resonance (NMR) systems as candidate technologies for quantum computing.

2.1 Chemical Properties

The rare-earths are a group of elements consisting of the lanthanides, yttrium and scandium. These elements are metals with a distinctive set of chemical and physical properties, which make them particularly attractive for quantum information applications. In solids, the rare-earths are strongly electro-positive and are generally found in a 3+ oxidation state. The electronic configuration of the lanthanides is $[\mathrm{Xe}]4f^n$ where $0 \leq n \leq 14$. The $5s$ and $5p$ shells extend further from the nucleus than the $4f$ electrons, as shown in Figure 2.1, shielding these electrons from the surrounding environment. The electronic structure of the rare-earths is the origin of the insensitivity to environmental noise in crystalline form and similar chemical properties.

Although the $4f$ electrons are well shielded from the environment, they are not well shielded from the nucleus. Due to this, there is a steady decrease in radius with nuclear charge in the lanthanides, resulting in an approximately 20% decrease in radius across the lanthanide series. The differences in rare-earth chemistry are largely a result of this difference in bonding radius. We use this difference in rare-earth radius to generate satellite lines by doping a stoichiometric rare-earth crystal with a second rare-earth, thereby distorting the local crystalline structure, as detailed in Section 2.5.

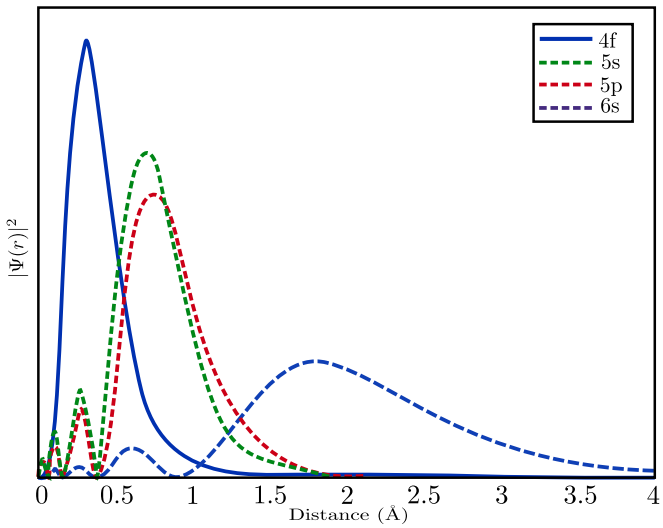

Figure 2.1: Radial electron probability for Pr^{3+}. Figure reproduced from [36].

2.2 4f energy levels

For quantum information applications, the transitions of interest are those between the $4f$ levels. Solving the Schrödinger equation for a multi-electron system is not possible; however, due to the shielding from the $5s$ and $5p$ shells, the Hamiltonian of $4f$ electrons in solids is very similar to the free-ion Hamiltonian. To approximate the Hamiltonian of the $4f$ levels, the free-ion Hamiltonian is used to describe the electron-nucleus, electron-electron and spin-orbit interactions and the remaining effects due to the crystal field are treated as a perturbation to this Hamiltonian.

The largest contribution to the free-ion rare-earth Hamiltonian comes from the electron-nucleus interaction and the central part of the electron-electron Coulomb repulsion. Under the influence of just these terms, the $n = 4$ levels are degenerate. The next most significant term in the rare-earth Hamiltonian is the non-central electron-electron Coulomb repulsion, which lifts the n degeneracy. The spin-orbit interaction removes some of the degeneracy of the $4f$ levels by mixing states of different L and S quantum numbers. The perturbation to the free-ion Hamiltonian from the crystal field contribution acts to further lift the $2J + 1$ degeneracy left in the free-ion Hamiltonian. The degree to which the remaining degeneracy is lifted depends on the crystal site symmetry and whether the ion has an odd number of electrons (a Kramers ion). For non-Kramers ions with sites of less than axial symmetry, the electronic states are singlets. This is the case for Eu^{3+} in $EuCl_3{\cdot}6H_2O$. In Kramers ions such as erbium, the J levels remain at least two-fold degenerate after accounting for the crystal field. The magnitudes of the contributions to the rare-earth Hamiltonian are displayed in Table 2.1.

The resulting energy level structure from the free ion and crystal field Hamiltonians is shown in a Dieke diagram in Figure 2.2. This diagram is for $LaCl_3$; however, the structure is very similar in other crystal hosts.

Table 2.1: Scale of the contribution to the Hamiltonian for rare-earth ions in crystal hosts [37].

Interaction mechanism	Energy splitting (cm^{-1})
Electron-nucleus and central electron-electron	10^5
Non-central Coulomb	10^4
Spin-orbit interaction	10^3
Crystal field	10^2
Hyperfine splitting (nuclear spin)	$10^{-1} - 10^{-3}$
Superhyperfine splitting (ion-host nuclear spin)	$10^{-2} - 10^{-4}$

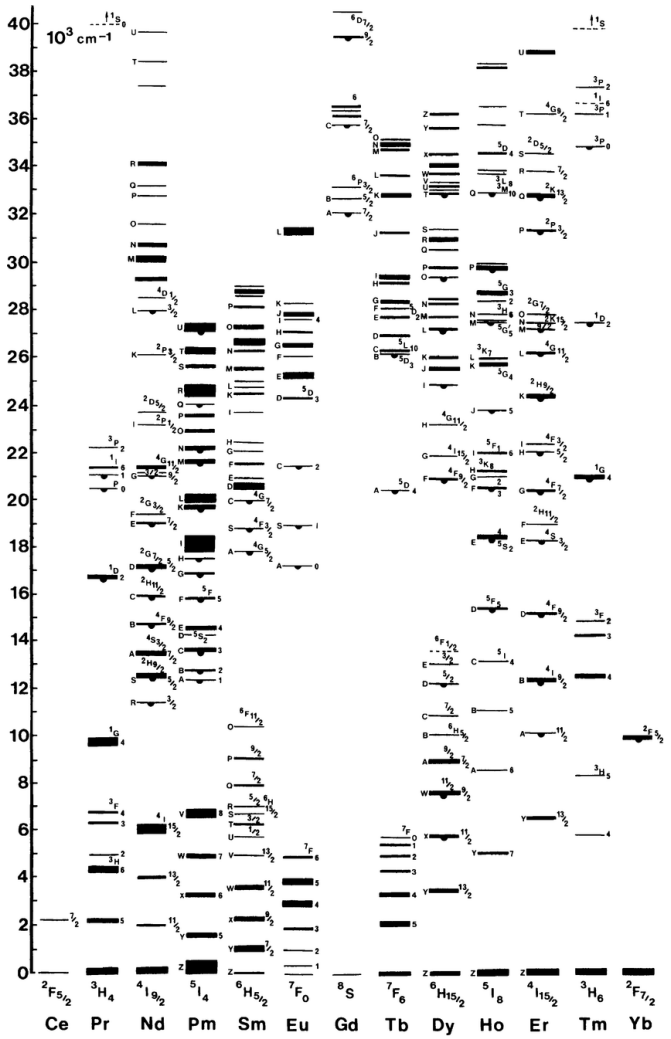

Figure 2.2: Dieke diagram of the energy levels of RE^{3+}:$LaCl_3$ from [38]. The crystal field levels are not resolved in this diagram and are indicated by the line thickness.

2.3 Rare-earth crystal Hamiltonian

There are a number of interactions that further split the crystal field levels into hyperfine structure. For the purposes of describing rare-earth hyperfine structure, the Hamiltonian of the rare-earth ions is usually written in the form of Equation 2.1.

$$H = H_{FI} + H_{CF} + (H_{HF} + H_Q + H_z + H_Z), \tag{2.1}$$

where H_{FI} is the free ion Hamiltonian, H_{CF} the crystal field, H_{HF} is the hyperfine interaction, H_Q the nuclear electric quadrupole, H_z is the nuclear Zeeman interaction and H_Z the electronic Zeeman interaction. The H_{FI} and H_{CF} Hamiltonians are used to characterise the electronic levels, with the remaining four terms treated as a perturbation on these levels.

To simplify analysis of the perturbation on the free-ion Hamiltonian, the mixing of L and S by the spin-orbit interaction and the J mixing by the crystal field is assumed to be small. Under this assumption, the energy levels are labelled using L, S and the total angular momentum J.

2.4 Inhomogeneous broadening

In any rare-earth crystal, there will inevitably be imperfections in the crystal lattice, resulting in variation in the strain, electric and magnetic fields experienced by a given ion in the crystal. The homogeneous linewidths of rare-earth optical transitions and hyperfine transitions can be sub-kilohertz at low enough temperatures. However, variation in the local environment means that ensemble (inhomogeneous) linewidths are much larger, with hyperfine linewidths of tens of kilohertz and optical linewidths varying from 10 MHz to over 100 GHz in different materials. This process of broadening due to crystal imperfections is shown in Figure 2.3.

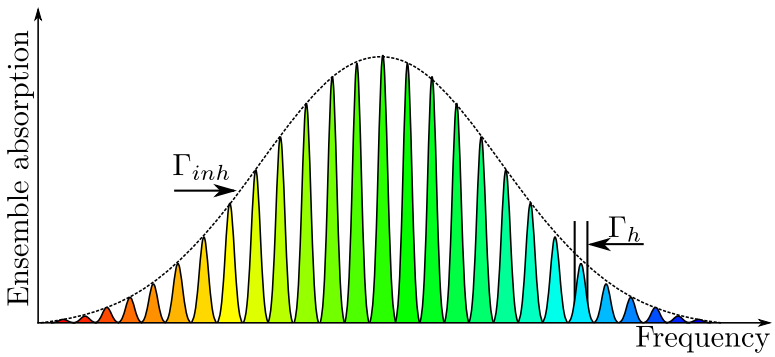

Figure 2.3: Inhomogeneous absorption profile of an ensemble of rare-earth ions in a crystal. The inhomogeneous line is the sum of the homogeneous profiles of rare-earth ions with different local environments due to crystal imperfections.

2.5 Satellite lines

Inhomogeneous broadening arises from the sum of frequency shifts from many defects distant from the ion of interest. Defects close to ions create satellite lines: a close defect causes a large local perturbation and shifts the site frequency outside of the main inhomogeneous line. Rare-earth ions with the same relative position to an identical defect contribute to the same satellite line, with each satellite line structure having the same lineshape as the main inhomogeneous line. The presence of satellite lines detuned by gigahertz to terahertz from the main inhomogeneous line is relatively common in rare-earth crystals [39–42].

Figure 2.4 is an example of the satellite structure created by these close defects, in the $^7F_0 \rightarrow ^5D_0$ transition of Eu^{3+}: Y_2O_3.

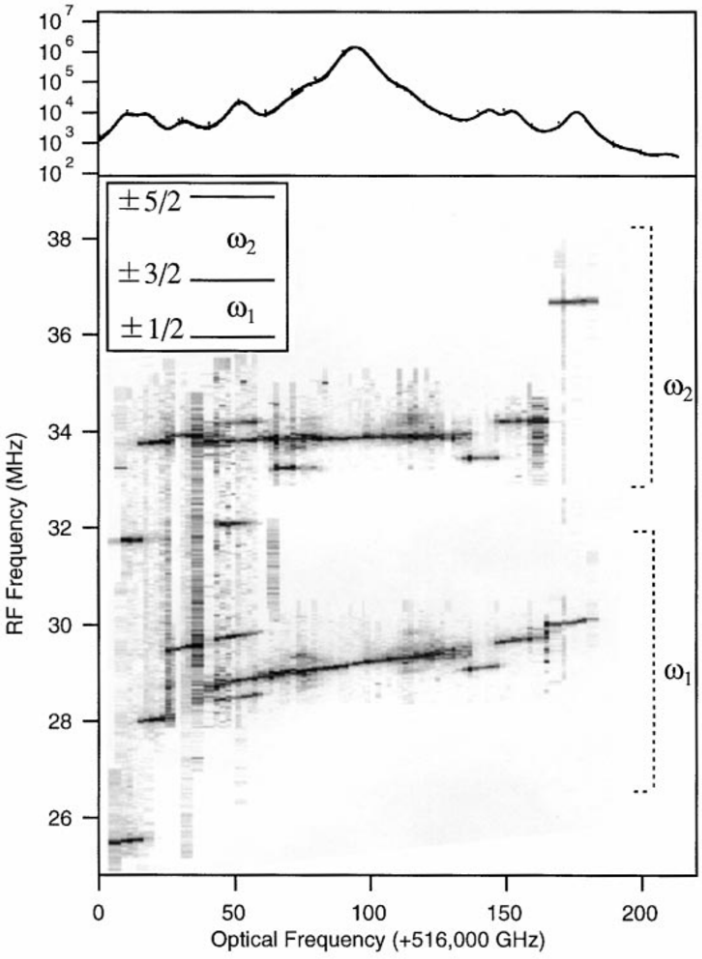

Figure 2.4: Double resonance excitation spectrum of the $^7F_0 \rightarrow ^5D_0$ transition of Eu^{3+}: Y_2O_3 [42]. The dark lines correspond to resonances of crystal satellite lines. Reprinted from Journal of Luminescence , Vol 87-89, M. Yamaguchi, K. Koyama & T. Suemoto. Three-parameter mapping of site distribution by optical-RF double resonance in Eu^{3+}: Y_2O_3 crystals, pp. 1099-1101. Copyright 2000, with permission from Elsevier.

In general, there is not a fixed spatial relationship between ions in different satellite lines as they may be generated from different defects. Additionally, for defects arising from crystal impurities and lattice defects, the number of ions contributing to each satellite line will vary between crystals. It is possible to induce consistent satellite structure with a fixed spatial relationship between sites by lightly doping a rare-earth crystal with a substitutional defect, such as a second rare-earth species. There is a size mismatch between the dopant and host ions, causing distortion of the crystal field at the nearby lattice sites and shifting their optical and hyperfine transition frequencies outside of the main inhomogeneous line.

Many satellite lines are well resolved from both the main inhomogeneous line and other satellite lines. This allows the optical and RF transitions of specific satellite ions to be addressed. Due to this, the standard quantum operations performed on the main inhomogeneous line can also be performed on specific satellite lines, thus allowing their use as qubits. The ions around a dopant are an example of a *spin cluster* system, in which the individually addressable spins are spatially distributed such that quantum operations can be performed between them. Figure 2.5 displays an example of the satellite structure created by this light doping.

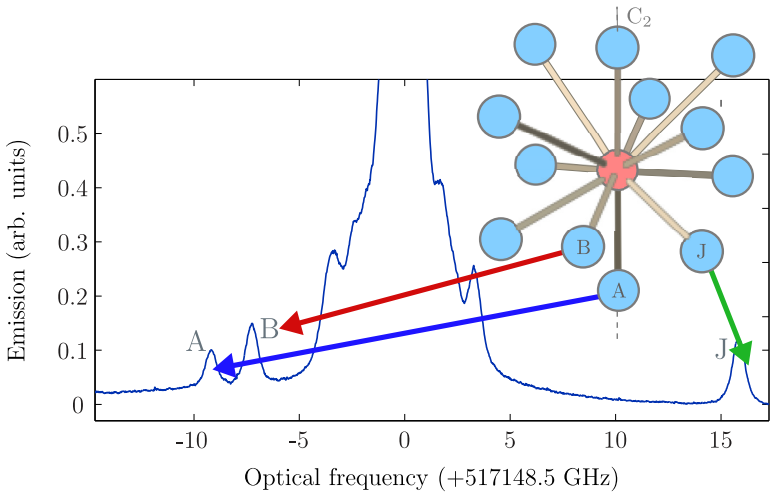

Figure 2.5: Satellite line structure in $EuCl_3{\cdot}6H_2O$ caused by doping the crystal with 1% La^{3+}. The inset diagram shows the relationship between the spatial position relative to the dopant ion and the satellite frequency for a select group of satellite lines.

In previous rare-earth crystal systems studied for quantum information, a crystal stoichiometric in one rare-earth species is doped with a second rare-earth ion, with the doped species then used as the quantum resource. The satellite system is the opposite approach in a sense, with the crystal stoichiometric in the species to be used for quantum operations and the dopant species used to create isolated clusters in the crystal. Figure 2.6 gives an illustration of the differences between the traditional doped rare-earth crystal system and a satellite spin-cluster system.

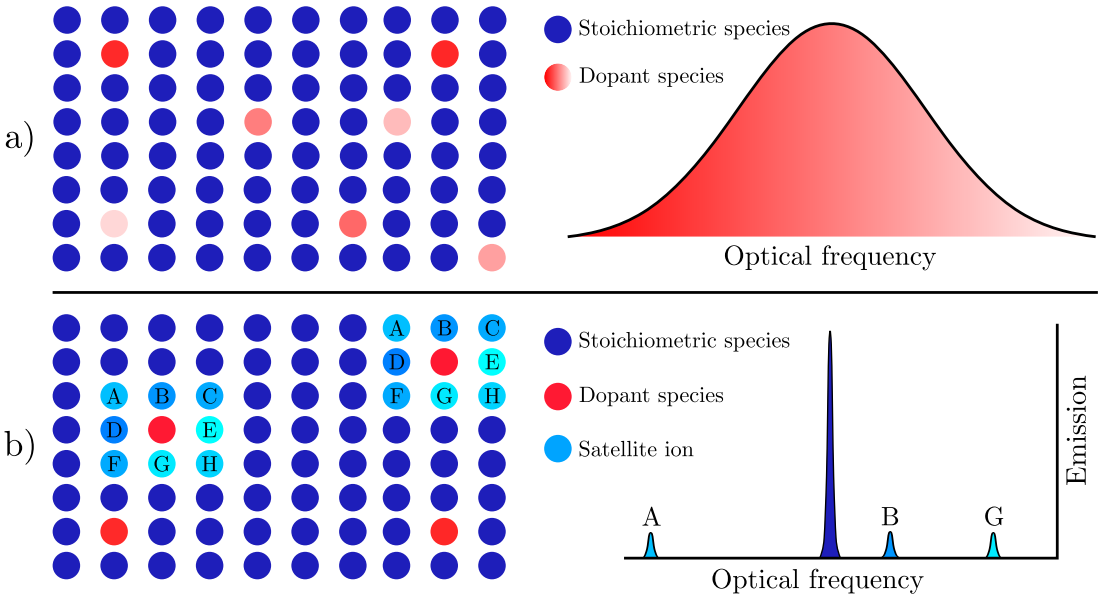

Figure 2.6: The doped (a) and satellite (b) rare-earth systems. In a doped rare-earth system, the rare-earth species of interest (in red) is doped into a crystal composed of a second rare-earth species (blue). In a satellite rare-earth system, a crystal stoichiometric in one rare-earth species (blue) is doped with a second rare-earth species (red), perturbing the transition frequencies of the surrounding stoichiometric ions (light blue), these can then be addressed separately from the stoichiometric bulk.

2.6 $EuCl_3{\cdot}6D_2O$

This thesis concerns the use of trivalent europium as the optically active species in the crystal $EuCl_3{\cdot}6D_2O$. In this system, quantum information is stored on the hyperfine levels of the ground $^7F_0$ state and the optical transition between the $^7F_0$ and $^5D_0$ levels is used to perform gates. Europium has two stable isotopes, $^{151}Eu^{3+}$ and $^{153}Eu^{3+}$, occurring in abundance 47.8% and 52.2% respectively. These isotopes have nuclear spin $J = \frac{5}{2}$ and large quadrupole moments. At zero-field, the $^7F_0$ and $^5D_0$ states are split into three doubly degenerate levels by the total quadrupole Hamiltonian, with level splittings of $\mathcal{O}(40\text{ MHz})$ for $^{151}Eu^{3+}$ and $\mathcal{O}(100\text{ MHz})$ for $^{153}Eu^{3+}$. The energy splittings of the $^7F_0$ and $^5D_0$ levels in $EuCl_3{\cdot}6H_2O$ are displayed in Figure 2.7.

The host system studied in this thesis is the hexahydrate crystal $EuCl_3{\cdot}6H_2O$ with the unit cell of this crystal displayed in Figure 2.8.

$EuCl_3{\cdot}6H_2O$ has the second-lowest known optical inhomogeneous linewidth of any rare-earth solid with only isotopically pure Nd:Y^7LiF_4 and Er:Y^7LiF_4 crystals known to have a lower linewidth [46]. The reported optical inhomogeneous linewidth of the $^7F_0$ and $^5D_0$ transition of $EuCl_3{\cdot}6H_2O$ is 100 MHz in crystals with natural isotopic abundance and 25 MHz when isotopically purified in ^{35}Cl [47]. This low inhomogeneous linewidth allows the hyperfine structure to be resolved and substantially increases the spectral density of these crystals.

In this thesis, I consider the deuterated crystal $EuCl_3{\cdot}6D_2O$, as this crystal has a

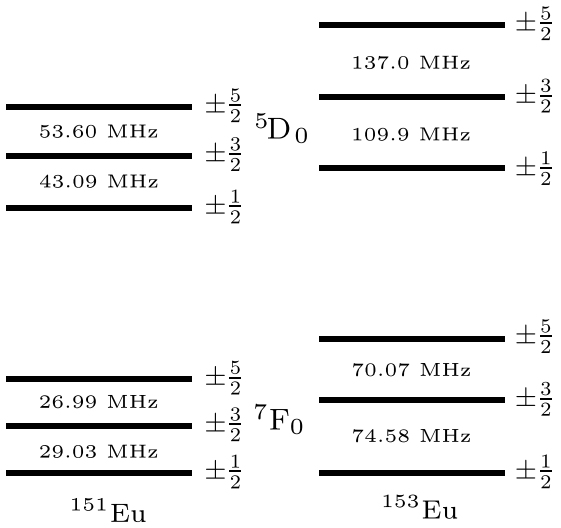

Figure 2.7: Hyperfine structure of the optical ground ($^7F_0$) and excited ($^5D_0$) states of the two Eu^{3+} isotopes in $EuCl_3{\cdot}6H_2O$ at zero-field [43, 44]. The levels are labelled using the m_I labelling despite m_I being a poor quantum number due to strong wavefunction mixing. This labelling is used as "like-to-like" $\Delta m_I = 0$ still have the highest relative oscillator strengths.

much longer optical lifetime of 2.6 ms than $EuCl_3{\cdot}6H_2O$, which has an optical lifetime of 115 μs [48]. The short relative lifetime of $EuCl_3{\cdot}6H_2O$ compared to $EuCl_3{\cdot}6D_2O$ is due to the high energy O-H bond [49–51]. This bond has a stretching mode with frequency $\approx$ 110 THz, which allows non-radiative decay in Eu^{3+} from the $^5D_0$ state to the $^7F_6$ state in a four-phonon process. This short lifetime is improved substantially in deuterated crystals, as the O-D bond has a lower phonon energy of $\approx$ 80 THz [48, 52–54]. The less energetic O-D bond means that non-radiative decay from the Eu^{3+} $^5D_0$ state to the $^7F_6$ state becomes a five-phonon process and we see a corresponding increase in the optical lifetime of $EuCl_3{\cdot}6D_2O$ to 2.6 ms [48].

In addition to the low linewidths, this system has long optical and spin coherence times in deuterated crystals, with measured optical coherence times of $\mathcal{O}(700\mu s)$ [21] and hyperfine coherence times of $\approx$ 40 ms [21]. This hyperfine coherence time has the potential to be substantially extended to $\approx$ 60s using zero first-order Zeeman (ZEFOZ) techniques [44].

The number of spectrally distinct satellite sites is determined by the site symmetry of the dopant site. The Eu^{3+} site in $EuCl_3{\cdot}6H_2O$ has site symmetry C_2 and as rare-earth dopants substitute at the Eu^{3+} site, they also have C_2 site symmetry. The Eu^{3+} ions on the dopant C_2 axis have a unique frequency shift, with each satellite line consisting of ions from a unique site. Eu^{3+} ions not on the dopant C_2 axis have the same frequency shift as another Eu^{3+} ion and due to this, satellite lines at these frequency shifts consist of ions from two sites. Figure 2.9 shows the nearest neighbour satellite lines about a dopant.

The satellite line shift created by a rare-earth dopant scales with the amount of

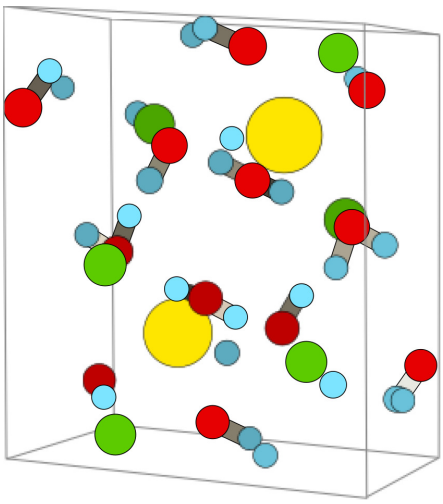

Figure 2.8: Unit cell of $EuCl_3{\cdot}6H_2O$ [45]. Europium atoms are coloured yellow, chlorine green, oxygen red and hydrogen teal.

perturbation to the local crystalline environment, and therefore the dopant radius. The rare-earths with the largest radius mismatch to europium are lanthanum and lutetium, and as such, they give the largest satellite shifts of any rare-earth dopant in $EuCl_3{\cdot}6H_2O$. The specific dopant system considered in this work is La^{3+}:$EuCl_3{\cdot}6D_2O$; this was selected over Lu^{3+} $EuCl_3{\cdot}6D_2O$ as the La^{3+} satellite lines are more spectrally isolated from one another than the Lu^{3+} satellite lines.

To implement quantum gates in an $EuCl_3{\cdot}6H_2O$ system, optical pulses between the $^7F_0$ computing levels and one of the hyperfine states in the $^5D_0$ optical level are used. Performing gates via the optical transition gives less off-resonant excitation of other qubits and the main inhomogeneous line than direct RF gates as qubits are more well resolved in optical frequency. Conditional gates between qubits in this system are performed by using the $\mathcal{O}(10\text{MHz})$ optical shift from optical excitation of nearby ions [55].

2.7 Rare-earth ion ensembles

The rare-earth ion system that this thesis concerns is an *ensemble system*, with a single qubit corresponding to satellite ions from many different spin clusters distributed across the crystal. This ensemble satellite line system is similar to the more commonly seen doped rare-earth systems [33, 56, 57]. Figure 2.10 gives an illustration of a rare-earth ensemble system. This stands in contrast to the *single instance* systems of contemporary interest for scalable quantum computing, in which each qubit is a single quantum object occupying a fixed spatial position in the system.

Ensemble systems have the constituent qubits distributed in space, resulting in the transition frequencies of these qubits being inhomogeneously broadened from inhomogeneities in system parameters across the ensemble such as crystal strain or

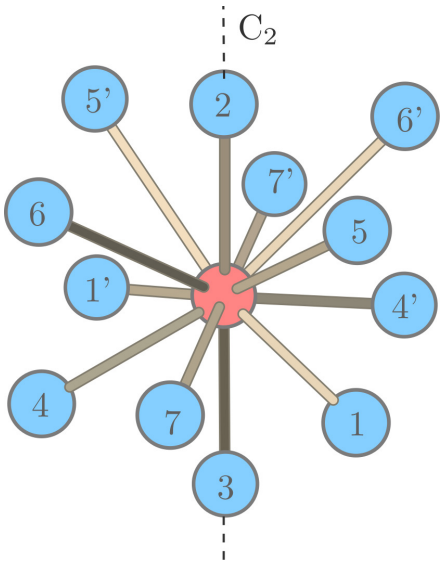

Figure 2.9: The nearest neighbour Eu^{3+} ions around a dopant in $EuCl_3{\cdot}6H_2O$. Ions have been labelled according to the distance from the central dopant ion and identical crystal sites have been labelled with a dash.

applied magnetic field. Due to inhomogeneous broadening, any pulse applied will be off-resonant for many of the ions and as a result, the operation applied to an individual ion will depend on where it is in the inhomogeneous line. To reduce the error when performing operations, a sub-ensemble is used for quantum operations. A subset of the ensemble in a narrow frequency range is prepared such that it can be separately addressed from the rest of the ensemble [56]. Working with a sub-ensemble allows for a smaller frequency distribution to be addressed, reducing the error of quantum operations such that quantum operations can be performed with reasonable fidelity.

2.8 Other spin cluster systems

The $EuCl_3{\cdot}6H_2O$ satellite system is not the only example of a spin cluster system, with several other systems having been proposed and used for quantum information. Notable examples of spin-cluster systems in which quantum computing has been demonstrated are the nitrogen-vacancy (NV) centre system [58–60] and liquid state nuclear magnetic resonance (NMR) [61–64]. In this section, I will explain the key differences between the attributes of the $EuCl_3{\cdot}6D_2O$ satellite system and the NV and NMR systems.

2.8.1 Nitrogen-vacancy centres

The most prominent spin-cluster system in the quantum information field at the time of writing is the NV centre system. An NV centre is a point-defect in diamond

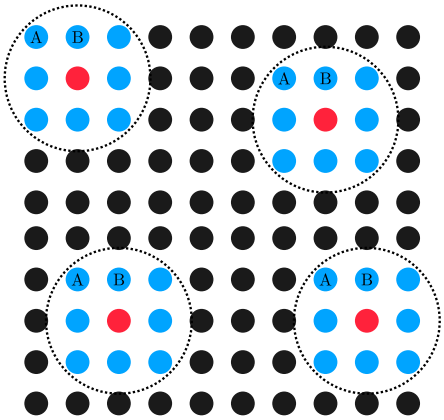

Figure 2.10: The rare-earth satellite system considered in this thesis is an ensemble, with many copies of the satellite cluster around a dopant distributed across the crystal. Each satellite line (e.g. the A and B lines) is composed of many ions distributed across the crystal.

consisting of a nitrogen atom that replaces a carbon in the crystal and an adjacent lattice vacancy. The nitrogen-vacancy centre and any nearby ^{13}C atoms are spectrally resolved from the ^{12}C bulk and can be used as qubits for a quantum system [58–60], Figure 2.11 gives an illustration of an NV spin-cluster.

The qubits in an NV system are the $I = \frac{1}{2}$ nuclear spins of the ^{13}C and either the electron ($S = \frac{1}{2}$) or nuclear ($I = 1$) spin of the NV centre. To initialise an NV system, the electron spin of the NV centre is used. The NV electron spin is first prepared in the $m_s = 0$ state using optical pumping, and this electron spin state is then swapped with a nuclear spin state. This process of initialising the NV electron spin to $m_s = 0$ and swapping it with another spin state is then repeated until all of the relevant spins have been initialised.

Quantum operations are implemented using RF pulses on the nuclear and electron spin states to manipulate the qubit states. Conditional logic is implemented using the interaction between the NV electron spin and the qubit nuclear spins. The nuclear spins experience a phase shift conditional on the electron spin state, allowing gates conditional on the NV state. Conditional logic between ^{13}C atoms is implemented using the NV centre as an intermediate qubit. This is in contrast to the rare-earth satellite system in which conditional logic can be implemented directly between satellite qubits.

Readout in this system is accomplished using an optical readout of the electron spin of the NV centre. The electron spin state is correlated with one of the nuclear spin states using a CNOT gate; a projective single-shot measurement can then be made to measure the nuclear spin state.

The coherence times of the nuclear spin qubits is $\mathcal{O}(10\text{ms})$ at cryogenic temperatures [65] and the electron spin coherence time is $\mathcal{O}(1\text{ms})$. The NV coherence times are sufficiently long to allow readout fidelities of ≥ 0.9 of the nuclear spin states and gate fidelities of ≥ 0.99 [66]. The nuclear spin coherence times of rare-earth satellite systems

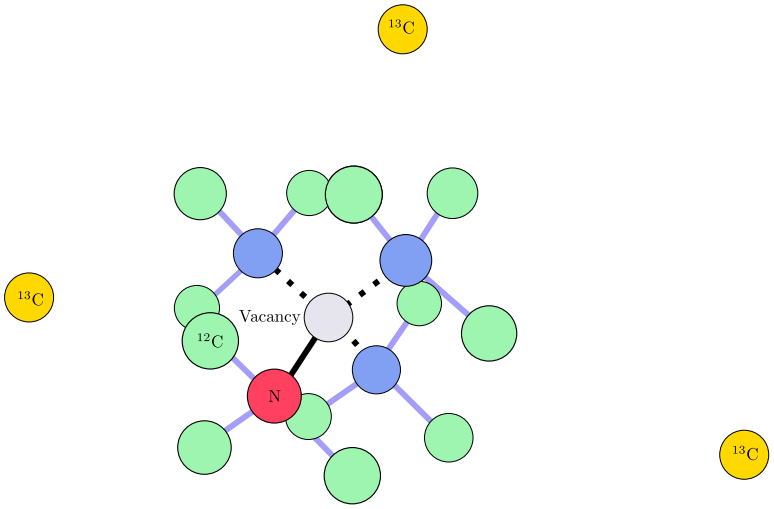

Figure 2.11: A nitrogen-vacancy centre with three nearby ^{13}C atoms. The ^{12}C atoms between the ^{13}C and the NV centre have been omitted to simplify the diagram.

have the potential to be $\mathcal{O}(\text{minutes})$ [44] which is substantially longer than the NV spin coherence times. However, gates are implemented via an optical transition with a coherence time of $\mathcal{O}(700\mu\text{s})$ [21] as opposed to the direct RF gates used in the NV system. The shorter coherence time of the NV system relative to the $EuCl_3{\cdot}6H_2O$ system is counterbalanced by its $\mathcal{O}(\text{GHz})$ [58] energy level splittings, compared to the energy level splittings of $\mathcal{O}(40\text{ MHz})$ in $EuCl_3{\cdot}6H_2O$. The comparable ratio of coherence time to energy level splittings between NV and $EuCl_3{\cdot}6H_2O$ means that the gate errors are likely to be of a similar order in these systems. However, for quantum memory purposes, the long spin coherence times makes the rare-earth satellite system more suitable.

The ^{13}C atoms in a diamond are randomly distributed and a nitrogen-vacancy site must be found with sufficient nearby ^{13}C atoms to achieve the desired number of qubits. This random distribution of ^{13}C atoms limits the size of NV cluster systems to at most a handful of qubits, with every NV cluster system having different attributes due to the relative positioning of the atoms. In the rare-earth satellite system, the number of satellites that can be addressed is limited by the strength of the perturbation from the dopant ion rather than the distribution of ions in the crystal. Due to this, tens of qubits can be resolved in these systems.

2.8.2 Nuclear magnetic resonance

The classic example of an ensemble spin-cluster system is liquid state NMR [61–63]. Liquid state NMR uses solutions of molecules, with several spin-half nuclei per molecule. A static magnetic field is applied to lift the spin degeneracy, allowing the spin states to be used as computing levels. In a given molecule, different nuclei will have different resonant frequencies and interactions with surrounding nuclei; hence they can be used as distinct qubits. Figure 2.12 displays example molecules for NMR

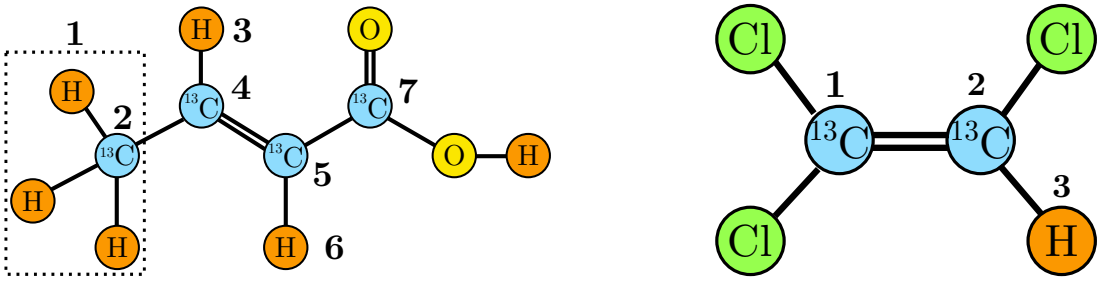

Figure 2.12: Examples of molecules used for liquid NMR computing, with qubits numbered. The molecule to the left is fully labelled crotonic acid, which is a seven qubit system with qubits given by the spin $\frac{1}{2}$ component of the methyl group, the spin of the Hydrogen adjacent the double bond and the spin of the four Carbon-13 nuclei . The molecule to the right is fully labelled crotonic acid, which is a three qubit system with qubits given by the spins of the two Carbon-13 nuclei and the spin of the Hydrogen.

computing.

The Zeeman splitting between qubit states is small compared to the thermal energy for any practical temperature and due to this, it is not possible to initialise an NMR system into a pure quantum state. NMR computing instead operate operates on pseudo-pure states of form $\rho = \frac{1-\epsilon}{2^n}\mathbb{1} + \epsilon \left|\psi\right\rangle \left\langle\psi\right|$, where $\mathbb{1}$ is an identity matrix, $\left|\psi\right\rangle \left\langle\psi\right|$ is some pure state, n is the dimensionality of the vector space and ϵ is a small positive number [61]. The use of pseudo-pure states means that there is an exponential decrease in ensemble size as the qubit number is increased, with $\epsilon \approx \frac{nh\nu/KT}{2^n}$ [67]. In order for any liquid state NMR system to scale to a useful number of spins, it would be necessary to have some mechanism for initialising the system, such as optical pumping. An additional problem that arises from the use of pseudo-pure states is the lack of ability to re-initialise spins during a computing sequence, meaning that NMR computing states can only use quantum error correction techniques a single time per computation. The rare-earth satellite system has optical levels that the system population can be driven to, allowing for ions to be optically pumped into specific ground-state hyperfine levels. The ability to optically pump means that qubit resets can be performed in this system and error correction techniques can be performed multiple times.

Gates are implemented in the NMR system using RF pulses to drive qubits between the Zeeman states. Conditional operations are implemented using the spin-spin J coupling between nuclei in the molecule to induce phase shifts. The qubits in NMR systems have only two levels, with no additional auxiliary levels. Due to this, the J coupling is always present between nuclei. In order to decouple nuclei to perform gates on only single qubits, special decoupling sequences must be used. In contrast, gates are performed via the optical transition in the rare-earth satellite system, allowing isolated gates to be performed on a qubit without interaction from other qubits.

Readout of states in NMR computing schemes is accomplished using standard NMR spectral techniques such as spin echoes. There are analogous photon-echo schemes that can be used for the readout of rare-earth satellite systems.

NMR systems can have long coherence times for single-qubit states, on the order of several seconds. However, multi-qubit states can be more strongly affected by decoherence in such systems, giving them relatively short coherence times ($\mathcal{O}(100\text{ ms})$) [68] compared to the gate time ($\mathcal{O}(100\text{ ms})$) [67]. Single-qubit nuclear spin coherence times in rare-earth satellite systems have the potential to be $\mathcal{O}(\text{hours})$ and due to the minimal perturbation from surrounding qubits [32] it is expected that multi-qubit states will have comparable coherence times. Gates in rare-earth satellite systems can be implemented on $\mathcal{O}(\mu\text{s})$ timescales which is much shorter than both the spin and optical coherence times in these systems.

2.8.3 Summary

This chapter introduced the properties of the rare-earth materials relevant to this thesis and the concept of ensemble quantum computing. The chapter began by discussing the chemistry of the rare-earths along with the origin of their coherence times and level structure. The $4f$ electron states in the rare-earth are shielded from external environmental noise by the $5s$ and $5p$ shells giving these transitions long lifetimes and coherence times. The radius of the rare-earth atoms increases with atomic number; this forms the basis for stoichiometric satellite rare-earth computing, in which a rare-earth crystal is lightly doped with a second rare-earth species.

The concept of an ensemble quantum computer was then introduced, in which each logical qubit consists of many physical qubits. The europium $^7\text{F}_0 \rightarrow ^5\text{D}_0$ optical transition used in this thesis were discussed along with the lifetimes and inhomogeneous linewidths of the crystal host $EuCl_3{\cdot}6D_2O$.

The chapter concluded with a comparison between rare-earth satellite systems and the nitrogen-vacancy and liquid-state NMR systems. NV systems use a NV centre along with any nearby ^{13}C atoms as a computing system, with nuclear coherence times of $\mathcal{O}(10\text{ms})$ and $\mathcal{O}(1\text{ms})$. The random distribution of ^{13}C limits the size of NV computing systems to a handful of qubits, as an NV site must be found with sufficient nearby ^{13}C atoms. Liquid state NMR uses solutions of molecules as a quantum system, and an applied magnetic field is used to separate the energies of the spin states of the individual nuclei, allowing their use as computing levels. The lack of an excited optical state means that it is not possible to initialise NMR systems and instead, a pseudo-pure state must be used, severely limiting the ability of this system to scale. The single-qubit coherence times of NMR systems can be $\mathcal{O}(\text{s})$. However, the coherence times of multi-qubit states are much shorter at $\mathcal{O}(100\text{ms})$. Gate errors in NMR systems are high due to this decreased coherence time and the slow speed of NMR gates.

Chapter 3

Quantum Computing

This chapter introduces the concepts relevant for implementing quantum computing. The requirements for the construction of a large scale quantum computer are first detailed, with discussion as to the limiting factors in current quantum systems. This is followed by an outline of the function of quantum gates, with the behaviour of notable examples listed. The chapter concludes with a discussion of quantum error correction and its implementation in single-instance and ensemble systems.

The execution of large quantum algorithms requires that the computing system is both large enough to encode the problem and of a high enough quality that the algorithm output is useful. The specific set of requirements for a large scale quantum computer were summarised in 2004 by David DiVincenzo [69]:

1. A scalable physical system with well-characterised qubits.
2. The ability to initialise the state of the qubits to a simple fiducial state, such as $|000...\rangle$.
3. Long relevant decoherence times, much longer than the gate operation time.
4. A "Universal" set of quantum gates.
5. A qubit-specific measurement capability.

There are an additional two criteria that were later proposed to address the integration of a quantum computer into a quantum communication system:

6. The ability to interconvert stationary and flying qubits.
7. The ability to faithfully transmit flying qubits between specified locations.

For a computing system to be able to satisfy these criteria, it is necessary that it is fault-tolerant, with the ability to correct for errors in the qubits and gates. A system that is not fault-tolerant will fail to satisfy criteria 1 and 3 when scaled to a large enough number of qubits or with a long enough algorithm due to the increasing probability of an error on one of the qubits.

It was initially believed that practical implementation of any physical quantum computer would be infeasible due to the fragility of the quantum state, with errors compounding so quickly that the quantum state would be completely corrupted [70]. In a classical computer, this issue can be solved by one of a variety of error correction algorithms, all of which function by some variety of data duplication. On a quantum computer, the no-cloning theorem [71] means that such an approach cannot be used.

In 1995 and 1996, there were several papers published proposing codes allowing for error correction in quantum systems [11, 72–75]. With the discovery of such codes, it became possible to create fault-tolerant quantum computers and interest in the field has grown substantially since then.

Current quantum computing platforms have been able to separately satisfy the DiVincenzo criteria, with demonstrations of scalability [15, 22], initialisation [76], sufficient gate error rates [77–79], universal gate sets [23] and qubit specific measurement [77]. The use of error correction in current quantum systems is discussed later in this chapter.

Creating systems that satisfy all of these criteria concurrently has proven difficult. As the number of qubits is increased, applying a gate to one qubit has increasingly complicated effects on other qubits [80–82], quickly becoming complex enough that the qubits can not be said to be "well-characterised". In addition, with increasing numbers of qubits and a corresponding increase in the complexity of qubit interactions, current error correction schemes become ineffective as they leave many potential *noise channels* uncorrected (a noise channel is some system operator ϵ with action $\epsilon(\rho) = \sum_k U_k^\dagger \rho U_k$).

To realise large-scale quantum computing, it will be necessary to carefully calibrate the computing system to minimise errors and implement effective quantum error-correction algorithms. The system calibration and error-correction schemes necessary for large-scale quantum computing will require the ability to characterise system noise for quantum systems and evaluate error correction protocols under different noise regimes.

In Chapter 4 we evaluate the performance of the rare-earth satellite system this thesis is concerned with under the DiVincenzo criteria. The rest of this chapter is concerned with the fundamental operations of a general quantum computer.

3.1 Quantum gates

To perform error correction in a quantum system, it is necessary to apply quantum gates during each round of correction. For a quantum error correction procedure to be useful, the error involved in the correction process needs to be low with a minimal number of gates used. This section explains the concept of a quantum gate and gives examples of common gates that are used for implementing both quantum algorithms and quantum error correction.

The fundamental building blocks of quantum computing are quantum logic gates, as with digital computing and classical logic gates. A quantum logic gate is a basic quantum circuit that has some reversible action on a small number of qubits, for

example, the quantum X gate, which maps $|0\rangle$ states to $|1\rangle$ and vice versa.

Mathematically, quantum logic gates can be represented using unitary matrices. A quantum logic gate acting on n qubits is written as a $2^n \times 2^n$ unitary matrix, which operates on the 2^n complex vectors used to represent quantum states.

The action of any unitary operator on a quantum state can be implemented in a quantum computer via some sequence of quantum logic gates. In practice, there are standard gates that are commonly used for quantum computing due to their simplification of quantum algorithms and ease of implementation in some systems. In the following, I give examples of these common gates:

Identity:

The identity gate is the "Do Nothing" operation, mapping a state to itself. The matrix form is:

$$I = \begin{bmatrix} 1 & 0 \\ 0 & 1 \end{bmatrix} \tag{3.1}$$

Pauli-X gate:

The X gate is a single-qubit gate analogous to the NOT gate in classical computing. It is equivalent to a rotation about the X axis of the Bloch sphere by π. It maps $|0\rangle$ to $|1\rangle$ and $|1\rangle$ to $|0\rangle$. The matrix form is:

$$X = \begin{bmatrix} 0 & 1 \\ 1 & 0 \end{bmatrix} \tag{3.2}$$

Pauli-Y gate:

The Y gate is a single-qubit gate equivalent to a rotation about the Y axis of the Bloch sphere by π. It maps $|0\rangle$ to $i|1\rangle$ and $|1\rangle$ to $-i|0\rangle$. The matrix form is:

$$Y = \begin{bmatrix} 0 & -i \\ i & 0 \end{bmatrix} \tag{3.3}$$

Pauli-Z gate:

The Z gate is a single-qubit gate equivalent to a rotation about the Z axis of the Bloch sphere by π. It maps $|0\rangle$ to $|0\rangle$ and $|1\rangle$ to $-|1\rangle$. The matrix form is:

$$Z = \begin{bmatrix} 1 & 0 \\ 0 & -1 \end{bmatrix} \tag{3.4}$$

Phase shift (R_ϕ) gates:

The R_ϕ gates are a family of single-qubit gates which introduce a ϕ phase shift between the $|0\rangle$ and $|1\rangle$ states. They map $|0\rangle$ to $|0\rangle$ and $|1\rangle$ to $e^{i\phi}$. Specific examples of phase shift gates are the T gate with $\phi = \frac{\pi}{4}$, S gate with $\phi = \frac{\pi}{2}$ and Z gate with $\phi = \pi$. The matrix form is:

$$S = \begin{bmatrix} 1 & 0 \\ 0 & e^{i\phi} \end{bmatrix} \tag{3.5}$$

Hadamard (H) gate:

The Hadamard gate is a single-qubit gate often used to create superposition states. It is equivalent to a rotation of π about axis $\frac{x+z}{\sqrt{2}}$ on the Bloch sphere. It maps $|0\rangle$ to $\frac{|0\rangle+|1\rangle}{\sqrt{2}}$ and $|1\rangle$ to $\frac{|0\rangle-|1\rangle}{\sqrt{2}}$. The matrix form is:

$$H = \frac{1}{\sqrt{2}} \begin{bmatrix} 1 & 1 \\ 1 & -1 \end{bmatrix} \tag{3.6}$$

Controlled NOT (CNOT) gate:

The controlled NOT gate is a two-qubit gate, often used as one of the basic conditional logic gates in quantum computing. It performs a NOT gate on the second qubit if the first qubit is in state $|1\rangle$ and otherwise leaves it unchanged. For a two-qubit basis $\{|00\rangle, |01\rangle, |10\rangle, |11\rangle\}$ the matrix form is:

$$CNOT = cX = \begin{bmatrix} 1 & 0 & 0 & 0 \\ 0 & 1 & 0 & 0 \\ 0 & 0 & 0 & 1 \\ 0 & 0 & 1 & 0 \end{bmatrix} \tag{3.7}$$

Toffoli (CCNOT) gate :

The Toffoli or controlled-controlled NOT gate is a three-qubit gate often used as a way to implement non-reversible classical gates. It performs a NOT gate on the third qubit only if the first two qubits are in state $|1\rangle$ and otherwise leaves it unchanged. For three-qubit basis $\{|000\rangle, |001\rangle, |010\rangle, |011\rangle, |100\rangle, |101\rangle, |110\rangle, |111\rangle\}$ the matrix form of a CCNOT is:

$$T = CCNOT = \begin{bmatrix} 1 & 0 & 0 & 0 & 0 & 0 & 0 & 0 \\ 0 & 1 & 0 & 0 & 0 & 0 & 0 & 0 \\ 0 & 0 & 1 & 0 & 0 & 0 & 0 & 0 \\ 0 & 0 & 0 & 1 & 0 & 0 & 0 & 0 \\ 0 & 0 & 0 & 0 & 1 & 0 & 0 & 0 \\ 0 & 0 & 0 & 0 & 0 & 1 & 0 & 0 \\ 0 & 0 & 0 & 0 & 0 & 0 & 0 & 1 \\ 0 & 0 & 0 & 0 & 0 & 0 & 1 & 0 \end{bmatrix} \tag{3.8}$$

A universal set of quantum gates is a set of quantum gates such that any unitary operation can be decomposed into just this set of gates. A common choice of universal gate set is the Clifford $+T$ gate set given by $\{X, Y, Z, CNOT, H, S, T\}$.

3.2 Errors in quantum systems

In a classical computing system, there is only one type of error that can occur: the bit-flip error, which maps $0 \rightarrow 1$ and vice versa. In a quantum computing system, there are an infinite number of possible qubit states and correspondingly an infinite number of possible qubit errors.

Errors on a quantum system can be classed into two categories: coherent errors, which preserve quantum information and incoherent errors resulting in a loss of

information from the system.

First, consider the case of a coherent error on a single qubit, in which the error is a unitary operator $U(\delta\theta, \delta\phi)$ with action on a single qubit given by:

$$U(\delta\theta, \delta\phi)\,|\psi\rangle = \cos\left(\frac{\theta+\delta\theta}{2}\right)|0\rangle + \sin\left(\frac{\theta+\delta\theta}{2}\right)e^{i(\phi+\delta\phi)}\,|1\rangle\,. \tag{3.9}$$

Coherent errors are a continuum of rotations on the Bloch sphere characterised by the rotation angles $\delta\theta$ and $\delta\phi$. In order to correct for coherent errors we decompose the errors into the Pauli basis $\{I, X_0, Z_0, X_0Z_0\}$:

$$U(\delta\theta, \delta\phi)\,|\psi\rangle = \alpha_I I\,|\psi\rangle + \alpha_2 X_0\,|\psi\rangle + \alpha_3 Z_0\,|\psi\rangle + \alpha_4 X_0 Z_0\,|\psi\rangle\,. \tag{3.10}$$

In a multi-qubit system, it is possible to encode the qubit such that measurements can be performed such that the system is collapsed into one of the four states: the original state $|\psi\rangle$, a *bit-flip* error $X_0\,|\psi\rangle$, a *phase-flip* error $Z_0\,|\psi\rangle$ or a combined bit-flip and phase-flip error $X_0Z_0\,|\psi\rangle$. Such measurements are called *syndrome* measurements and are explored later in this chapter. The values of syndrome measurements can then be used to determine if an error has occurred and to apply the appropriate correction operation.

The action of bit-flip, phase-flip and combined bit-flip, phase-flip errors on a quantum state are as follows:

- Bit-flip: In a bit-flip error the $|0\rangle$ and $|1\rangle$ states are swapped, inverting the quantum state, i.e. the state $|\Psi\rangle = A\,|0\rangle + B\,|1\rangle \rightarrow A\,|1\rangle + B\,|0\rangle$. Bit-flip errors are direct analogues of classical bit-flip errors.

- Phase-flip: In a phase-flip error a relative phase of π is introduced between the $|0\rangle$ and $|1\rangle$ states, i.e. $A\,|0\rangle + B\,|1\rangle \rightarrow A\,|0\rangle - B\,|1\rangle$. Phase flips are a type of error with no analogue on a classical computer.

- Combined bit-flip and phase-flip: In a combined bit-flip and phase-flip error there is both a swapping of the $|0\rangle$ and $|1\rangle$ states and an introduction of a π phase shift, i.e. $A\,|00\rangle + B\,|11\rangle \rightarrow A\,|10\rangle - B\,|01\rangle$.

A quantum error correction scheme that can correct for bit-flip, phase-flip and combined bit-flip and phase-flip errors can therefore correct for any coherent error on a single qubit. Similarly, it can be shown that unitary errors on more than a single qubit can be decomposed into either bit-flip, phase-flip or combined bit-flip and phase-flip errors on single qubits, hence to correct for an arbitrary unitary error, it is sufficient to correct for these three types of error.

Incoherent errors result in a loss of coherence from the system, taking a pure state $\rho = |\psi\rangle\langle\psi|$ to a probabilistic mixture of pure states (a mixed state) $\rho = \sum_i P_i\,|\psi\rangle_i\langle\psi|_i$. As a mixed state is simply a sum of pure states, any error correction protocol that corrects for arbitrary unitary errors on pure states will also correct for incoherent errors.

In addition to single-qubit error channels, it is possible for quantum systems to have correlated errors, with the probability of errors on other qubits in the quantum system increasing or decreasing with errors on one of the qubits. Correlated errors can arise from a noise source affecting multiple qubits, gate operations with unintended effects on qubits or some combination of these effects. In basic error correction schemes, it is assumed that qubit errors are uncorrelated, allowing error correction using some variant of a majority vote scheme when the two-qubit error probability is sufficiently low. In the case of only correlated errors, such a scheme will always fail, as there will always be more than one qubit error. Physical systems will lie somewhere on the spectrum between these uncorrelated and fully correlated regimes. Characterisation of the correlation between qubit errors in a quantum system will allow for system-specific error correction protocols to be created that minimise the effect of both correlated and uncorrelated errors.

3.3 Error correction in single instance

In a classical computer, a state can be corrected by creating redundant copies of the data, for example, by storing the state A as $A \otimes A \otimes A$. Errors in the computation can then be corrected by comparing the values of the different copies of the data.

In a quantum computer, the no-cloning theorem prohibits simply storing redundant copies of the data. Additionally, errors in a quantum computer are continuous rather than discrete and the state of the system can not simply be measured to determine if an error has occurred.

To correct for errors in a quantum system, the superposition state is distributed across additional qubits, creating a *logical qubit* constructed out of several physical qubits. Additional qubits are initialised to the $|0\rangle$ state for use as *syndrome qubits* in the correction process. As stated in the previous section, continuous errors can be decomposed into a finite number of error operators on the quantum state. Detection of errors is accomplished by performing controlled gates onto the syndrome qubits such that they store information about whether an error has occurred. Measurement of the syndrome qubits partially collapses the system into a definitive error state and controlled gates are applied to correct for errors based on the syndrome measurements.

States are prepared for quantum error correction by encoding in a basis such that a syndrome measurement can be performed to indicate whether an error has occurred. For example, consider the initial state $A|0\rangle + B|1\rangle$ which we wish to protect against bit-flip errors. In an analogue classical computer case we could use the repetition code $(A|0\rangle + B|1\rangle)(A|0\rangle + B|1\rangle)(A|0\rangle + B|1\rangle)$. In a quantum computer, we can encode the qubit using the logical qubit $A|000\rangle + B|111\rangle$. Under the assumption that only one or zero bit-flips have occurred, there are then four possible bit-flip states: no error or an error on any of the three qubits. To correct for these errors, we then perform conditional operations on additional qubits known as ancilla qubits, based on the values of the logical qubits. The values stored on the ancilla qubits are known as error syndromes. Conditional gates are then applied based on the value of the ancilla

qubits to correct the error.

Implementing quantum error correction requires additional system resources, with a need for additional qubits for encoding and syndrome measurement and gates for encoding, syndrome measurement and correction. Encoding a quantum state into a logical qubit across several physical qubits exposes the state to potential multi-qubit noise channels. No quantum gate is perfect and there will always be a difference between the desired unitary operation and the physical gate applied to the system, creating additional errors. The potential errors due to the use of additional qubits and gates mean that implementing quantum error correction will not necessarily reduce system error. The errors caused by the error correction resource overhead must be significantly less than the expected system error for the implementation of error correction to be worthwhile.

Error correction protocols have been successfully demonstrated in quantum computing systems, with the first demonstration in a single-instance system in 2004 [83]. Several demonstrations of a reduction in state error when errors are artificially induced have since been published [26, 27, 66, 83–86], with additional papers demonstrating the operations for error correction but not showing a coherence time extension [28, 87].

3.3.1 Bit-flip code

As an instructive example of implementing a quantum error correction code, we will consider the example of the bit-flip code [88]. The standard bit-flip code is a three-qubit code used to correct for single bit-flip errors on a qubit.

Encoding:

The initial quantum state is of form $|\psi\rangle = A|0\rangle + B|1\rangle$. To encode the state in a three-qubit space, two additional qubits are first initialised to zero, giving $|\psi\rangle = A|000\rangle + B|100\rangle$. A controlled-NOT (CNOT) gate is then performed on qubit two with qubit one as the control giving the state $|\psi\rangle = A|000\rangle + B|110\rangle$. The initialisation finishes by performing a CNOT on qubit three with qubit one as the control giving the state $|\psi\rangle = A|000\rangle + B|111\rangle$.

Correction:

After a period of time, an error may have occurred. Under the assumption of one or fewer errors the system is in the following set of states:
$\{A|000\rangle + B|111\rangle, A|100\rangle + B|011\rangle, A|010\rangle + B|101\rangle, A|001\rangle + B|110\rangle\}$.

Whether an error has occurred and if so on which qubit is determined by measuring the syndromes Z_0Z_1 and Z_1Z_2 (Where the syndrome notation is such that $Z_0Z_1 = Z \otimes Z \otimes I$ and $Z_1Z_2 = I \otimes Z \otimes Z$).

The syndrome is measured by performing a CNOT gate on the first ancilla with qubit one as the control, followed by a second CNOT on this qubit with qubit two as the control. CNOT gates are then performed on a second ancilla with qubit two as a control and qubit three as a control.

The state of these ancilla qubits is then measured. If the first ancilla measurement is true and the second is false, a NOT gate is applied to the first qubit. If both are true, a NOT is applied to the second qubit and if the first is false and the second true, a NOT is applied to the third qubit.

In circuit diagram notation, this sequence takes the following form:

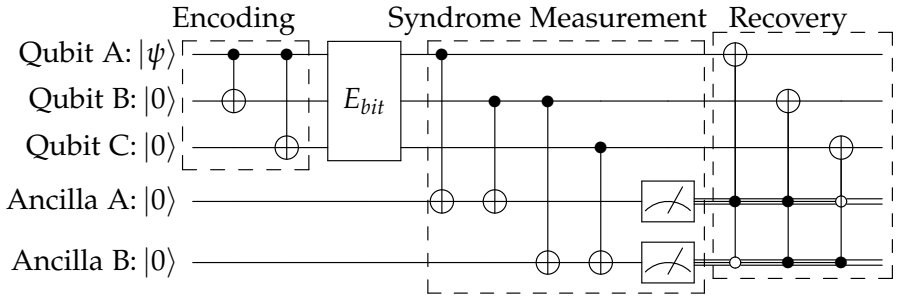

3.3.2 Phase-flip code

The phase-flip code [88] is implemented in a similar fashion to the bit-flip code, with the difference that before and after the expected error, Hadamard gates are applied.

The encoded state takes the form:
$|\psi\rangle = A(|0\rangle + |1\rangle)(|0\rangle + |1\rangle)(|0\rangle + |1\rangle) + B(|0\rangle - |1\rangle)(|0\rangle - |1\rangle)(|0\rangle - |1\rangle)$.

After some possible error has occurred to the encoded state, the syndromes X_0X_1 and X_1X_2 are measured and correcting gates applied. In circuit diagram notation, this sequence takes the following form:

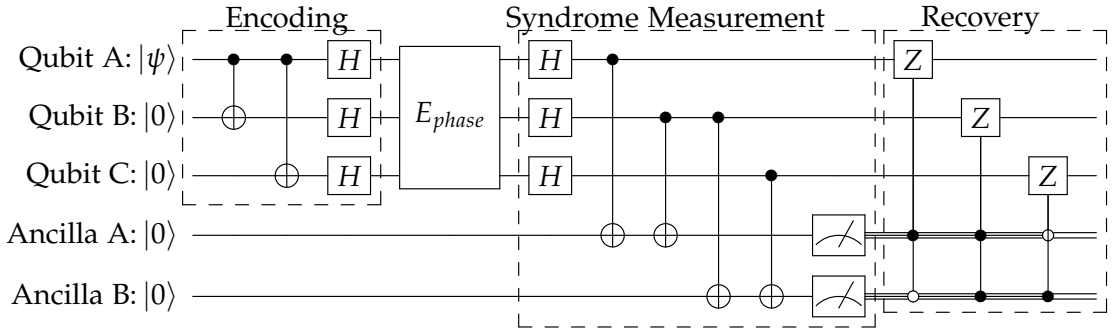

3.3.3 Shor code

The simplest error correction code that can correct for both bit-flip and phase-flip errors is the Shor code [11], which is a nine qubit code constructed by concatenating the bit-flip and phase-flip codes. The encoding sequence for this concatenated code is displayed in the following circuit diagram:

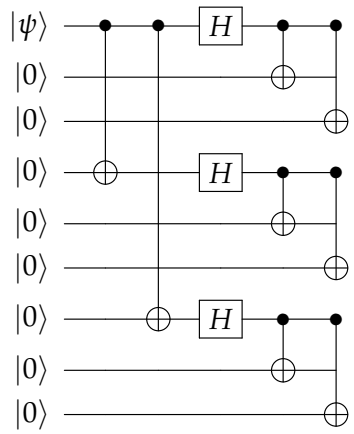

Correction of bit-flip errors:

Correcting for errors in this encoding is performed in two blocks. First, bit-flip errors are corrected by measuring the syndromes $\{Z_0Z_1, Z_1Z_2, Z_3Z_4, Z_4Z_5, Z_6Z_7, Z_7Z_8\}$ and applying correcting gates. This bit-flip correction sequence is shown in the following:

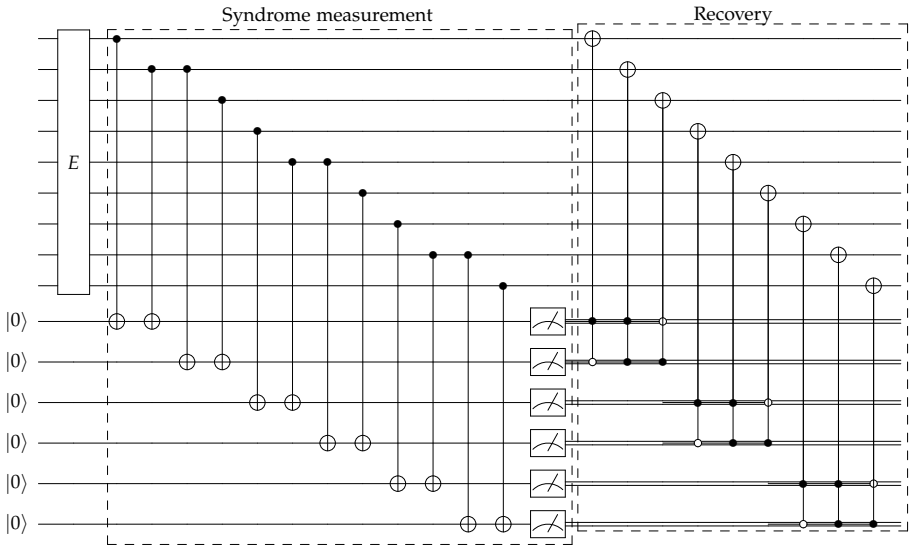

Correction of phase-flip errors:

Following the bit-flip correction procedure, any phase-flips in the system are corrected. The syndromes for this correction are $\{X_0X_1X_2X_3X_4X_5, X_3X_4X_5X_6X_7X_8\}$. The measurement and correction procedure for phase-flip errors are shown in the following circuit diagram:

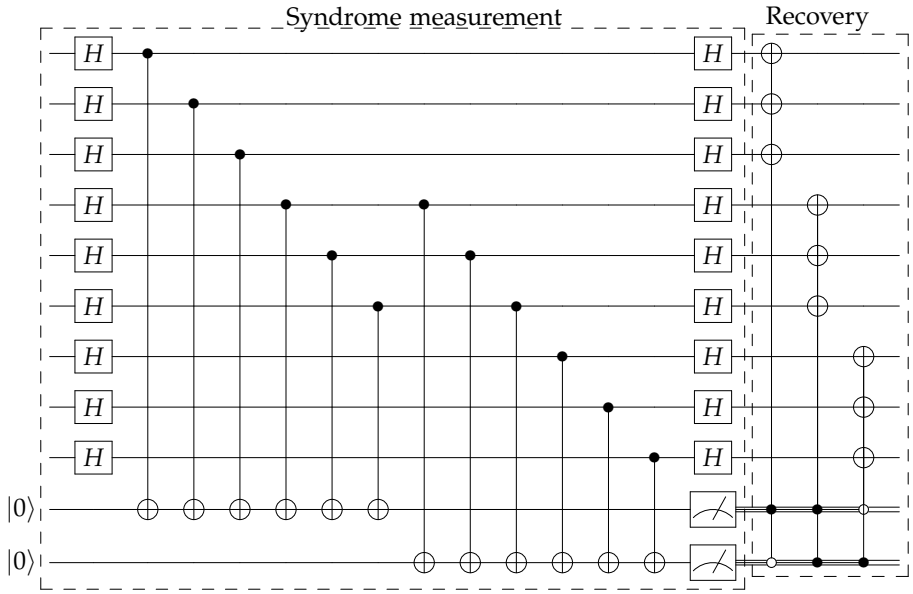

3.3.4 Steane code

A slightly more complicated code allows for correction of both bit and phase-flip errors with only seven qubits and six ancilla qubits. This is the seven qubit Steane code [72], with the encoding sequence shown below:

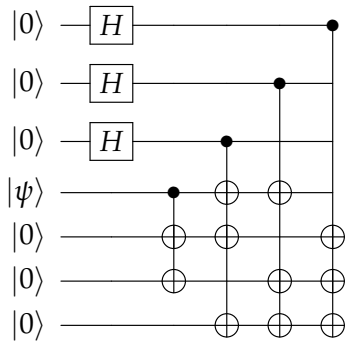

Syndrome measurement:

There are 21 possible single-qubit errors that may occur to this code: a bit-flip error on one of the qubits, a phase-flip error on one of the qubits or both bit and phase-flip errors on a qubit. To correct for errors we first measure the six syndromes: $N_0 = Z_0Z_4Z_5Z_6, N_1 = Z_1Z_3Z_5Z_6, N_2 = Z_2Z_3Z_4Z_6, M_0 = Z_0Z_4Z_5Z_6, M_1 = Z_1Z_3Z_5Z_6, M_2 = Z_2Z_3Z_4Z_6$. The measurement sequence for these syndromes is shown in the following circuit diagram:

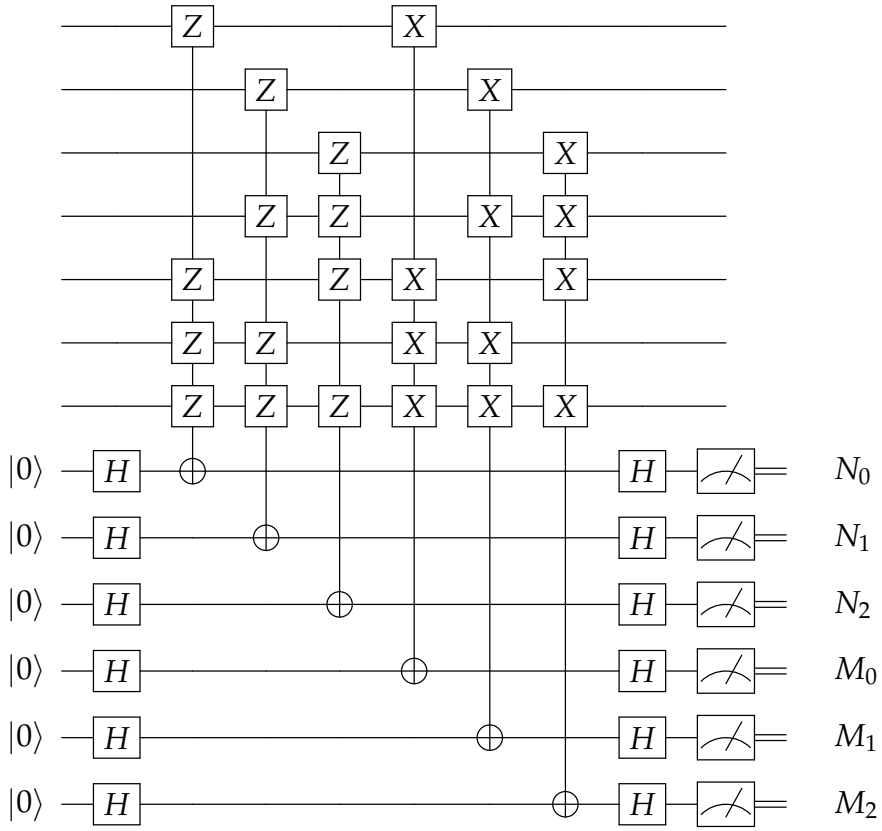

Error correction:

As with the other error correction codes, these syndromes are then used to apply controlled gates. The N syndromes give information on bit-flip errors and the M syndromes on phase-flip errors. The following circuit diagram is one possible correction sequence for the errors that can occur to the seven qubit Steane code:

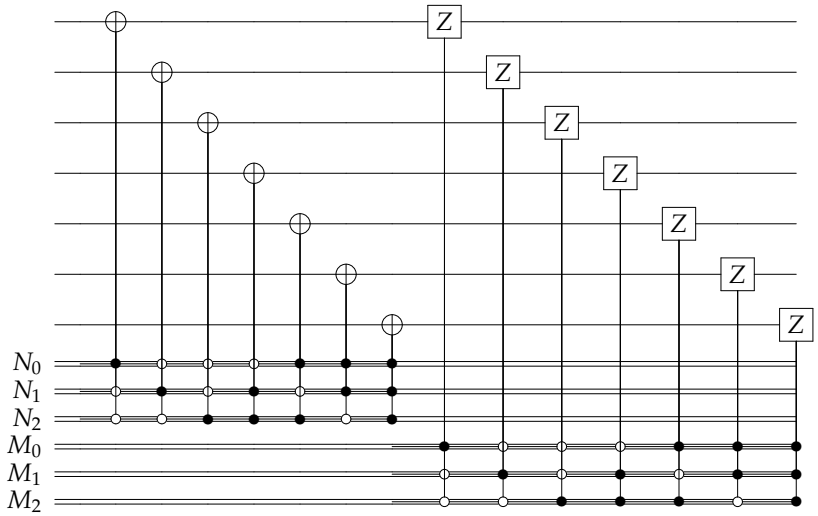

This correction sequence first corrects bit-flip errors using the N syndromes,

followed by correction of the phase-flip errors using the M syndromes. Combined bit-flip and phase-flip errors are operated on by both rounds of correction.

This explanation of the Steane and Shor codes is merely an illustration of the operation of quantum codes, with more complicated codes being useful in many contexts. In particular, it is possible to modify the Steane code and several other quantum codes such that only two ancilla qubits are required [89, 90]

3.3.5 Status of error correction in single instance

To date, quantum error correction demonstrations have been limited in scope, with the current state of the art superconducting microwave qubit systems not using error correction protocols due to the marginal reduction in error compared to the resource overhead. There has been only one demonstration to date in which quantum error correction was shown to increase qubit coherence time under the influence of un-induced noise in the system [91].

The single-instance systems that quantum error correction have been demonstrated in have a low degree of qubit connectivity, with superconducting microwave and trapped ion systems primarily utilising nearest-neighbour interactions and NV systems implementing controlled operations using the NV centre as an intermediary between qubits. The superconducting microwave and trapped ion systems exhibit a large amount of crosstalk between qubits, limiting current trapped ion systems to 14 qubits [92], with the microwave systems encountering similar problems in the current $\mathcal{O}$(50 qubits) regime.

Error correction in a quantum system will likely be most effective in systems with a high potential for qubit interconnectivity while also having low crosstalk between qubits. This is because high qubit interconnectivity will decrease the number of gates that need to be applied during the error correction process and having low crosstalk between qubits will reduce the potential for multi-qubit noise. In a system with high interconnectivity and low crosstalk, there will be a smaller resource overhead when implementing error correction, making error correction a more useful procedure.

3.4 Error correction in ensemble

In an ensemble system, the standard quantum error correction procedure requires modification. In single-instance systems, errors are corrected by taking a weak-measurement to determine if an error has occurred and, if so, correcting the error. This process is shown in the following:

In an ensemble system, there will be different error states on different members of the ensemble and so such a procedure is not possible. Instead of using ancilla qubits to store an error syndrome and then performing gates determined by measurement of these ancilla qubits, "blind" error correction is used. In this scheme, a series of conditional gates are applied to the entire ensemble, irrespective of whether an error has occurred to that instance. In the case of an error, the data qubit is corrected to

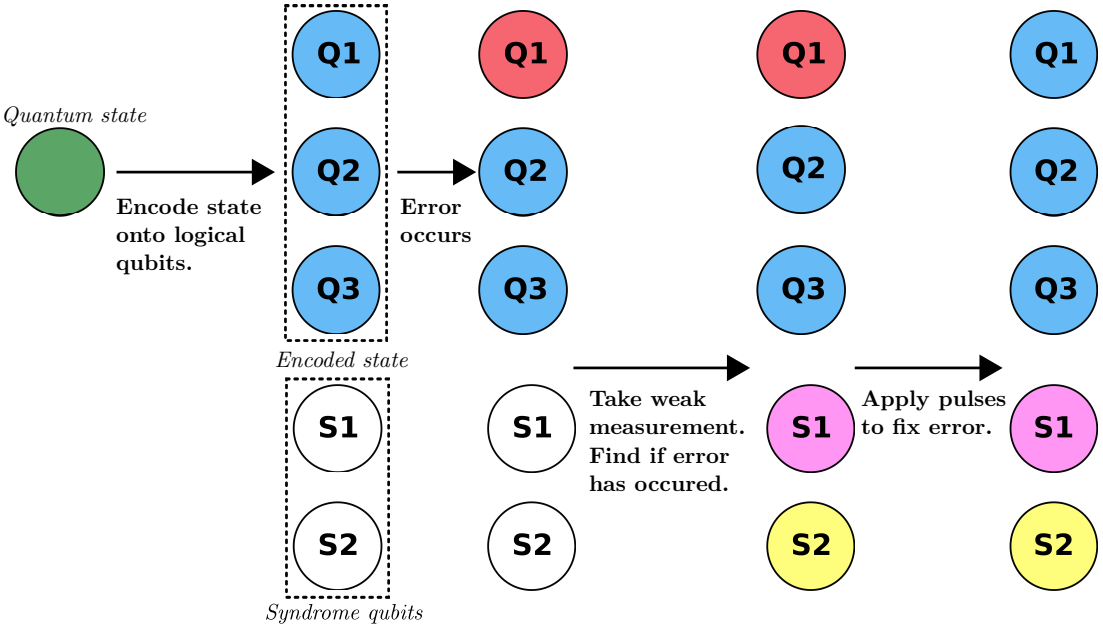

Figure 3.1: Error correction process for a single instance quantum computer

its original state and for no error, the net operation on the data qubit is an identity operation. Figure 3.2 shows this blind correction process.

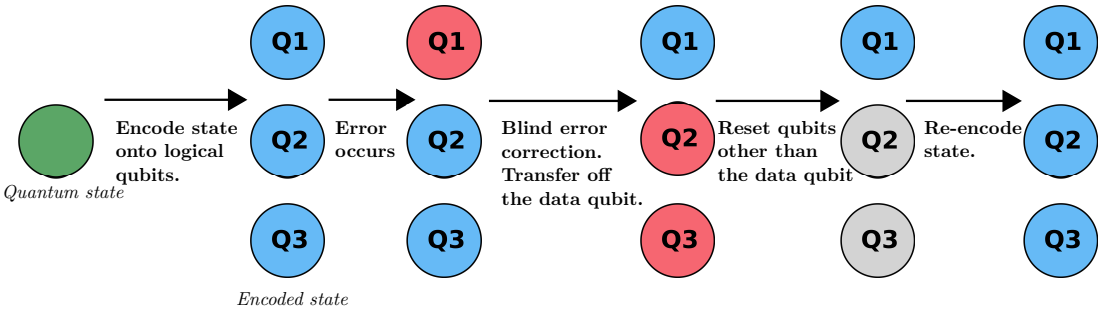

Figure 3.2: Error correction process for an ensemble quantum computer

At the end of every correction sequence, the qubits other than the data qubit are reset. For multiple rounds of correction to be feasible in an ensemble system, it is necessary that the qubit coherence time is long compared to the qubit reset time. Ensemble error correction requires that the constituent gates are of higher fidelity than in the single-instance case, as gate operations are applied to the data qubit regardless of whether an error has occurred to this qubit. The implementation of quantum error correction in a rare-earth satellite ensemble is discussed in Chapter 4.

As an example of the implementation of an ensemble error correction code, the following circuit diagram is a correction sequence for the nine-qubit Shor code:

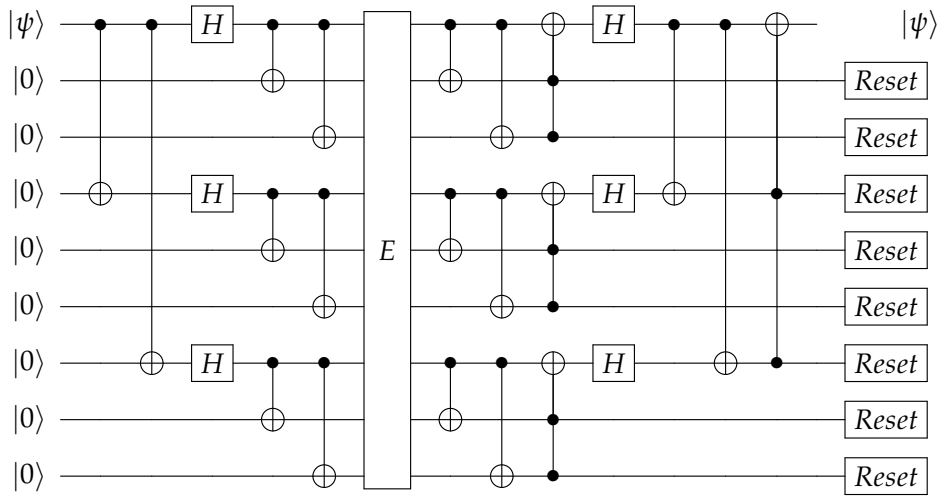

The ensemble error correction scheme can also be used in single instance error systems, in what is commonly referred to as *error correction without measurement*. In systems where the additional qubits needed for syndrome measurements are not a limiting factor, the additional gates needed for correction without measurement can be avoided, and as such, it is more common to use measurement-based error correction.

3.5 Summary

This chapter introduced the concepts relevant for implementing quantum computing. The DiVincenzo criteria for the creation of a scalable quantum computer were introduced and the problem of increasing complexity in the noise channels as the number of qubits was introduced and discussed. As the number of qubits in a quantum computing system is increased, the noise channels become increasingly complex, limiting the size of current quantum computing systems to $\mathcal{O}(50$ qubits). This problem is compounded by a high degree of crosstalk between qubits in the most well-developed systems.

The concept of a quantum gate was then introduced, with examples of common gates used to form a spanning set of operations given. The method by which errors are corrected in a quantum system was then explained, with a discussion of the current state of error correction demonstrations. There has been one demonstration of a quantum error correction protocol extending the coherence time of a qubit with system noise to date, with all other demonstrations showing only coherence time improvement against induced errors. In all quantum computing systems, there is some degree of correlation between errors on different qubits. The error correction schemes that have been demonstrated thus far fail to account for correlations between qubit errors.

The chapter concluded with a discussion on the differences between error correcting a single instance and an ensemble system. In a single instance, system error correction

is accomplished by taking a weak measurement of the encoded qubit state and then conditionally applying gates. Ensemble error correction corrects for errors by applying conditional gates such that any error is transferred to qubits other than the data qubit, which are reset at the end of a correction sequence.

Chapter 4

Quantum computing in rare-earth ensembles

This chapter describes the implementation of quantum operations in a rare-earth satellite system. The chapter begins with a historical perspective on the progress to date on implementing quantum operations in rare-earth materials in both doped and stoichiometric systems. The properties of stoichiometric satellite systems are then detailed and the performance of these systems in relation to the DiVincenzo criteria is discussed. The chapter concludes with an explanation of the procedures for implementing quantum operations in a rare-earth satellite system. The performance of the rare-earth satellite system is not explored in detail in this chapter, with it instead giving an overview of the steps to perform the operations for quantum computing. The quantum operations discussed in this chapter are a summary of the previous work in doped systems from the Kröll [33] and Sellars [93] groups, along with the theses of Longdell [34], Wesenberg [94] and Nilsson [95]. Quantum operations in stoichiometric systems were previously explored by the Sellars group [96] and in the thesis of Ahlefeldt [21].

4.1 Doped rare-earths

In a doped rare-earth system, a crystal stoichiometric in one rare-earth species is doped with a second rare-earth species, with the dopant ions used as the qubits. As discussed in earlier chapters, such systems are well developed for use as quantum memories and quantum sources. There have been previous demonstrations of the fundamental operations to implement quantum computing in such systems, with demonstrations of single-qubit [93] and multi-qubit gates [56] in doped systems.

The first demonstration of single-qubit operations in a doped system was in 1999 by Pryde et al. [93]. An isolated feature narrow in frequency compared to the experimental Rabi frequencies was prepared from the inhomogeneous line. It was then demonstrated the qubit state could be manipulated via the application of optical pulses.

In 2002 a full scheme for quantum computing in a doped rare-earth crystal was published by the Kröll group [33]. In this scheme, qubits are created from narrow

spectral features in a broad optical inhomogeneous line. Two hyperfine levels along with an auxiliary optical level were used for quantum gate operations. Controlled gates were implemented using the differing electric dipole moment of the hyperfine computing levels and the auxiliary optical level. Due to the difference in electric dipole moment, optical excitation of ions causes frequency shifts in the optical frequency of nearby ions allowing for controlled logic. The 2004 thesis of Wesenberg [94] further explored the implementation of quantum computing in doped rare-earth crystals with the introduction of phase-compensated pulses in such systems. The use of doped rare-earth systems as a quantum memory in which quantum operations can be performed was proposed in the 2005 thesis of Nilsson [95].

A modification of the Kröll scheme was demonstrated in the doctoral work of Longdell, published in 2003 [34], with this work using a different scheme for qubit preparation. In this work, narrow spectral features were prepared in a 0.1% Eu^{3+}:Y_2SiO_5 crystal and optical pulses were used to implement both single-qubit operations and a multi-qubit CROT gate.

There has since been research into the implementation of low error single-qubit gates and initialisation procedures in rare-earth ensembles with spectral features hundreds of kilohertz in width [35].

A major issue limiting the performance of rare-earth crystal systems is inhomogeneity. In a doped rare-earth system, there are two types of inhomogeneity affecting the ability to construct a good computing system: inhomogeneity in the ensemble transition frequency and inhomogeneity in the qubit-qubit optical interaction strengths. Inhomogeneity in the ensemble transition frequency causes different ions to experience a different amount of rotation on the Bloch sphere with applied pulses. Similarly, an inconsistent optical interaction strength between qubit features will cause a variable amount of rotation when performing controlled gates, dependent on the degree of optical interaction shift. Ideally, in a rare-earth system, the transition inhomogeneous linewidth would be as narrow as possible such that ions experience a consistent Rabi frequency and the optical interaction strength would also be as consistent as possible such that multi-qubit gates operate with a low error.

In a doped rare-earth system, the ions constituting each qubit are randomly distributed across the crystal, so there is a random distance between ions in qubit ensembles and hence a continuum of optical interaction strengths as shown in Figure 4.1. To be able to perform multi-qubit gates, it is necessary to have a consistent optical interaction strength across ions in the ensemble, otherwise, ions will experience a variable amount of rotation during the gate. A consistent interaction strength is achieved by selecting for a portion of the ensemble with a consistent interaction strength, in a process known as qubit distillation. The distillation for a doped system is discussed in detail in [34], with the implementation in a stoichiometric satellite system detailed later in this chapter.

The distillation process for qubits in a doped system substantially reduces the number of ions in the ensemble. In the demonstration by Longdell et al. of a CROT gate [56], the measured gate fidelity was still low following a distillation process as distillation to a level required for high fidelity gates would have left the ensemble

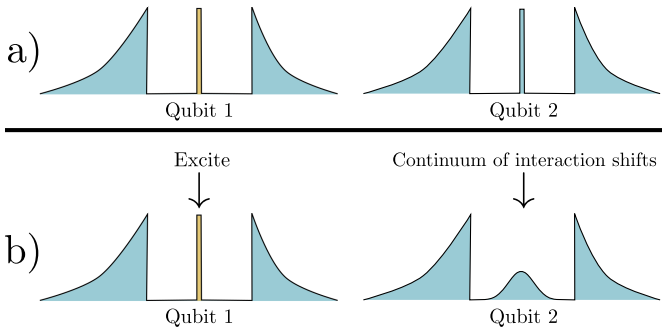

Figure 4.1: Optical frequency shifts in a doped system. The system starts with narrow features on both qubits in a). In b) the ions in the first feature are excited, causing a frequency shift in the ions in the second feature proportional to the distance between the second feature ion and the nearby feature one ions. Due to the random distribution of ions in frequency and space, this causes a distribution of optical frequency shifts in the second feature.

so small as to be undetectable with the fluorescence detection scheme used. The continuum of interaction strengths in doped ensemble systems and the subsequent need to highly distil the ensemble has limited the implementation of doped rare-earth systems to date. In a satellite system, this distillation process is unnecessary as the optical interaction strength is discrete rather than continuous.

4.2 Stoichiometric rare-earths

In a rare-earth satellite system, we take the opposite approach to doped rare-earth crystal systems: a crystal stoichiometric in the rare-earth that we wish to use is doped with a second rare-earth to create the qubit sites. The satellite lines created by the dopant rare-earth are then used as qubits.

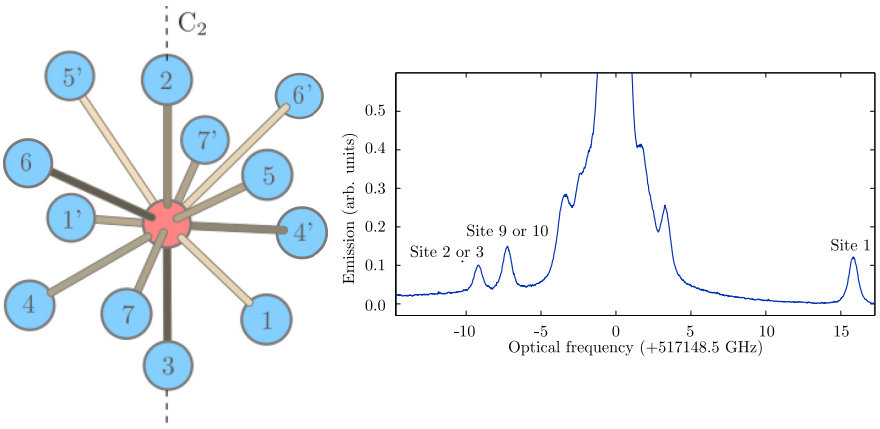

Figure 4.2: On the left, the 12 closest Eu^{3+} ions (in blue) surrounding a dopant site (in red) in $EuCl_3{\cdot}6H_2O$ (Figure modified from [97]). There are seven spectrally distinct satellite sites in this figure, with the sites labelled by distance from the dopant. The dashed sites have an identical frequency to their undashed counterparts, which they are related to by a 180° rotation about the C_2 axis. The right figure is a 1% La^{3+}:$EuCl_3{\cdot}6H_2O$ spectrum from [21] with the satellite sites labelled by the corresponding satellite site position that was determined in [21].

In the $EuCl_3{\cdot}6D_2O$ rare-earth satellite system, quantum information is stored across two $^7F_0$ hyperfine levels, which are used as the $|0\rangle$ and $|1\rangle$ qubit states. Quantum gates are implemented using pulses between the ground-state computing levels and an auxiliary optical $^5D_0$ level.

There is an optical electronic ion-ion interaction between neighbouring Eu^{3+} ions in a $EuCl_3{\cdot}6D_2O$ system. This interaction shifts the optical transition frequencies of nearby Eu^{3+} ions when a Eu^{3+} is optically excited. This conditional shift in the optical transition frequency is the mechanism through which multi-qubit gates are implemented in rare-earth satellite systems. In a rare-earth satellite system, there is a fixed spatial relationship between satellite ions and dopant ions. As a consequence of the fixed spatial relationship between ions, the optical interaction strength between qubit features is discrete: it is either a fixed value if both ions are present in a spin-cluster, or zero if one of the ions is absent. Without the need to distil for inter-qubit optical interaction strength, it is possible to create multi-qubit ensembles in these systems in which high fidelity gates can be performed.

Research to date in implementing quantum operations in satellite systems has been limited, with the 2013 measurement of satellite-satellite optical interaction shifts by Ahlefeldt et al. [55] coming the closest to a demonstration of conditional quantum logic.

It was shown in the work of Ahlefeldt et al. [55] that the optical qubit-qubit interaction has an inhomogeneity of less than 7 kHz, with the potential for the inhomogeneity to be much less than this as measurements were limited by the laser linewidth. The optical interaction shifts were determined to be additive, with excitation of two satellite ions causing an optical shift in neighbouring ions equal to

the sum of the individual optical shifts. Although this work measured many of the optical interaction shifts between satellites, the characterisation of optical interaction frequencies was incomplete, with many interactions either too weak to be measured or outside of the measurement range. Many of the satellite features with unmeasured optical interaction frequencies have desirable properties for a quantum system and it would be advantageous to measure these interactions before implementation of quantum computing in this system. The choice of satellite features as qubits for an $EuCl_3{\cdot}6D_2O$ system is discussed in Chapter 6.

In order to understand the relative performance of the rare-earth satellite system in comparison to other computing systems, we look to the DiVincenzo criteria as outlined in Chapter 3. The processes for implementing qubit initialisation, operations and readout is very similar to how these operations are implemented for doped systems [33, 34, 93], with a few differences.

The rare-earth satellite system satisfies most of the DiVincenzo criteria well. Qubits can be prepared to a single hyperfine level, optical and hyperfine coherence times are long for rare-earth qubits, a universal gate set can be implemented and individual qubit states can be read out. The one criteria that the ensemble satellite system does not currently satisfy well is scalability, with current materials only having the ability to only scale to 5-10 qubits [96]. In the following, I give a more detailed evaluation of the rare-earth satellite system under these criteria.

4.2.1 Qubit preparation and initialisation

The satellite system satisfies the second criteria of the DiVincenzo criteria well, with the ability to prepare the entire computing ensemble in a single hyperfine level through the use of optical pumping. There are two stages required to prepare a satellite ensemble for quantum computing: feature preparation and qubit distillation.

The rare-earth satellite system is an ensemble system and hence is subject to inhomogeneous broadening. To achieve low error gates, it is necessary for qubit linewidths to be $\mathcal{O}$(100 kHz) [34]. The lowest linewidth crystals of $EuCl_3{\cdot}6H_2O$ that have been grown are 25 MHz [47] in crystals isotopically pure in ^{35}Cl. Hence, even with isotopic purification, the inhomogeneous linewidth is too large to perform quantum gates. In the feature preparation stage, spectral holeburning is used to create narrow spectral features isolated in frequency from the main inhomogeneous line. Figure 4.3 demonstrates the process for spectrally holeburning narrow qubit features.

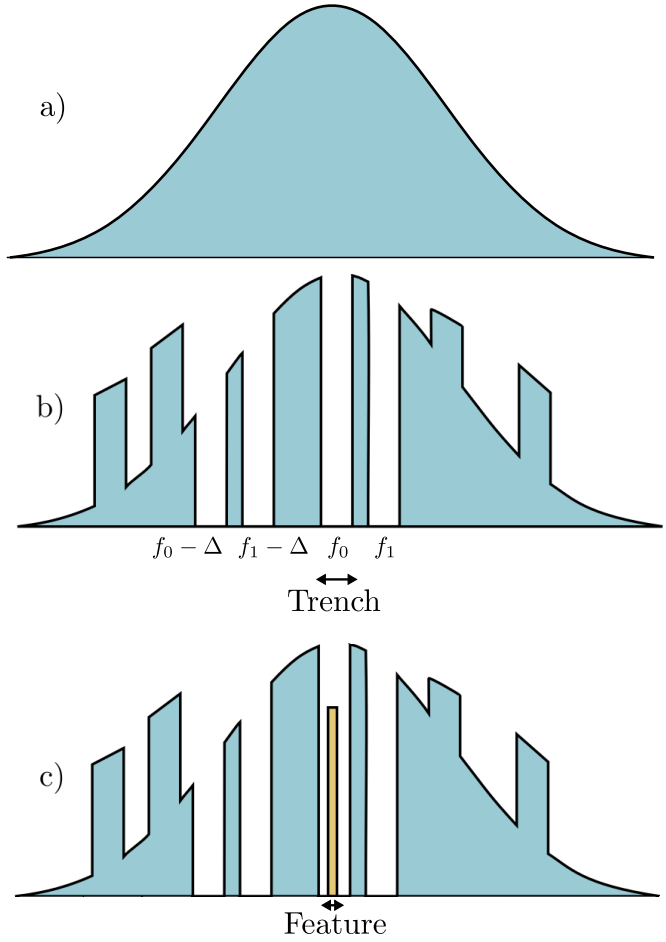

Figure 4.3: Process for creating a narrow spectral feature in an inhomogeneous line. In a) the line is initially inhomogeneously broadened. In b) optical holeburning is then used to prepare spectral trenches. For a multi-qubit system, in addition to trenches about the optical transition frequencies f_0 and f_1 (for the $|0\rangle \leftrightarrow |e\rangle$ and $|1\rangle \leftrightarrow |e\rangle$ transitions respectively), it is necessary to prepare spectral trenches at the shifted optical frequencies $f_0 - \Delta_k$ and $f_1 - \Delta_k$, where Δ_k is the optical frequency shift when qubit k is excited. Thus, in a two-qubit system, two additional trenches are needed, as illustrated in this diagram. These additional trenches are necessary for the operation of the multi-qubit gates described in 4.2.2.2. In the process of preparing a spectral trench side and anti-holes are created corresponding to combinations of the hyperfine frequencies; these additional spectral features constrain the width of trenches that may be burnt. In step c), the trench population begins in ground-state hyperfine levels other than the $|0\rangle$ computing level. To prepare a narrow spectral feature, a "burn-back" sequence is performed in which a narrow frequency range of ions are optically pumped back into the $|0\rangle$ level.

Following the creation of narrow spectral features, a distillation step is needed such that each ensemble spin-cluster has ions from each of the computing satellite features present. The spectral holeburning stage removes ions from the ensemble. If

spin-cluster ions are not perfectly correlated in their position on the inhomogeneous line, this feature preparation will result in spin-clusters in which not all of the qubit site ions are part of the system ensemble. To determine the correlation between the frequency shift in the inhomogeneous line for ions in the same spin cluster, I performed a Monte Carlo simulation of optical shifts caused by nearby isotopic impurities using the isotope shifts determined in [21]. From this simulation, I concluded that the optical inhomogeneous line shift is only weakly correlated for different satellite ions with the correlation between satellites shifts ≤ 0.14. This low inhomogeneous shift correlation means that additional qubit distillation must be performed following spectral holeburning of each qubit feature.

Qubit distillation is performed between pairs of qubits. One of the pair is first optically excited, shifting the optical excited levels of neighbouring satellite ions. Spectral holeburning is then performed at the unshifted optical frequency of the second qubit, removing ions that have not experienced an optical shift from the excitation of the first qubit. This process is then performed with the qubits flipped, initially exciting the second qubit. This distillation process can then be repeated between one of these distilled ions and additional qubits to distil a larger quantum system. Figure 4.4 illustrates this process with a pair of satellite ions.

4.2.2 Quantum gates

In order to satisfy the universal gate set DiVincenzo criteria, it is necessary to implement high fidelity multi-qubit gates in rare-earth satellite systems. In the following, the implementation of single-qubit and multi-qubit gates in rare-earth satellite systems is detailed.

4.2.2.1 Single-qubit gates

Single-qubit gates are implemented by moving population between the computing hyperfine levels via pulses applied to an auxiliary optical level. As the satellite features have a difference in optical transition frequency of order gigahertz, optical pulses applied to one qubit will have a negligible effect on other qubits.

To implement a single-qubit NOT gate in this system, we use the procedure in Figure 4.5.

4.2.2.2 Multi-qubit gates

Multi-qubit gates in satellite systems are implemented by making use of the optical frequency shift of other qubits in the spin cluster when one qubit is optically excited. In a multi-qubit gate, we wish to perform a single-qubit operation on one qubit, conditional on the states of one or more additional qubits.

In this thesis, I consider the specific example of a multi-qubit blockade gate, in which one or more qubits is optically excited in order to bring other qubits out of resonance with applied pulses. A π pulse is first applied to the control qubit(s) on the $|0\rangle \rightarrow |e\rangle$ transition. If a control qubit is in the $|0\rangle$ state, it will be optically excited

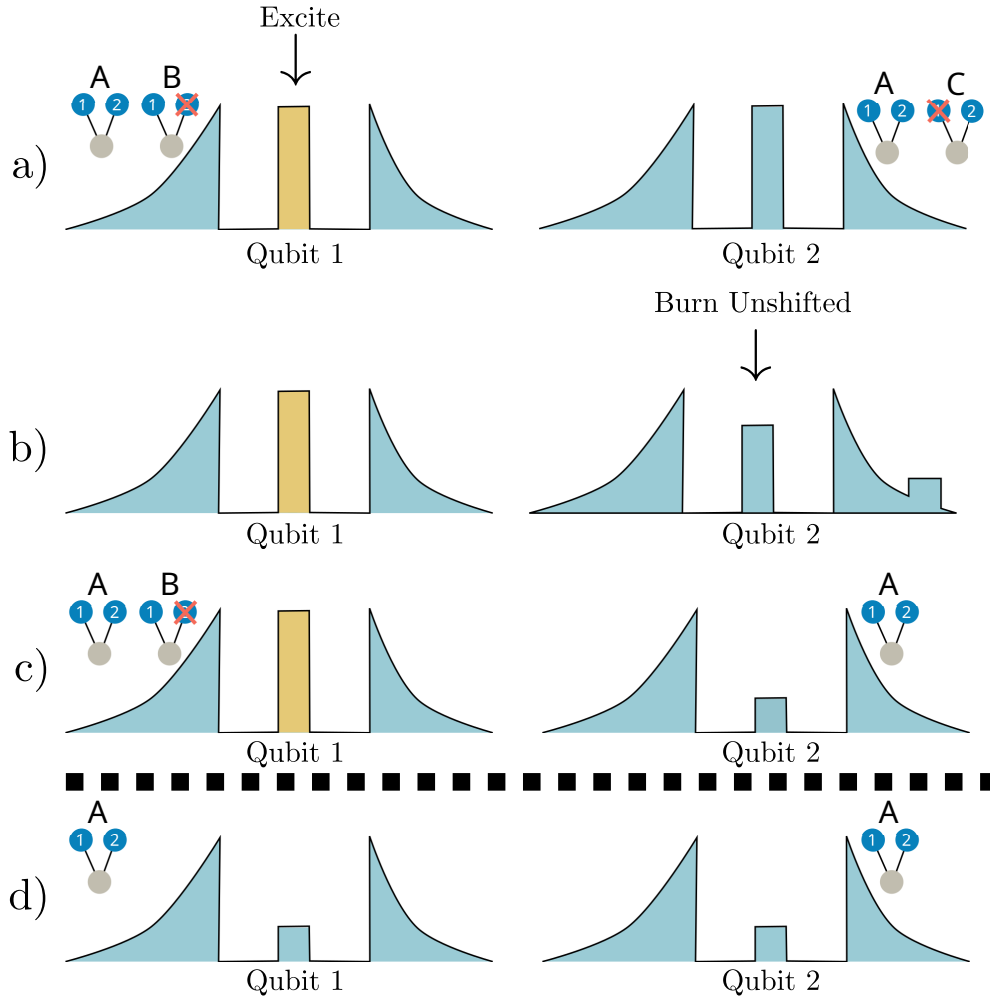

Figure 4.4: The procedure for distilling spin-cluster pairs. Initially, there are three possible cases for the ions in an individual spin-cluster: Case A, in which both the first and second ions are in the ensemble; case B, in which only the first ion is in the ensemble and case C, in which only the second ion is in the ensemble. To perform quantum computation, all ions in the ensemble qubit must be in case A. a) The ions in feature one are driven to the excited optical level, thereby shifting the optical excited levels of neighbouring satellite ions. b) The unshifted optical frequency of the second qubit is driven, burning away all ions that have not been shifted by exciting feature one. c) At this stage, feature one is at the original ensemble size and feature two has a reduced ensemble size, in which all of the feature two ions have a partner in feature one. At this stage, all sites of case C have been eliminated. d) In order to remove the case B sites, in which there is feature one population but no feature two population, this procedure is performed with the qubits reversed, initially exciting feature two and then burning away the unshifted feature one ions.

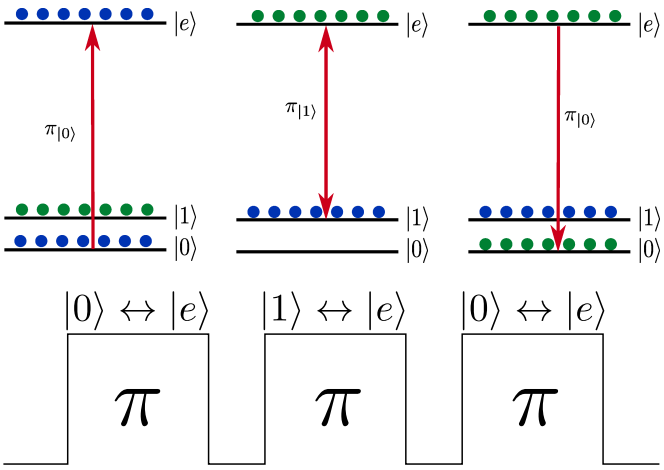

Figure 4.5: Implementation of a NOT gate in a satellite system. Consider a qubit initially in the state $A|0\rangle + B|1\rangle$. An optical π pulse is first applied to the $|0\rangle \leftrightarrow |e\rangle$ transition, such that the qubit is in state $A|e\rangle + B|1\rangle$. Applying a $|1\rangle \leftrightarrow |e\rangle$ π pulse then inverts the population of the $|1\rangle$ and $|e\rangle$ levels, giving $A|1\rangle + B|e\rangle$. Finally a second $|0\rangle \leftrightarrow |e\rangle$ π pulse is applied, leaving the qubit in the inverted state $A|1\rangle + B|0\rangle$.

and shift the optical frequency of the target qubit. The desired single-qubit gate is then performed using the unshifted optically transition frequencies. Finally, a pulse is performed on the control qubit, which will return it to the optical ground level if it was initially excited. As an example of this implementation scheme for multi-qubit gates, Figure 4.6 displays the applied pulses and population movement for a CNOT gate.

As previously stated in this chapter, the shift in optical interaction frequencies by excitation of ions in a spin cluster is additive, with the optical frequency shift created by exciting two ions simply the sum of the two interaction shifts. It is possible to create gates controlled by more than a single qubit using this additive frequency shift, such as the Toffoli (CCNOT) gate.

If high fidelity multi-qubit gates can be implemented in rare-earth satellite systems, then these systems are also able to satisfy the universal gate set DiVincenzo criteria. High fidelity multi-qubit gates are still yet to be demonstrated, however with the increased homogeneity of the satellite system compared to a doped system; it is expected that the gate fidelity demonstrated in [56] will see substantial improvement.

4.2.3 Readout

There are several potential methods that can be used to read out a stoichiometric ensemble, which can be classed into two groups: coherent and incoherent. Both of these readout schemes allow for the readout of specific qubit states, satisfying the qubit-specific readout DiVincenzo criteria. The choice of whether to use a coherent or incoherent scheme requires balancing several factors.

Coherent readout schemes measure a coherent transient emission from the ensemble

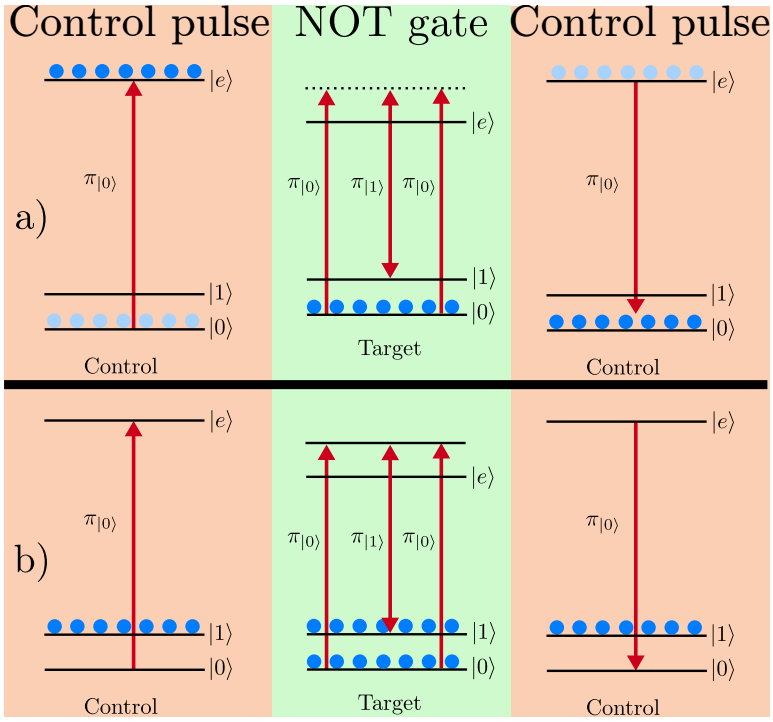

Figure 4.6: Implementation of a CNOT gate in a satellite system. There are two cases that must be considered, case a) in which the control qubit population is initially in the $|0\rangle$ state and case b) in which the control qubit is initially in the $|1\rangle$ state. At the start of the sequence, a π pulse is applied to the control qubit $|0\rangle \leftrightarrow |e\rangle$ transition. If the control qubit was in the $|0\rangle$ state, the optical transition frequencies of the target qubit will be shifted by this excitation. A NOT gate sequence is then applied to the target qubit. If the control qubit is initially in $|0\rangle$, these pulses are not resonant as the transition frequencies have changed, so this gate will have no effect. For the control qubit initially in the $|1\rangle$ state, the initial π pulse will have done nothing as it was non-resonant. The π pulses applied to the target qubit are resonant in this case and the NOT gate sequence succeeds. To finish the sequence, a π pulse is applied to the $|0\rangle \leftrightarrow |e\rangle$ transition, returning the control qubit to the optical ground level if it was excited by the initial pulse.

and use this to infer information about the quantum state of the ensemble. Examples of coherent readout schemes are measuring a photon echo or free induction decay. The use of a coherent readout scheme allows for a full measurement of the qubit state. Coherent readout schemes have the benefit that very sensitive measurements can potentially be achieved through the use of heterodyne detection and optical cavities. With such schemes, there is the potential for the entire quantum state to be measured in each experimental repetition. A difficulty in the use of coherent schemes is the high sensitivity to noise. There are several potential noise sources for coherent measurements, such as vacuum noise, laser intensity, phase fluctuation and noise on the detection electronics. Additional complications with the use of a coherent detection scheme are that not all of the ensemble will emit for a measurement and that for small numbers of ions, the coherent emission is less spatially and temporally constrained.

Incoherent readout schemes measure an incoherent emission from the ensemble to infer the quantum state of the ensemble. Incoherent readout schemes all use some variant of photon-counting on the emission from an ensemble. Unlike with coherent schemes, only the $\hat{z}$ component of the qubit state on the Bloch sphere can be measured in incoherent schemes. To reconstruct the full quantum state in an incoherent scheme, multiple measurements of projections onto the Bloch sphere are taken. Gate operations are applied to the quantum state to perform rotations before the incoherent measurement is taken, thus allowing for different projections of the Bloch sphere to be measured when the incoherent readout of the $\hat{z}$ component is taken. In addition to the need for multiple types of measurements for incoherent readouts, when the ensemble is small, measurements must be performed several times to have sufficient statistics for the true value of the Bloch sphere projection. As detailed earlier in this chapter, satellite ensembles must be distilled for both the linewidth of individual computing features and ions occupying the same satellite site. This process leads to an ensemble size of $N_{ensemble} = N_{original}\left(\frac{\Gamma_q}{\Gamma_{inh}}\right)^n$ (Where Γ_{inh} is the satellite inhomogeneous optical linewidth and Γ_q is the feature linewidth). In the case of a large ratio of feature linewidth to inhomogeneous optical linewidth, the system preparation process quickly leads to small ensemble sizes, which will require many repetitions of each measurement on the ensemble to gather sufficient statistics.

Due to incoherent readouts measuring spontaneous emission from the ensemble, which is dependent on the optical lifetime and the need to repeat measurements many times for small ensembles, incoherent schemes are much slower than using a coherent readout. On the other hand, incoherent detection schemes have fewer potential noise sources than coherent schemes. In the past, photon-counting was limited by the non-negligible dark counts of detectors, limiting the time that photon emission could be measured before the probability of registering a dark count exceeded the probability of detecting an emitted photon. In recent years detectors with zero dark counts have been demonstrated [98], meaning that, in principle, an incoherent measurement can take an arbitrarily long time. Incoherent schemes are not sensitive to vacuum noise and are less susceptible to noise on the laser and detection apparatus. The remaining

source of noise is from the detection of photons not from the computing ensemble. There is less frequency selectivity when performing photon counting measurements; hence this noise source is more problematic in incoherent measurements.

Incoherent fluorescence readout has a reduced complexity compared to coherent schemes and has been successfully used for ensemble rare-earth computing [56, 99–101]. Due to this, the use of this readout scheme was assumed in this work for evaluation of the $EuCl_3 \cdot 6D_2O$ system. Fluorescence readout is accomplished by applying a π pulse between one of the computing levels and the auxiliary optical level. The qubit ensemble is then allowed to decay, producing fluorescence. Comparing the amount of fluorescence with the measured fluorescence when all of the qubit population is in the optical excited-state allows for the projection of the qubit state onto the $\hat{z}$ axis of the Bloch sphere to be determined.

4.2.4 Scalability

The only DiVincenzo criterion that the rare-earth satellite system is not currently well-positioned to satisfy is criterion one: "a scalable physical system with well-characterised qubits.". The number of independently addressable qubits in a satellite system is limited by the number of resolved satellite lines and the optical inhomogeneous linewidth. The number of satellite lines that can be independently addressed is dependent on how widely spaced in optical transition frequency the satellite lines are. In prior spectroscopy on rare-earth crystals, measurement of 30 or more resolved satellite lines has been common [97, 102]. As explained in Section 4.2.3 after distillation the number of ions in a satellite computing ensemble is $N_{original}\left(\frac{\Gamma_q}{\Gamma_{inh}}\right)^n$. The number of qubits that can be used in a satellite system before the ensemble size is too small to measure is, therefore, limited by the optical inhomogeneous linewidth of satellite lines. In $EuCl_3 \cdot 6H_2O$ crystals that have been grown to date, a large amount of distillation must be performed and consequently, the qubit number is limited to only $5-10$ qubits [21]. The growth of crystals with a narrower optical linewidth will allow for the use of larger ensemble sizes after distillation and the subsequent creation of higher qubit number systems.

4.2.5 Quantum networks

Compatibility with a quantum network is not necessary for the construction of a quantum computing system and is not the primary focus of this thesis. Nonetheless, the sixth and seven criteria DiVincenzo (pertaining to compatibility with a quantum network) can be satisfied by $EuCl_3 \cdot 6D_2O$ as optical photons can be read in and read out using the $^7F_0 \rightarrow {}^5D_0$ transition.

Although this system is compatible with visible wavelength quantum networks, it would be preferable if it was also compatible with 1550 nm Telecom band networks due to the very low attenuation (≈ 0.2 dB/km [103]) of fibre optic cable in this band. Through the use of erbium as the dopant species, it is possible for this system to be compatible with the 1550 nm networks. The dopant erbium ion would be used as

a "quantum bus": a SWAP gate is performed between the erbium dopant and the qubit to be measured, transferring the qubit state to the erbium. Performing a readout on the erbium ion then allows the qubit state to be read out at telecom wavelengths. Read-in at telecom wavelengths can be accomplished using the reverse of this process: a quantum state is first read in onto the dopant erbium and then SWAP gates are performed to transfer this state to the relevant qubits. This quantum bus technique features prominently in NV systems, with the NV centre used to address the quantum system [58–60]. Additionally, this quantum bus approach has been proposed for the readout of single rare-earth ions [99, 104–106] and ensemble rare-earth systems [107].

4.2.6 Criteria for a small quantum processor

DiVincenzo's criteria pertain to constructing a large quantum computer, however, there are several applications for which large-scale quantum computing is not necessary and a small quantum system of high quality is useful. Examples of such applications are as a testbed for quantum error correction and performing linear quantum optics on a quantum memory. In light of this, we define the following criteria for a small quantum processor:

1. A system with well-characterised qubits which can be scaled to a moderate number.
2. The ability to initialise the state of the qubits to a simple fiducial state, such as $|000...\rangle$.
3. Long relevant decoherence times, much longer than the gate operation time.
4. A "universal" set of quantum gates.
5. A qubit-specific measurement capability.
6. Low crosstalk between qubits.
7. High qubit interconnectivity.

For a small quantum processor, it is desirable to have low qubit crosstalk such that operations in this system can be implemented with minimal system corruption. High qubit interconnectivity allows operations on the moderate number of qubits to be performed with a minimal number of gates and for applications such as tests of error correction protocols to be explored in many different regimes.

The satellite system is very well suited for application as a small quantum processor for the purpose of tests of error correction protocols. Full scalability is not necessary for such an application and the potential for $5 - 10$ qubits is sufficient to make this a useful system for error correction tests. This system has low crosstalk between qubits as the hyperfine transitions experience minimal perturbation due to excitation of surrounding ions [32]. The minimal perturbation in the hyperfine frequencies means that performing quantum gates has a negligible effect on uninvolved qubits.

The qubits in this system are highly interconnected, with $\mathcal{O}$(MHz) interaction shifts between each satellite and at least the surrounding shell of nearby ions. In addition, the additive interaction shifts between qubits mean that many-qubit gates such as the Toffoli (CCNOT) gate can be implemented with fewer pulses, reducing the error when performing these gates.

4.2.7 Summary

This chapter described the implementation of quantum operations in both doped and stoichiometric satellite systems. In a doped system, there is a broad continuum of optical interaction strengths, meaning that sub-ensembles must be prepared with more consistent optical interaction strengths — the need to distil for optical interaction strength results in very small ensembles in doped systems. Stoichiometric satellite systems have a consistent optical interaction strength between ions in the same spin cluster and require less spectral preparation, resulting in larger ensemble sizes. Qubits are prepared in a stoichiometric satellite system using spectral hole-burning on each qubit followed by a distillation process to remove spin clusters that do not have population at all of the qubit sites in the system ensemble.

Quantum gates are implemented in satellite rare-earth systems using optical pulses between two hyperfine transitions via an auxiliary optical level. There is an optical interaction shift from excitation of satellite ions within the same cluster allowing for controlled gates. Read-out of the satellite system can be accomplished via either coherent or incoherent measurements. An incoherent fluorescence readout was considered in this thesis as its performance could be quantified with fewer assumptions than in a coherent readout.

The example $EuCl_3{\cdot}6D_2O$ system that we are considering in this thesis has the potential to satisfy all of the DiVincenzo criteria other than the ability to scale, as the need to perform large amounts of distillation limits the number of possible qubits. There are potential applications where the need to scale to large qubit numbers is not necessary. For these applications, a set of criteria for small quantum processors was proposed. The small quantum processor criteria modifies the first DiVincenzo criteria to require only a moderate number of qubits and adds the requirements that qubits have low crosstalk and are highly interconnected. The rare-earth satellite systems are well suited for application as small quantum processors.

Chapter 5

System manipulation

This chapter details how applied magnetic fields can be used to reduce the gate error in rare-earth crystal systems. The effect of an applied magnetic field on the rare-earth energy levels is described by the final four terms of equation 2.1 (the hyperfine, nuclear electric quadrupole, nuclear Zeeman and electronic Zeeman interactions). The application of a magnetic field allows the system hyperfine splittings and mixing of the hyperfine states to be manipulated, which in turn changes the relative oscillator strengths for transitions. By applying specific magnetic fields, the hyperfine splittings and relative oscillator strengths can be altered to values more favourable to performing low-error quantum gates.

The objective of applying a magnetic field is to reduce off-resonant excitation to both neighbouring hyperfine levels and the other computing level. Off-resonant excitation is a function of two system parameters, the energy splittings between hyperfine levels and the oscillator strengths between the excited optical levels and ground-state hyperfine levels. To minimise off-resonant excitation, the splittings between hyperfine levels should be as large as possible, with, in the worst-case off-resonant excitation scaling with the square of hyperfine splitting [108]. The oscillator strengths affect off-resonant excitation in two ways, with both the absolute oscillator strength of auxiliary optical to ground-state multiplet transitions and relative oscillator strengths needing to be considered. In order for large Rabi frequencies to be achievable, it is desirable for the absolute oscillator strengths to be as large as possible. Ideally the relative oscillator strengths would be such that we have an "ideal" Λ system, with equal oscillator strengths between the $|0\rangle \rightarrow |e\rangle$ and $|1\rangle \rightarrow |e\rangle$ transitions and zero oscillator strength to the other hyperfine levels. At zero-field, it is not common to find rare-earth systems with both the desired large hyperfine splittings and oscillator strength structure. Through the use of applied magnetic fields, rare-earth systems can be manipulated to improve these system parameters for quantum gates [109, 110].

5.1 Measuring gate performance

5.1.1 Performance metric

To evaluate the suitability of a quantum system for performing quantum gates, it is necessary to define a suitable metric. The metric chosen for the following analysis is the quantum gate error (QGE), defined as:

$$E = \frac{1}{2} \max_{\rho} \left| U\rho U^{\dagger} - \nu(\rho) \right|, \tag{5.1}$$

where ρ is the density matrix describing the ensemble qubit state, U is a unitary operator representing the ideal gate, and $\nu(\rho)$ is the physically realised ensemble state after the operation.

It is common to see the quantum gate fidelity (QGF) used as a metric for the performance of quantum operations. The QGF was not used in this analysis as it is insensitive to certain forms of error [111, 112]. There are two additional reasons to use QGE over QGF: it obeys the triangle inequality, so the error of applying n gates is bounded by the sum of the error of those gates, and it directly bounds the probability that the quantum error correction process has failed $|P_{\text{fail}}| \leq 2E$. The QGE is greater than or equal to the infidelity $1 - F$, with $1 - E \leq F \leq \sqrt{1 - E^2}$ [113].

The QGE allows us to establish an upper bound for the error when performing a quantum gate. In particular, we are interested in using rare-earth satellite systems for tests of error correction algorithms. The three-qubit bit-flip sequence introduced in Chapter 3 is used as our metric of performance. An optimised pulse sequence to implement this bit-flip protocol is displayed in Figure 5.1. Section 6.4 details how this pulse sequence was optimised to reduce the number of pulses.

This sequence is a series of seventeen π pulses about the $\hat{x}$ axis: eight on $|0\rangle \leftrightarrow |e\rangle$ transitions and nine on $|1\rangle \leftrightarrow |e\rangle$ transitions, applied across the three system qubits, as shown in Figure 5.1. The large inter-qubit interaction strength means that the dominant error mechanism in any pulse sequence is the error on single-qubit gates, which is later established in Chapter 6. Therefore a pulse sequence composed of seventeen π pulses also provides a representative demonstration of the system performance.

To determine the necessary QGE for this correction sequence to be useful, the threshold error value for an improvement in coherence time can be calculated. To estimate this threshold value, we assume that the only spontaneous error in the system is a pure bit-flip. It is important to note that this is not a physical error in a rare-earth ion crystal: pure phase errors (due to dephasing) and arbitrary errors (due to spin-phonon interactions) are natural errors in spin systems like rare-earth ions, but not pure bit-flip errors. It is further assumed that the error correction either restores the original state or takes the system to an orthogonal, unrecoverable state with a probability of ϵ, the sequence error of the previous section. Then, there are two possible states we need to consider for each qubit: the original state ρ_0 and the orthogonal flipped state ρ_f. The probabilities of the qubit occupying those two states

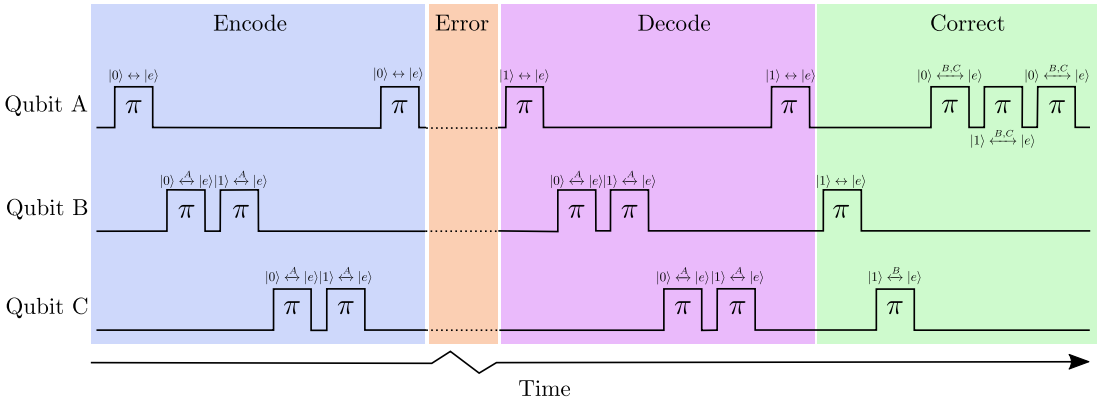

Figure 5.1: Pulse sequence to implement the three-qubit bit-flip error correction protocol. Qubit A is the data qubit and Qubits B and C are the ancilla qubits. Overset letters are used to indicate shifted transitions. For example, a $|1\rangle \overset{A}{\leftrightarrow} |e\rangle$ pulse on qubit B means the $|1\rangle \leftrightarrow |e\rangle$ transition driven at the resonant frequency when qubit A is excited.

with time are:

$$p_0(t) = \frac{1}{2}\left(1 + e^{-\frac{t}{T_E}}\right) \tag{5.2}$$

$$p_f(t) = \frac{1}{2}\left(1 - e^{-\frac{t}{T_E}}\right), \tag{5.3}$$

where T_E is the time constant describing the bit-flip error. If the error correction sequence is applied, the state is first encoded across three qubits and the probability that the system is in a correctable state (zero or one error) is:

$$P_c(t) = p_0^3 + 3p_0^2 p_f. \tag{5.4}$$

For an error correction sequence applied at time Δt, a lower bound for the probability that the state is corrected is then given by $(1-\epsilon)P_c(\Delta t)$. From this equation, we can determine an approximate effective coherence time for the corrected system T_{eff}:

$$T_{eff} \approx \frac{-\Delta t}{\ln\left(2(1-\epsilon)P_c(\Delta t) - 1\right)}. \tag{5.5}$$

Solving this equation numerically for the correction time Δt gives that the coherence time is improved only when $\epsilon < 0.11$.

5.1.2 Gate simulation

To determine the performance of La^{3+}:$EuCl_3{\cdot}6D_2O$ for different choices of computing and auxiliary levels and driving Rabi frequencies, pulses were modelled in an inhomogeneously broadened ensemble of satellite ions in La^{3+}:$EuCl_3{\cdot}6D_2O$. The model used was based on the optical Bloch equations with decoherence.

From the optical Bloch equations, the Hamiltonian of an n-level atom interacting with an electromagnetic field of frequency ω [114] is:

$$H = H_0 + H_I = \begin{pmatrix} \omega_0 & \Omega_{01}e^{i\omega t} & \cdots & \Omega_{0n}e^{i\omega t} \\ \Omega_{01}^* e^{-i\omega t} & \omega_1 & & \Omega_{1n}^* e^{-i\omega t} \\ \vdots & & \ddots & \vdots \\ \Omega_{0n}^* e^{-i\omega t} & \Omega_{1n}^* e^{-i\omega t} & \cdots & \omega_n \end{pmatrix}, \tag{5.6}$$

where ω_i is the transition of the i-th level, and Ω_{ij} is the Rabi frequency driving the transition between the i-th and j-th levels.

In order to model an ensemble, we use the density matrix formalism. The ensemble density matrix ρ is a weighted sum of pure states, with $\psi = \sum_j p_j \left|\psi_j\right\rangle \left\langle\psi_j\right|$ where p_j is the probability of an ion in the ensemble being in that pure state.

The evolution of the density matrix is given by $\frac{\partial \rho}{\partial t} = -i[H, \rho]$. To reduce simulation complexity, we work in the interaction picture, with time-dependent factor $e^{i\omega_0 t}$ (where ω_0 is the difference in frequency between the lowest energy ground-state level and the lowest energy excited-state level).

In this basis, the evolution of the qubit density matrix ρ_I is given by:

$$\frac{\partial \rho_I}{\partial t} = -i \left[\begin{pmatrix} 0 & \Omega_{01}e^{i(\omega-\omega_1+\omega_0)t} & \cdots & \Omega_{0n}e^{i(\omega-\omega_n+\omega_0)t} \\ \Omega_{01}^* e^{-i(\omega-\omega_1+\omega_0)t} & 0 & & \Omega_{1n}^* e^{-i(\omega-\omega_n+\omega_1)t} \\ \vdots & & \ddots & \vdots \\ \Omega_{0n}^* e^{-i(\omega-\omega_n+\omega_0)t} & \Omega_{1n}^* e^{-i(\omega-\omega_n+\omega_1)t} & \cdots & 0 \end{pmatrix}, \rho_I \right], \tag{5.7}$$

where Ω_{ij} is the coupling constant between levels i and j and ω_{ij} is the difference in frequency between levels i and j.

When applying an optical pulse between the ground-state hyperfine levels and excited optical levels, the coupling constants Ω for ground-ground and excited-excited transitions are set to zero due to the negligible amount of population that will be driven between these levels. Similarly, when applying an RF pulse, the Ω between states in different multiplets are set to zero.

To model the effects of decoherence and dephasing in this system, we use the Lindblad master equation [114], with density matrix evolution given by Equation 5.8. In a system with M decoherence sources the density matrix time evolution is given by the Lindblad equation:

$$\frac{\partial \rho_I}{\partial t} = -i[H, \rho_I] + \mathcal{L}(\rho_I) = -i[H, \rho_I] + \sum_{k=1}^{M} \left(L_k \rho_I L_k^\dagger - \frac{1}{2} L_k^\dagger L_k \rho_I - \frac{1}{2} \rho_I L_k^\dagger L_k \right), \tag{5.8}$$

where the $\mathcal{L}$'s are the Lindblad operators.

There are two relevant Lindblad operators used for this system. The relaxation

operator is given by:

$$L_{relaxation} = \sqrt{\Gamma_{mn}}\sigma^{-}_{mn},$$

where m and n are ground or excited-state levels with $m > n$ and $\Gamma_{mn} = 1/T_1$. The second Lindblad operator is the dephasing operator which is given by:

$$L_{dephasing} = \sqrt{\frac{\Gamma^{\phi}_{mn}}{2}}\sigma^{z}_{mn},$$

where m and n are ground or excited-state levels with $m > n$ and $\Gamma^{\phi}_{mn} = \frac{1}{T_2} - \frac{1}{2T_1}$.

In this model, the six ground-state and six excited-state levels of Eu^{3+} under applied magnetic field are considered, as off-resonant excitation is a major source of error in this system.

The sample was assumed to be optically thin, with no spatial variation in Rabi frequency accounted for in simulations.

As the QGE obeys the triangle inequality, the error of the full 17 π pulse sequence can be bounded using the error of the π pulses on the $|0\rangle \leftrightarrow |e\rangle$ transitions and $|1\rangle \leftrightarrow |e\rangle$ transitions so it suffices to calculate these errors to bound the total QGE.

The pulses considered in calculating QGE were only basic square and Gaussian shapes. Gaussian pulses were found to have consistently lower QGE due to a reduction in off-resonant excitation and so were used in the following analysis of the system performance at zero-field and applied field.

5.2 Zero-field

Prior to analysis of the effect of an applied field, it is instructive to analyse the system performance at zero-field in order to illustrate why an applied field is necessary.

At zero-field, $EuCl_3{\cdot}6H_2O$ has three ground and three excited-states, of which we are free to choose two ground-states and one excited-state for our computing system. At zero-field, the splittings between neighbouring hyperfine levels are all of a similar magnitude; hence the main consideration for QGE is that the relative oscillator strengths of the $|0\rangle \leftrightarrow |e\rangle$ and $|1\rangle \leftrightarrow |e\rangle$ transitions are as close to 0.5 as possible.

The zero-field hyperfine structure of $EuCl_3{\cdot}6H_2O$ was previously introduced in Figure 2.7. The oscillator strengths for $EuCl_3{\cdot}6H_2O$ at zero-field are displayed in Table 5.1.

At zero-field the optimal Λ system is the $\pm\frac{1}{2}$ and $\pm\frac{3}{2}$ ground-state levels used for the computing levels $|0\rangle$ and $|1\rangle$ respectively, and the excited-state $\pm\frac{1}{2}$ level used as the auxiliary optical state $|e\rangle$.

To determine the error rate of this choice of Λ system with different Rabi frequencies and linewidths of the ensemble features, simulations were performed with a 500 ion ensemble with a tophat feature lineshape. A 500 ion ensemble was used for this simulation to strike a balance between capturing the ensemble behaviour due to frequency inhomogeneity and the simulation completing in a tractable length of time.

Table 5.1: Relative optical oscillator strengths at zero-field for both Eu isotopes in $EuCl_3{\cdot}6H_2O$. The row labels indicate ground-state levels, the columns excited-state levels. The absolute oscillator strength of the $EuCl_3{\cdot}6H_2O$ $^7F_0 \rightarrow {}^5D_0$ transition is $\approx 1.9 \times 10^{-9}$ [21].

	$\lvert\pm5/2\rangle$	$\lvert\pm3/2\rangle$	$\lvert\pm1/2\rangle$
$\lvert\pm5/2\rangle$	0.94	0.06	0
$\lvert\pm3/2\rangle$	0.05	0.88	0.07
$\lvert\pm1/2\rangle$	0.01	0.06	0.93

For this choice of Λ system, Figure 5.2 shows the error rates of individual π pulses on the two optical transitions $|0\rangle \leftrightarrow |e\rangle$ and $|1\rangle \leftrightarrow |e\rangle$ respectively, as a function of Rabi frequency and the linewidth of the ensemble features, when simulating a 500 atom ensemble with a tophat feature lineshape.

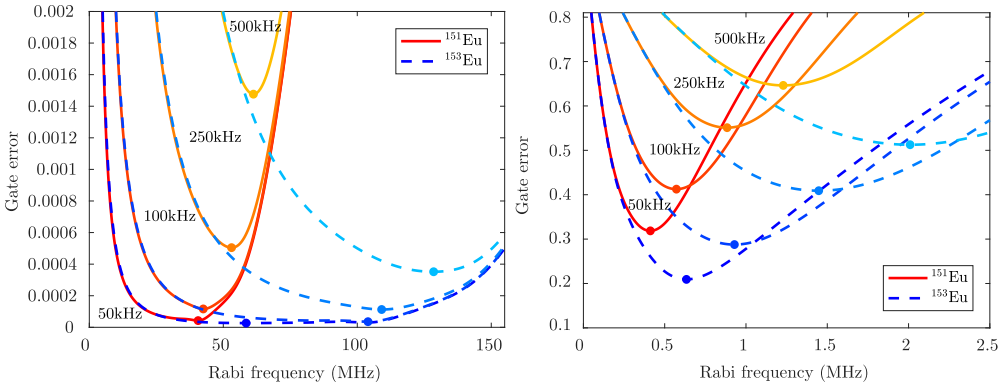

Figure 5.2: QGE in zero-field for ^{151}Eu (red family of solid lines) and ^{153}Eu (blue family of dashed lines) as a function of Rabi frequency, for different choices of the ensemble inhomogeneous width (marked on figure). a) For the $|0\rangle \leftrightarrow |e\rangle$ transition, b) for the $|1\rangle \leftrightarrow |e\rangle$ transition. For each choice of isotope and ensemble width, the QGE goes through a minimum with Rabi frequency, marked by the filled circles.

To interpret the behaviour we see when driving this system, we consider the initial population in either in $|0\rangle$ or $|1\rangle$, and the Gaussian π pulse aims to drive it into $|e\rangle$. When the Rabi frequency is low, the π pulse has to be long, and dephasing during the pulse dominates the error. This error decreases with increasing Rabi frequency, but at the same time, off-resonant excitation of other transitions increases, which soon dominates the QGE. This leads to a minimum error at a Rabi frequency determined by the hyperfine splitting of the $|0\rangle$ and $|1\rangle$ levels. Since ^{153}Eu has larger hyperfine splittings than ^{151}Eu, the off-resonant excitation is lower and so is the QGE. Reducing the ensemble width also reduces the error, as ions at the edge of the spectral feature are excited off-resonantly, so the π pulse does not drive them entirely into the excited-state.

The error is much lower when driving the $|0\rangle \leftrightarrow |e\rangle$ transition (Figure 5.2) than

the $|1\rangle \leftrightarrow |e\rangle$ transition, and the Rabi frequency that gives the minimum error is two orders of magnitude higher. The reason is the relative oscillator strengths of the driven transition, the other computing transition, and other transitions in the system. The $|0\rangle \leftrightarrow |e\rangle$ transition is strong, whereas the surrounding transitions that can contribute to the error are all weak. The situation is reversed for when driving the $|1\rangle \leftrightarrow |e\rangle$ transition: both the $|0\rangle \leftrightarrow |e\rangle$ and the transition from $|1\rangle$ to the second excited-state $\left|\pm\frac{3}{2}\right\rangle$ are strong and near in frequency, so off-resonant excitation of these transitions causes errors at even low Rabi frequencies.

The error on the $|1\rangle \leftrightarrow |e\rangle$ transition is larger than the minimum error required to usefully implement an error correction sequence, even with a 10 kHz linewidth ensemble. Driving the $|1\rangle \leftrightarrow |e\rangle$ transition is unavoidable in any error correction protocol. The poor oscillator strength of this transition in zero-field renders this regime unsuitable for error correction. No other choice of computing states gives any substantial improvement in the error because the oscillator strength is so strongly concentrated in $\Delta m_I = 0$ transitions. In the next section, we show that the oscillator strength of this transition can be improved by applying a magnetic field.

5.3 Applied field

The system performance at zero-field demonstrates that the mixing between hyperfine levels is insufficient to allow for low error quantum gates, with there being a high error between levels with different m_I values. Application of a magnetic field can be used to induce further mixing of the hyperfine levels, allowing for reduced QGE. The use of applied magnetic fields to manipulate system parameters for quantum computing applications has also been explored in [109, 110, 115]

The energy levels of a rare-earth crystal can be described by Equation 2.1 from Chapter 2

$$H = H_{FI} + H_{CF} + (H_{HF} + H_Q + H_z + H_Z).$$

This Hamiltonian describes the behaviour of the entire 4f configuration. In this instance, we are only considering the hyperfine structure of a single optical transition, and as such, a spin Hamiltonian acting in the reduced space of the nuclear spin can be used to model the ground and excited-states. In this model, electronic contributions to the hyperfine structure are parametrised, leading to a Hamiltonian of the form:

$$H' = (B \cdot Z \cdot B)\,\hat{E} + B \cdot M \cdot \hat{I} + \hat{I} \cdot Q \cdot \hat{I}, \tag{5.9}$$

where B is the magnetic field, Z the quadratic Zeeman tensor, M the enhanced nuclear Zeeman tensor, $\hat{I}$ the nuclear spin operator, $\hat{E}$ the identity operator and Q the effective quadrupole tensor.

The crystal tensors take the following forms in $EuCl_3{\cdot}6H_2O$:

$$Z = R(\alpha, \beta, \gamma_m) \begin{bmatrix} Z_x & 0 & 0 \\ 0 & Z_y & 0 \\ 0 & 0 & Z_z \end{bmatrix} R^T(\alpha, \beta, \gamma_m) \tag{5.10}$$

$$M = R(\alpha, \beta, \gamma_m) \begin{bmatrix} g_x & 0 & 0 \\ 0 & g_y & 0 \\ 0 & 0 & g_z \end{bmatrix} R^T(\alpha, \beta, \gamma_m) \tag{5.11}$$

$$Q = R(\alpha, \beta, \gamma_q) \begin{bmatrix} -E & 0 & 0 \\ 0 & E & 0 \\ 0 & 0 & D \end{bmatrix} R^T(\alpha, \beta, \gamma_q), \tag{5.12}$$

where $R(\alpha, \beta, \gamma)$ is a rotation matrix defined by three Euler angles of the form:

$$R(\alpha, \beta, \gamma) = \begin{bmatrix} \cos(\alpha) & -\sin(\alpha) & 0 \\ \sin(\alpha) & \cos(\alpha) & 0 \\ 0 & 0 & 1 \end{bmatrix} \times \begin{bmatrix} \cos(\beta) & 0 & \sin(\beta) \\ 0 & 1 & 0 \\ -\sin(\beta) & 0 & \cos(\beta) \end{bmatrix} \times \begin{bmatrix} \cos(\gamma) & -\sin(\gamma) & 0 \\ \sin(\gamma) & \cos(\gamma) & 0 \\ 0 & 0 & 1 \end{bmatrix}. \tag{5.13}$$

The parameters for the $EuCl_3 \cdot 6H_2O$ spin Hamiltonian were fitted in [44] for both the ^{151}Eu and ^{153}Eu isotopes, they are reproduced in Table 5.2 and Table 5.3.

Table 5.2: Ground-state $^7F_0$ spin Hamiltonian parameters for $EuCl_3 \cdot 6H_2O$.

	Ground-State $^7F_0$	
Fitted parameters	$^{151}Eu^{3+}$	$^{153}Eu^{3+}$
$\alpha(^\circ)$	0.0 ± 0.8	0.0 ± 0.8
$\beta(^\circ)$	6.2 ± 1.4	6.2 ± 1.4
$\gamma_M(^\circ)$	67.31 ± 0.07	67.31 ± 0.07
$\gamma_Q(^\circ)$	87.07 ± 0.13	87.07 ± 0.13
g_x (MHz/T)	$\mp 1.504 \pm 0.004$	$\mp 0.673 \pm 0.002$
g_y (MHz/T)	$\pm 4.029 \pm 0.004$	$\pm 1.794 \pm 0.002$
g_z (MHz/T)	3.006 ± 0.008	1.35970 ± 0.04
E (MHz)	-5.29026 ± 0.00002	13.66093270 ± 0.00008
D (MHz)	0.35692 ± 0.00003	0.79181570 ± 000014
Z_x (MHz/T^2)	134.5 ∓ 0.5	134.5 ∓ 0.5
Z_y (MHz/T^2)	-50.66 ± 0.2	-50.66 ± 0.2
Z_z (MHz/T^2)	-57.87 ± 0.2	-57.87 ± 0.2

Table 5.3: Excited-state $^5D_0$ spin Hamiltonian parameters for $EuCl_3{\cdot}6H_2O$.

	Excited-State $^5D_0$	
Fitted parameters	$^{151}Eu^{3+}$	$^{153}Eu^{3+}$
$\alpha(\circ)$	0.0 ± 0.8	0.0 ± 0.8
$\beta(\circ)$	6.2 ± 1.4	6.2 ± 1.4
$\gamma_M(\circ)$	-3.1 ± 0.7	-3.1 ± 0.7
$\gamma_Q(\circ)$	-13.22 ± 0.03	-13.22 ± 0.03
g_x (MHz/T)	9.666 ± 0.006	4.269 ± 0.003
g_y (MHz/T)	9.293 ± 0.006	4.105 ± 0.003
g_z (MHz/T)	10.025 ± 0.014	4.428 ± 0.007
E (MHz)	9.0859570 ± 00003	23.21 ± 0.02
D (MHz)	-1.8586870 ± 00005	-4.8 ± 0.02
Z_x (MHz/T^2)	0	0
Z_y (MHz/T^2)	0	0
Z_z (MHz/T^2)	0	0

Through the calculation of eigenvalues of this reduced spin Hamiltonian, the hyperfine splittings of the ground and optical excited-state multiplets can be calculated. The relative oscillator strengths of optical transitions are calculated from the state overlap of the ground and excited-state wavefunctions, for example:

$$R = \frac{\left\| \langle \psi_{1g} | \psi_{1e} \rangle \right\|^2}{\left\| \langle \psi_{2g} | \psi_{2e} \rangle \right\|^2}. \tag{5.14}$$

The $EuCl_3{\cdot}6H_2O$ spin Hamiltonian describes a 14-dimensional space with 336 possible Λ systems. This parameter space is too large to perform an analytical analysis of field values which give desirable Λ systems. In order to obtain a complete picture of magnetic field values that yield favourable system parameters, numerical simulations were performed. Analysis of field values that give favourable oscillator strength ratios was performed for a specific choice of computing levels in [110].

In an ideal system, the excited level only has strong transitions to the computing states and the computing transitions have equal oscillator strengths. In addition, there need to be a large splitting between the computing levels, excluding many field regions where the oscillator strengths are otherwise favourable.

A simulated annealing algorithm was used to minimise QGE starting from a grid of initial magnetic field points. The system simulated was a 500 ion ensemble with a 50 kHz tophat lineshape. The QGE model is computationally expensive due to the number of possible field values and Λ systems, so error minimisation was performed using a two-step optimisation routine:

- At a given field value, "promising" Λ systems with relative oscillator strengths greater than 0.25 and separations from other transitions greater than 30 MHz were identified.

- A NOT gate was then simulated for each of these Λ systems and the lowest QGE for any of these systems was taken as the error at that field value.

The minimum error at each field value was calculated using a rudimentary optimisation of the Rabi frequency for the relevant Λ system. The Rabi frequency was optimised using the following procedure:

- Calculate the error value for two possible values of the Rabi frequency, Ω_0 and Ω_1.
- The secant method was then used to select the value Ω_n to evaluate the error for, $\Omega_n = \Omega_{n-1} - E(\Omega_{n-1})\frac{\Omega_{n-1}-\Omega_{n-2}}{E(\Omega_{n-1})-E(\Omega_{n-2})}$.
- Ten evaluations of the error function were then performed.
- If the minimum error value was below 0.1, a further ten evaluations of the Rabi frequency were performed.
- If after the additional ten function evaluations the error was below 0.05, a further ten evaluations of the Rabi frequency were performed.

A ball of error values was calculated by performing simulated annealing at each point on a spherical grid of points about zero-field. Figure 5.3 displays the QGE on this ball of field values. When the initial grid point had no Λ system with oscillator strength > 0.05 or splitting > 10 MHz, only the error value at the initial field point was calculated. Simulating the QGE at such points is very computationally expensive and hence we sought to evaluate the error at as few of these points as possible.

Regions with low error correspond to regions where the $|0\rangle$ and $|1\rangle$ states are well-mixed (far from the m_z eigenstates), and the spectral resolution of the optical transitions is high. For ^{151}Eu, there are ≈ 5 regions where the error is below 0.1 between 1 and 10 T. The error tends to be lower at higher fields, as the spectral resolution of the transitions improves with increasing field. Below 10 T, the lowest error obtained for a 50 kHz ensemble was 0.022 at point $(1.4975, -6.7127, 3.9684)$T, with a magnitude of 7.67T. At lower fields, large regions where the error is fairly low (< 0.05) exist, spanning more than 0.2 Tesla in every direction. The lowest error obtainable below 2T is 0.065 at $(-1.6097, -0.4587, -0.3916)$T. The error of a disk containing the
$(1.4975, -6.7127, 3.9684)$T point and perpendicular to the C_2 axis is shown in Figure 5.5.

^{153}Eu has smaller Zeeman coefficients than ^{151}Eu and so larger fields are required to obtain well-mixed states that give good oscillator strength ratios. Due to the poor mixing, no low error points exist below 1.5T and for field values below $\approx$ 15T, ^{153}Eu has a higher error than ^{151}Eu. For fields greater than $\approx$ 15T, ^{153}Eu gives lower error values than ^{151}Eu due to its larger hyperfine splittings.

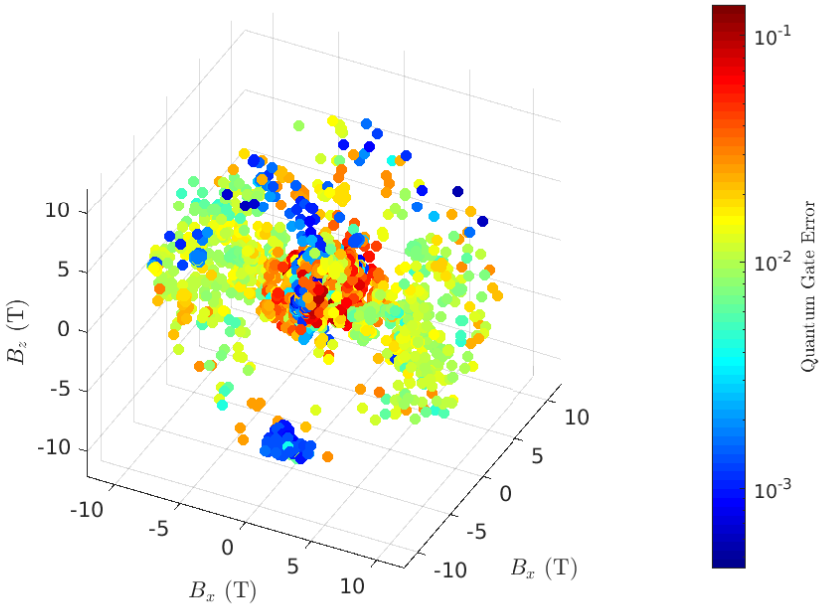

Figure 5.3: QGE for fields with a magnitude below 8T with ^{151}Eu.

5.4 ZEFOZ

The primary objective of this chapter is to illustrate the use of magnetic fields to reduce QGE. Applied magnetic fields can also be used to increase hyperfine coherence times by applying a zero first-order Zeeman (ZEFOZ) magnetic field, where a particular transition of the rare-earth ion is insensitive to magnetic fluctuations to first-order [29]. It would be desirable to be able to apply fields that are both ZEFOZ points and have a low QGE.

ZEFOZ points for a transition occur when the gradient $\mathbf{S_1}$ of the transition frequency f with respect to magnetic field $\mathbf{B}$ vanishes, namely that:

$$\mathbf{S_1} = \left(\frac{\partial f}{\partial B_x}\right)^2 + \left(\frac{\partial f}{\partial B_y}\right)^2 + \left(\frac{\partial f}{\partial B_z}\right)^2 = 0. \tag{5.15}$$

Through the use of Equation 5.9, the ZEFOZ points of $EuCl_3{\cdot}6H_2O$ can be calculated. To determine if any hyperfine ZEFOZ points coincided with regions of low error, the hyperfine ZEFOZ points below 20 T were first calculated. Simulations of QGE were then performed with the $^7F_0$ ZEFOZ levels as the system $|0\rangle$ and $|1\rangle$ levels and choices of excited-state such that the Λ system met the earlier criteria for a promising point. From these simulations, I determined that there were several ZEFOZ points coinciding with regions of low error. Figure 5.6 displays the hyperfine ZEFOZ points of $EuCl_3{\cdot}6H_2O$ with the field values existing in low error regions circled.

The identified field values correspond to ZEFOZ transitions between different

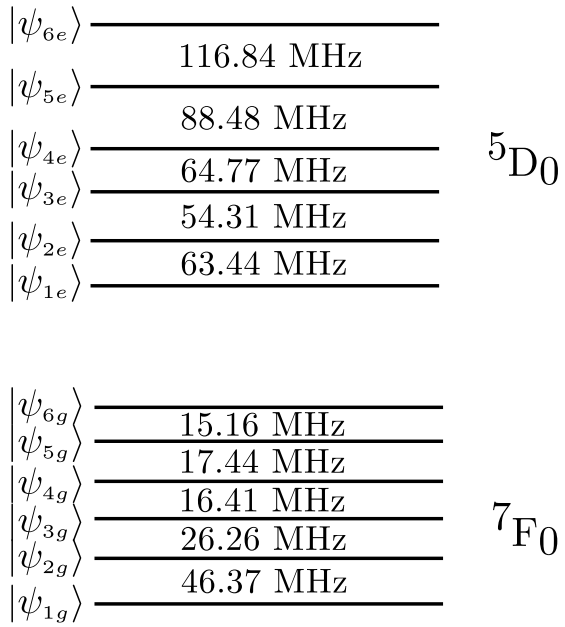

Figure 5.4: Hyperfine structure at field point $(1.4975, -6.7127, 3.9684)$T. At this field value the Λ system with the $|\psi_{1g}\rangle$ and $|\psi_{2g}\rangle$ as the ground-state computing levels and $|\psi_{1e}\rangle$ as the optical excited level gives a QGE of 0.065.

ground-state hyperfine levels. The level structure of the *A* and *B* ZEFOZ points from Figure 5.6 are displayed in Figure 5.7 with the ZEFOZ computing levels and the auxiliary optical level labelled.

At the *A* point, there is a ZEFOZ transition between the $|\psi_{1g}\rangle$ and $|\psi_{2g}\rangle$ levels; with the $|\psi_{6e}\rangle$ level used as the auxiliary optical state this system has a QGE of 0.0371 for the three-qubit bit-flip sequence. At the *B* point the $|\psi_{2g}\rangle$ and $|\psi_{5g}\rangle$ levels have a ZEFOZ transition; using the $|\psi_{4e}\rangle$ level as the auxiliary optical state gives a QGE of 0.0416.

The field values at the *A* and *B* points are $(0.2742, 8.7432, -0.0298)$ and $(1.0033, -2.3311, -0.109)$ respectively. Figure 5.8 displays the error in a sphere about these ZEFOZ points.

5.5 Other rare-earths

Although the use of specific magnetic fields can be used to improve the properties of the example $EuCl_3{\cdot}6D_2O$ system, there is a limit to how much this system can be improved through this or any other technique. The $EuCl_3{\cdot}6D_2O$ system is fundamentally limited by the size of the hyperfine splittings in the $^7F_0$ and $^5D_0$ levels, relative to the optical coherence time of this system. The limitations of $EuCl_3{\cdot}6D_2O$ for performing quantum operations are discussed further in Chapter 6. This is not an issue unique to $EuCl_3{\cdot}6H_2O$ but to europium systems as a whole. The suitability of other europium crystal systems is unlikely to be substantially different from $EuCl_3{\cdot}6H_2O$,

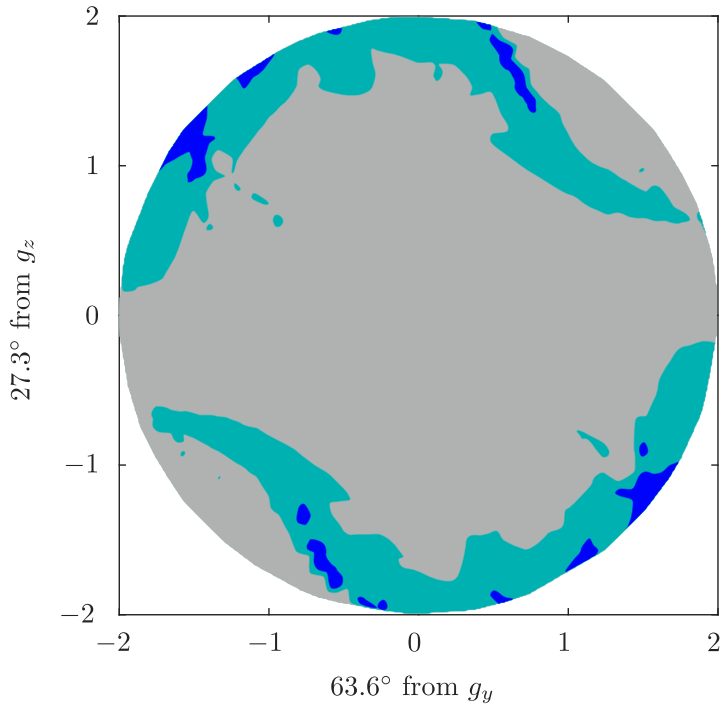

Figure 5.5: QGE in a 2T disk, offset by $(0.5, 0, 0)$ T. Regions with error below 5% are dark blue, between 5% and 10% teal, and above 10% grey.

with the hyperfine splittings [116, 117] and optical coherence times [118] similar in previously studied systems. Europium is not unique amongst the rare-earth ions in being limited by the hyperfine splitting to optical coherence time ratio,

Although europium is limited by its hyperfine splitting to optical coherence time ratio, it still compares favourably to some of the other rare-earth ions in this regard. In particular, praseodymium systems are likely to have significantly higher QGE due to their $\mathcal{O}(100\mu\text{s})$ optical coherence times and $O(10\text{MHz})$ hyperfine splittings [119].

In light of this inherent limitation of europium satellite systems, it is worth exploring if lower QGE can be achieved with other rare-earth hosts. In addition to a favourable ratio of hyperfine splittings to optical coherence time, there are several other properties necessary for any candidate system to be suitable for quantum computing. For the purposes of qubit initialisation and manipulation, a low optical inhomogeneous linewidth and long hyperfine coherence times are also requirements. Additionally, for addressing and reading out qubits to be feasible, the quantum efficiency and optical oscillator strengths must be sufficiently large. Two potential rare-earth species that may merit exploration in future work are the Kramers ion erbium and the non-Kramers ion holmium. These ions both have large magnetic moments and resultantly large hyperfine splittings. Erbium and holmium are not an exhaustive list of rare-earth ions with potential for quantum computing and it is possible that other rare-earth ions, such as neodymium, are well-suited for low-error quantum gates.

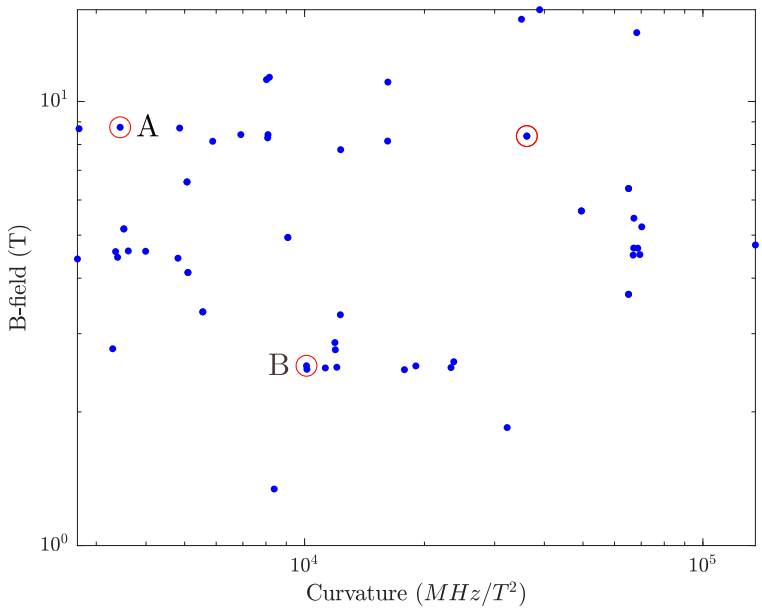

Figure 5.6: Hyperfine ZEFOZ points below 20T for $EuCl_3{\cdot}6H_2O$, with ZEFOZ points that coincide with regions of low error circled. The low error ZEFOZ point with the lowest curvature is labelled *A* and the low error ZEFOZ point at the lowest magnetic field magnitude is labelled *B*.

Of the Kramers ions, erbium is of particular interest due to its narrow optical inhomogeneous linewidths, with one of the narrowest measured optical inhomogeneous lines 16 MHz in ^{170}Er:$^7LiYF_4$ [120]. An additional consideration for the use of erbium satellite systems is the compatibility with existing telecom wavelength technologies. Erbium has hyperfine splittings of $\mathcal{O}$(GHz) [121] and optical oscillator strengths of $\mathcal{O}(1 \times 10^{-6})$ [122]. In doped Er:YSO systems, optical coherence times of 4.4 ms [123] and hyperfine coherence of 1.3 s [121] times have been achieved by applying magnetic fields up to 7 T and cooling the sample to sub 1.5 K. In doped crystals the properties of erbium make it well-positioned for performing low error gates, however in order to create a satellite system it is necessary to move to a stoichiometric crystal. Although there is little existing literature on stoichiometric erbium systems, it is known that Er:LiF_4 has well-resolved satellite lines and measured optical lifetimes of $\mathcal{O}$(ms) [124].

Holmium is a non-Kramers ion with very large hyperfine splittings due to its large magnetic moment. The hyperfine splittings of holmium are commonly of $\mathcal{O}$(GHz) [125–129], which is $\approx$ 100 times larger than the splittings found in $EuCl_3{\cdot}6H_2O$. Holmium has optical coherence times of $\mathcal{O}(\mu s)$[130] and hyperfine coherence times of $\mathcal{O}$(ms) [131] in doped materials. The optical oscillator strengths are $\mathcal{O}(10^{-6})$ [132], which is $\approx$ 100 greater than those of europium systems and there is good mixing between hyperfine levels. In order to use holmium as a computing species for a rare-earth satellite system, it will be necessary to extend the coherence times past

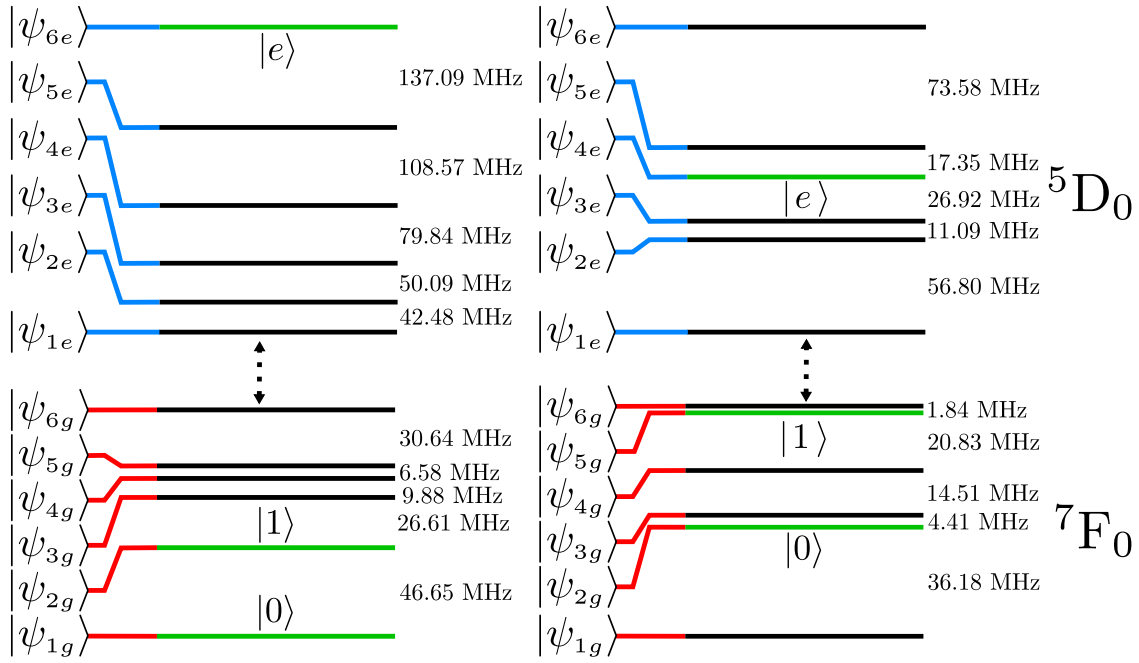

Figure 5.7: Level structure of the *A* and *B* ZEFOZ points with the computing levels and auxiliary optical level labelled. The *A* point has a ZEFOZ transition between the $|\psi_{1g}\rangle$ and $|\psi_{2g}\rangle$ $^7F_0$ levels and the *B* point has a ZEFOZ transition between the $|\psi_{2g}\rangle$ and $|\psi_{5g}\rangle$ $^7F_0$ levels.

was has been reported in the literature. It is possible that techniques similar to those used in erbium [121, 123] could give substantial increases in the coherence times of holmium materials.

The hyperfine splittings of both erbium and holmium ions are $\mathcal{O}(\text{GHz})$, which is ≈ 100 times larger than those in europium materials. Correspondingly, there is potential for up to a 100-fold decrease in QGE moving to such rare-earth materials.

There are two major open questions that must be addressed regarding computing in rare-earth satellite materials. The first question is whether rare-earth species other than europium have suitable coherence properties in stoichiometric materials. To date, the only measured optical or hyperfine spin coherence times in stoichiometric systems have been in $EuCl_3{\cdot}6H_2O$. Further investigation is needed to determine the coherence properties of other rare-earth ions in stoichiometric crystals.

The second question is whether dephasing due to magnetic coupling with the surrounding spin-bath can be reduced. In both erbium and holmium materials, there is a large magnetic moment. In erbium, this is due to the electron spin state, whereas in holmium it is due to the nuclear spin state. As a result of this magnetic moment, there is a large magnetic coupling between these ions and the surrounding spin bath [133]. In erbium materials, this coupling causes rapid flipping of the electron spins, leading to very short transition lifetimes and coherence times. In [121] a 7 T field was used to polarise the erbium spins, creating a 'frozen core' about each erbium ion —

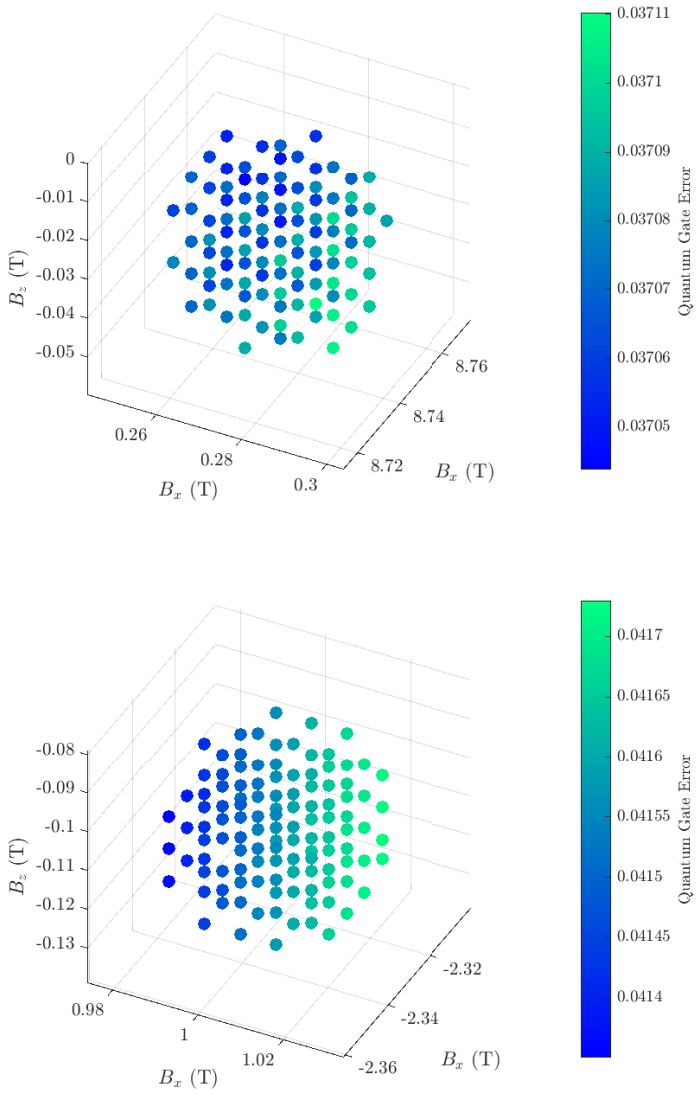

Figure 5.8: QGE in a ball of radius 0.025 T about the *A* and *B* ZEFOZ points. There are large regions in which it is possible to be both in the vicinity of a hyperfine ZEFOZ point and to have low QGE when these transitions are used in a quantum computing system. Within 0.025 T from the *A* ZEFOZ point, the QGE is below 0.0371 and within 0.025 T of the *B* ZEFOZ point, the QGE is below 0.0420.

with the electron spins frozen, the nuclear spins could then be used as a quantum resource. In stoichiometric materials, a large magnetic field can not be used to create a frozen core, as each ion in the stoichiometric bulk is identical. It may be possible to create a frozen core in stoichiometric materials by using a dopant with a small magnetic moment. The difference in the magnetic moment between the dopant and stoichiometric ion will create a large magnetic field gradient, which may be sufficient to create a frozen core.

5.6 Summary

This chapter discussed the application of magnetic fields to manipulate the properties of rare-earth satellite systems in order to reduce the QGE. Applied magnetic fields can be used to increase the hyperfine spacing between levels and bring the relative oscillator strengths closer to a Λ system in order to reduce QGE.

Regions of low QGE were identified using a simulated annealing algorithm and it was found that there are several regions in which a QGE of less than 5% for a seventeen pulse bit-flip correction sequence can be achieved. The low error regions are wide, with some of these regions forming balls of radius greater than 0.1T. For field values less than 15T, $^{151}Eu^{3+}$ gives lower error values than $^{153}Eu^{3+}$ due to the larger Zeeman coefficients with the increased hyperfine splittings of $^{153}Eu^{3+}$ not yielding lower error rates until the applied field is greater than 15T.

The error in regions surrounding hyperfine ZEFOZ points was simulated and it was found that there are several ZEFOZ points that exist in low error regions. The QGE at the low error ZEFOZ point with the smallest field magnitude was calculated to be 0.0355 and the QGE at the low error ZEFOZ point with the smallest curvature was calculated to be 0.0262.

To conclude the chapter, the potential for the use of other rare-earth species was discussed. The QGE in europium systems is fundamentally limited by the size of the europium hyperfine splitting relative to the optical coherence time. The potential for computing in erbium and holmium was explored due to their larger hyperfine structure and it was established that there is potential for up to a 100-fold reduction in gate-error by moving to these host ions. Stoichiometric erbium and holmium systems have yet to be investigated and much further research is needed to determine if satellite quantum computing can be performed using these rare-earth ions.

The results in this chapter inform the regimes in which it is feasible to perform quantum operations using a stoichiometric $EuCl_3{\cdot}6D_2O$ system. The high error rate when performing gate operations at zero-field necessitates the use of an applied field when implementing computing in this system. Low error operation can be achieved through the use of an 8T magnetic field to favourably manipulate the oscillator strengths. If the maximum magnetic field that can be applied is less than $\approx$ 12T then the $^{151}Eu^{3+}$ transitions are preferable for quantum operations due to their lower error in this regime.

Chapter 6

Pulse optimisation

This chapter explores the optimisation of the optical pulses used to perform gates in rare-earth crystal systems. There are three inhibiting factors that need to be considered when performing pulses on a rare-earth ensemble system: off-resonant excitation to neighbouring hyperfine levels, decoherence over the course of the pulse and inhomogeneous driving of the ensemble. Minimising the error in performing a pulse requires optimisation of both the Rabi frequencies and frequency profile so as to minimise the sum of these error sources.

The chapter begins with a comparison of the performance of pulse shapes commonly seen in the literature and an evaluation of their relative performance at both zero-field and the low error regions identified in Chapter 5. This is followed by an investigation into the use of arbitrary pulse shapes and the regimes in which different forms of pulses are optimal. The chapter concludes with a discussion of how quantum gates can be modified to reduce the number of constituent optical pulses and make use of favourable properties of rare-earth crystal systems.

6.1 Standard pulse types

In the quantum computing literature, there are standard pulse types that are commonly used to drive quantum systems. The most common pulse shapes seen are square, Gaussian and hyperbolic secant (Sech). These pulse shapes have unique characteristics that make them advantageous in different situations. Square pulses are the narrowest pulses in the time domain; however, they have a broad frequency distribution in the form of a *sinc* function. Gaussian pulses are longer in the time domain than square pulses, which is counterbalanced by their narrower frequency distribution. Sech pulses take slightly longer to perform than Gaussian pulses, with a correspondingly narrower frequency distribution. Sech pulses are of additional interest because they provide exact solutions to the optical Bloch equations and do not experience pulse deformation as they pass through an optically thick medium [134]. These standard pulse shapes are displayed in Figure 6.1.

In order to determine how to optimally drive the $EuCl_3{\cdot}6D_2O$ system using the standard pulse shapes, simulations of a NOT gate were performed at both zero-field and the 8T field value identified in Chapter 5. The simulations modelled the effect on

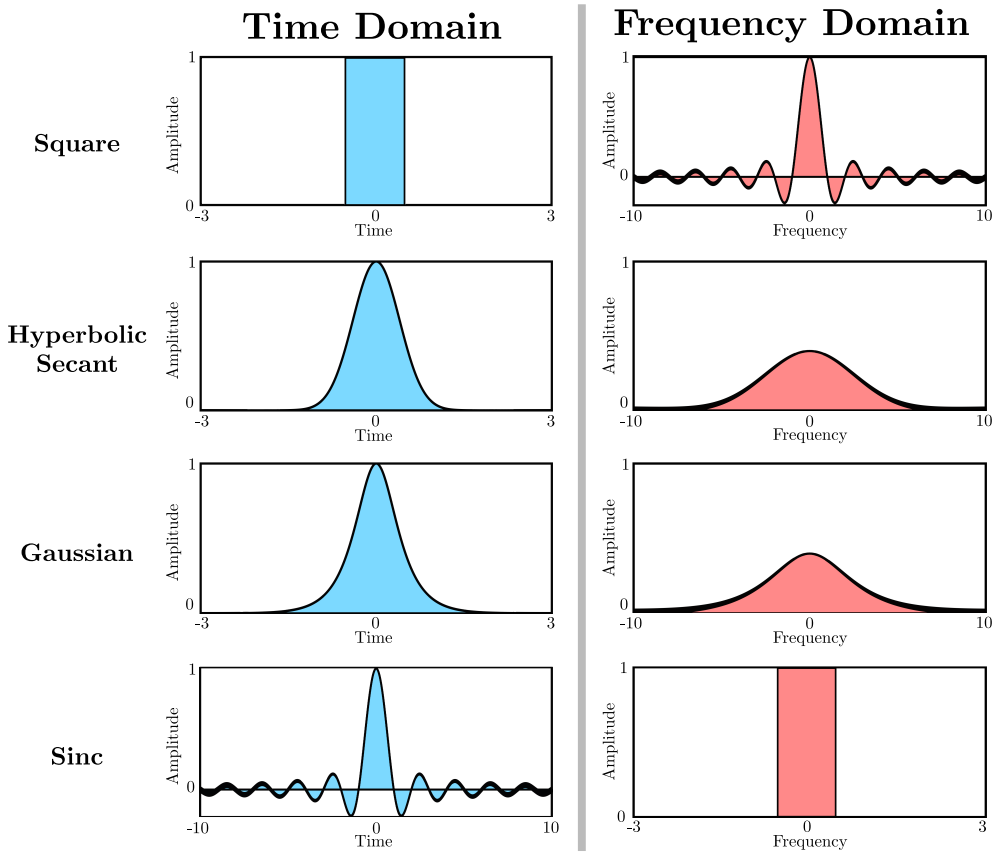

Figure 6.1: Standard pulse shapes commonly used to drive quantum systems.

an inhomogeneously broadened ensemble of 500 ions using an optical Bloch equation model of the full 12 level system with Lindbladian operators to model decoherence. 500 was chosen as the size of the ion ensemble as a compromise between capturing the frequency inhomogeneity of the ensemble and simulations completing in a feasible length of time. Table 6.1 displays these optimised values. To decrease optimisation time, each pulse in the NOT gate sequence was assumed to have an area of π. The Sech pulses were parametrised by:

$$\Omega_{Sech}(t) = \Omega_{peak}[\text{sech}(\Omega_{peak}t)]^{(1+i\mu)}, \tag{6.1}$$

the square pulses by:

$$\Omega_{Square}(t) = \Omega_{peak}\Pi(\frac{t}{\Omega_{peak}\pi}), \tag{6.2}$$

where $\Pi(t)$ is the rectangular function and the Gaussian pulses by:

$$\Omega_{Gaussian}(t) = \Omega_{peak}\exp\left(-\frac{(\Omega_{peak}t)^2}{\pi}\right). \tag{6.3}$$

Table 6.1: Optimised parameters and corresponding error values for standard pulse shapes at both zero-field point and the 8T point identified in Chapter 5. The 0 and 1 subscripts denote the optimised parameter for a pulse driving the $|0\rangle \leftrightarrow |e\rangle$ and $|1\rangle \leftrightarrow |e\rangle$ transitions respectively. The Rabi frequencies in this table are given relative to a resonant transition with a unit relative oscillator strength, the transition specific Rabi frequency can be found by multiplying this value by the relative oscillator strength of the transition.

Field Point	Sech	Gaussian	Square
Zero-Field	$E = 0.59$ $\Omega_{0,peak} = 16.43$ MHz $\Omega_{1,peak} = 149.9$ MHz $\mu_0 = 0.1465$ $\mu_1 = 0.04390$	$E = 0.58$ $\Omega_{0,peak} = 14.74$ MHz $\Omega_{1,peak} = 149.9$ MHz	$E = 0.66$ $\Omega_{0,peak} = 11.20$ MHz $\Omega_{1,peak} = 112.5$ MHz
8T point	$E = 0.0039$ $\Omega_{0,peak} = 57.03$ MHz $\Omega_{1,peak} = 34.83$ MHz $\mu_0 = 0.0014$ $\mu_1 = 0.000$	$E = 0.0037$ $\Omega_{0,peak} = 55.96$ MHz $\Omega_{1,peak} = 29.42$ MHz	$E = 0.0060$ $\Omega_{0,peak} = 25.57$ MHz $\Omega_{1,peak} = 22.07$ MHz

At zero-field, the error of all of the standard pulses is much too high to be useful as a computing system, as previously determined in Section 5.2. At the 8T point, Gaussian pulses outperform both Square and Sech pulses, with a 38% and 5% lower error, respectively.

6.2 Pulses in an ensemble

In addition to the effects of off-resonant excitation and decoherence, pulses in an ensemble are limited by their ability to address the entire ensemble when it is inhomogeneously broadened. To reduce the effect of off-resonant driving in an inhomogeneously broadened ensemble *composite pulses* can be used. In place of a single pulse to rotate the state of an ensemble, composite pulses use multiple pulses applied at different angles to drive the ensemble state. For ensembles with a frequency distribution, composite pulse schemes can be used to drive the ensemble to a more consistent state than direct pulses. There are several composite pulse schemes in the NMR literature that have demonstrated this increased tolerance of ensemble frequency detuning [135]. Figure 6.2 shows the action of a $90^\circ_{90^\circ} 180^\circ_{0^\circ} 90^\circ_{90^\circ}$ pulse sequence (Where the angles denote the pulse area and the subscript angle denotes the phase relative to the $\hat{x}$ axis) on an ensemble, displayed on the Bloch Sphere.

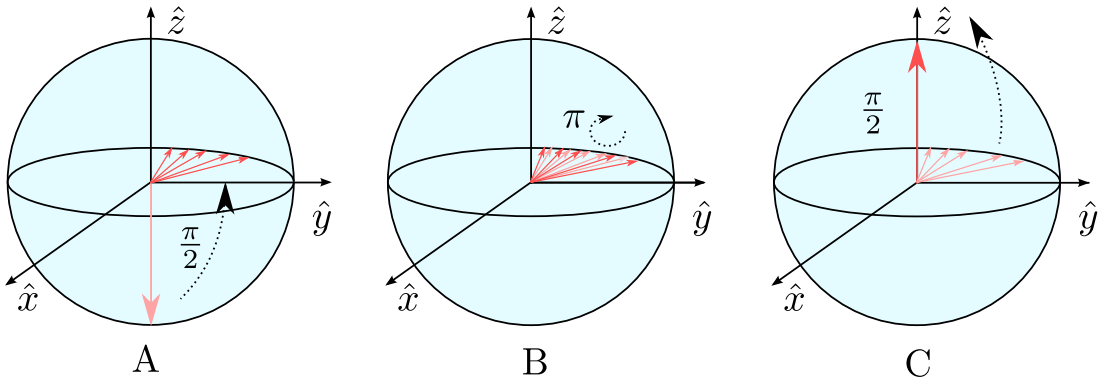

Figure 6.2: Action of a $90^{\circ}_{90^{\circ}} 180^{\circ}_{0^{\circ}} 90^{\circ}_{90^{\circ}}$ composite pulse on the Bloch sphere, performing a π rotation about the $\hat{x}$ axis. During the 90° rotation in A, the ions in the ensemble dephase due to the inhomogeneous broadening. The 180° rotation in B reverses the direction of this dephasing, causing the ions to rephase. In C, a second 90° rotation is applied to the ensemble; during this pulse, the ions are still rephasing with this pulse timed such that the ions finish rephasing when the pulse completes. Using this multi-axis pulse allows for the inhomogeneously broadened ensemble to be driven more uniformly than a direct rotation.

Implementing composite pulses in a rare-earth system is complicated by the need to not excite levels neighbouring the computing levels. Composite pulse sequences for an arbitrary initial state use square pulses, some of which are narrow in time. Narrow square pulses create a large amount of off-resonant excitation to both neighbouring hyperfine levels and ions outside of the hole-burnt features, making them unsuitable for ensemble rare-earth systems. A method for the use of composite pulse sequences more suitable for rare-earth systems was proposed by Roos and Mølmer in 2004 [136]. In this scheme, both of the ground optical state to excited optical state computing transitions are driven simultaneously. The pulse scheme begins with choosing the relative phase ϕ of the driving fields are chosen such that there is an orthonormal basis:

$$|\bar{0}\rangle = \frac{1}{\sqrt{2}}(|0\rangle - e^{-i\phi}|1\rangle) \tag{6.4}$$

$$|\bar{1}\rangle = \frac{1}{\sqrt{2}}(|0\rangle + e^{-i\phi}|1\rangle), \tag{6.5}$$

in this basis $|\bar{1}\rangle$ is driven to the $|e\rangle$ excited-state and $|\bar{0}\rangle$ is a *dark-state* which is unaffected by the driving fields. Applying a second pulse where both driving fields have a phase shift of $\pi + \theta$ drives the $|e\rangle$ state to $e^{i\theta}|\bar{1}\rangle$. This dark state scheme transforms a pulse sequence that provides a compensated rotation between the poles of the Bloch sphere into a sequence that can provide an arbitrary rotation. The paper demonstrated that a multi-pulse Gaussian sequence could be used to achieve a more accurate gate operation on a 1 MHz ensemble than is possible with either a

compensated $90^{\circ}_{90^{\circ}}180^{\circ}_{0^{\circ}}90^{\circ}_{90^{\circ}}$ sequence of square pulses or direct rotations.

To investigate whether using this dark-state scheme instead of direct pulses is advantageous in this system, simulations of a NOT gate were performed at the 8T field point, using the dark-state scheme with six dual-frequency Gaussian pulses and direct NOT gates with three Gaussian pulses or three Sech pulses. These simulations were performed using an inhomogeneously broadened ensemble of 500 ions, with all 12 hyperfine levels and decoherence included in the model. It was assumed that the applied pulses did not have any errors in amplitude or phase. In the 2004 Roos and Mølmer paper, it was found an exact $90^{\circ}_{90^{\circ}}180^{\circ}_{0^{\circ}}90^{\circ}_{90^{\circ}}$ sequence did not give the lowest error. To minimise QGE, the phase, area and Rabi frequency of the pulses in both the compensated and direct sequences were optimised. The simulations were repeated at different qubit linewidths to investigate the relationship between qubit linewidth and QGE for the compensated and direct pulse schemes. Figure 6.3 displays the error of the compensated sequence compared to the error of a NOT gates implemented with direct rotations using Gaussian or Sech pulses.

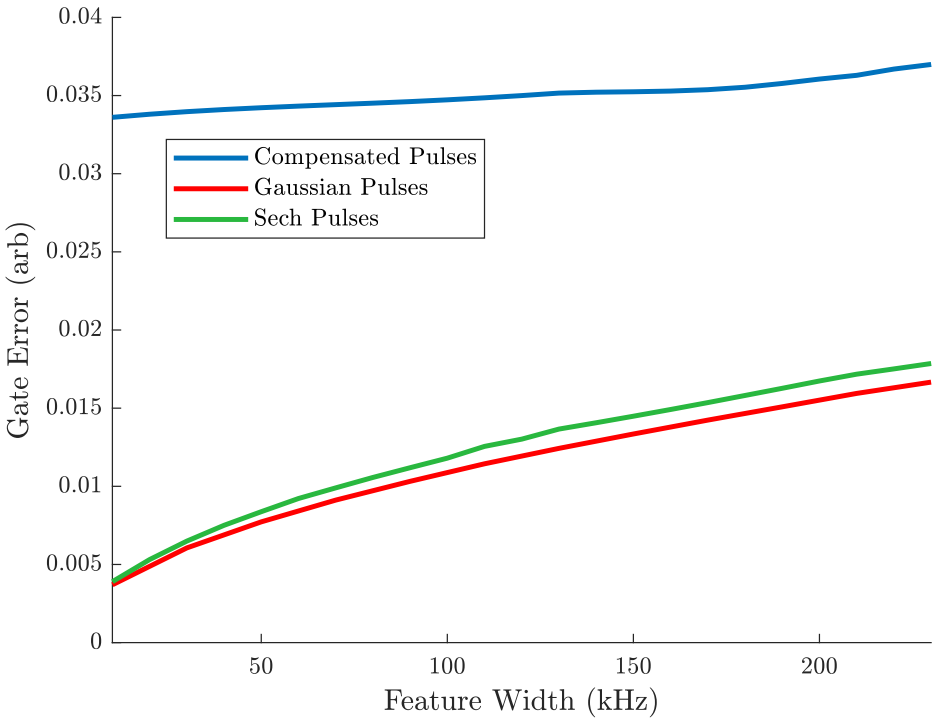

Figure 6.3: QGE as a function of linewidth for implementation of a NOT gate with direct Gaussian or Sech pulses and error compensated pulses.

For the ensemble linewidths considered, both direct Gaussian and Sech pulses substantially outperform the compensated pulses, with Gaussian pulses having a marginally lower QGE than Sech pulses and the QGE of the compensated sequences ≈ 3 times larger than both direct pulse types. The compensated pulses appear to scale slower with an increase in linewidth compared to the direct pulses; however, this is insufficient to yield a lower error even with a feature width of 250 kHz. The Gaussian

and Sech sequences outperforms the compensated sequence due to the shorter amount of time spent in the optical excited-state, which results in less decoherence and fewer pulses applied to the ensemble, thereby resulting in less off-resonant excitation.

For a compensated pulse sequence to have a lower QGE than direct rotations, the dominant source of error would need to be the inhomogeneous broadening of the qubit feature, as opposed to optical decoherence and off-resonant excitation of hyperfine levels. In a $EuCl_3 \cdot 6D_2O$ system, the qubit widths would have to be $\mathcal{O}$(MHz) to be in this regime; this would result in very high QGE and is not a relevant regime for quantum computing in this system. In systems with broader optical inhomogeneous linewidth, the use of compensated pulses may lead to a lower error than direct pulses. In such a system, where it is necessary to use $\mathcal{O}$(MHz) width computing features, off-resonant driving of the ensemble would be the primary source of error.

6.3 Arbitrary pulse shapes

In addition to the standard pulse shapes seen in the literature, customised pulse shapes can be used to account for the properties of the specific computing system. The optimal pulse shape depends on the states which need to be driven and the relative effect of off-resonant excitation and decoherence on the QGE. Population transfer with no off-resonant excitation can be accomplished using adiabatic pulses; however, these are very slow and lead to a large amount of decoherence. Shortcut to adiabaticity (STA) pulses are a method for achieving the same net effect as an adiabatic pulse in a much shorter time window. STA pulses have been shown to allow for even driving of a 1 MHz wide rare-earth ensemble [35]. Although STA pulses are able to achieve very low error rates, they are unsuitable for implementing quantum gates as they only have this behaviour for rotations beginning from known states, for example, during qubit initialisation. Outside of the adiabatic regime, there is a large potential solution space for optimal pulses. For example, in the limit of widely spaced levels with a short coherence time, direct square pulses may be optimal, whereas for very closely spaced levels, simultaneous driving of multiple transitions may yield the best performance.

As the landscape of potential pulse solutions is so large, it is unlikely that an optimal gate sequence will be found through analytical methods. To minimise QGE, an arbitrary pulse sequence can instead be used, with the amplitude and phase at evenly spaced points in a time window being optimised to reduce QGE. Optimising a pulse sequence in such a manner allows for pulses to take an arbitrary shape and to drive multiple transitions.

In order to estimate the level of improvement that can be obtained through the use of an arbitrary pulse sequence, a NOT gate was optimised at the 8T point using the Krotov method [137]. The Krotov method is a non-local gradient optimisation method with monotonic convergence to an optimal sequence. This optimisation method was presented instead of other methods such as Gradient Ascent Pulse Engineering (GRAPE) as it converged to an optimal solution with fewer iterations.

The operation of a NOT gate was optimised in a 20μs window, discretised into 6000 time segments. The optimisation was performed in the interaction picture, with the $|0\rangle \leftrightarrow |e\rangle$ transition used as the oscillation frequency. The initial conditions for the driving field were defined by a random driving field of maximum amplitude 10 MHz (Relative to a transition with unit relative oscillator strength), given by a spline interpolation on 20 random Rabi frequency values. This starting condition was chosen to avoid erroneous solutions discussed later in this section. Over the course of the optimisation, the step-size for the change in the driving field was automatically reduced to ensure monotonic convergence to an optimal solution.

Two cases were considered, a maximum Rabi frequency of 10 MHz and an arbitrarily large Rabi frequency. Due to a slow convergence rate, pulses were optimised in a three-step process. Initially, pulses were optimised in a single-instance system, which gave the solution displayed in Figure 6.4 for the case limited to 10 MHz Rabi frequency and the solution in Figure 6.5 for the unconstrained case.

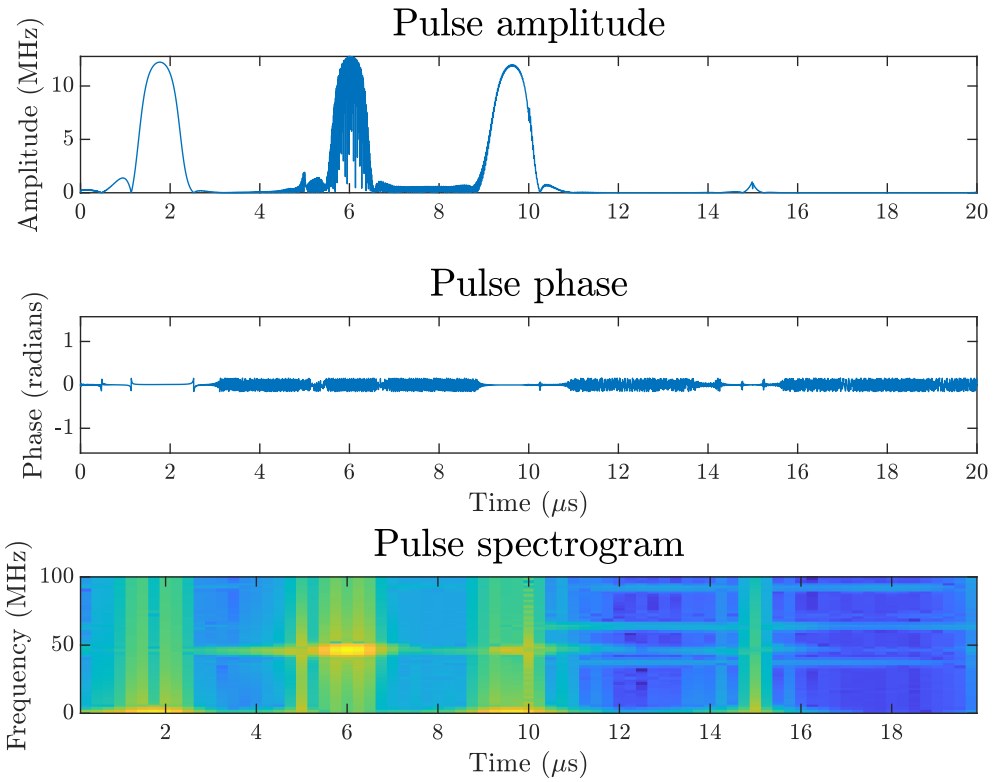

Figure 6.4: Optimised pulse solution for performing a NOT gate in a 20μs window with Rabi frequency constrained to 10 MHz. Simulation was performed in a single instance system at the 8T field value. The Rabi frequency displayed is relative to a transition with a unit relative oscillator strength.

In the single-instance case both the constrained and unconstrained optimised solutions have three distinct pulses, evenly spaced in time. The unconstrained case simultaneously drives the $|0\rangle \leftrightarrow |e\rangle$ and $|1\rangle \leftrightarrow |e\rangle$ transitions of the Λ system

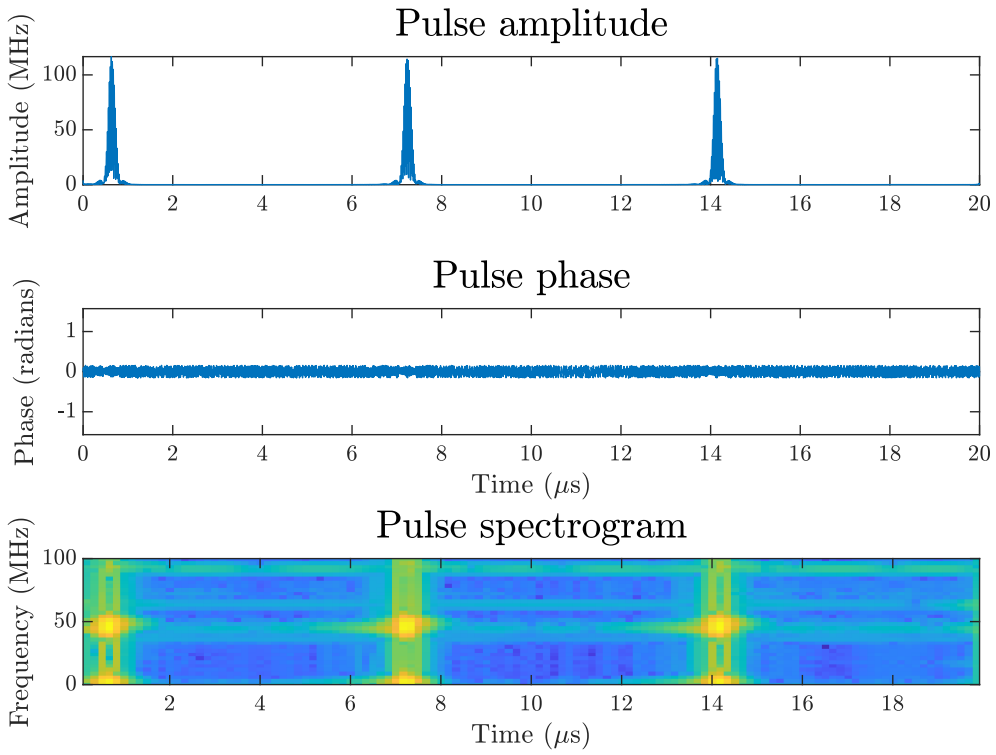

Figure 6.5: Optimised pulse solution with unconstrained Rabi frequency for performing a NOT gate in a 20μs window. Simulation was performed in a single instance system at the 8T field value. The Rabi frequency displayed is relative to a resonant transition with a unit relative oscillator strength.

identified in Section 5.3 with frequencies 46.37 MHz and 0 MHz. The constrained case alternates driving the $|0\rangle \leftrightarrow |e\rangle$ transition with frequency 46.37 MHz and the $|1\rangle \leftrightarrow |e\rangle$ transition with frequency 0 MHz, as in the pulse scheme proposed in Section 4.2.2.2.

This difference in pulse character between the constrained and unconstrained cases is due to the increased time that bicolour pulses take to implement. With the Rabi frequency constrained to 10 MHz, the additional error due to decoherence is larger than the decrease in off-resonant excitation for bicolour pulses. Due to this increased decoherence, pulses driving alternating computing frequencies give a lower error for the constrained case.

The frequencies present in the optimised single-instance solutions centre about the 0 MHz $|1\rangle \leftrightarrow |e\rangle$ and 46.37 MHz $|0\rangle \leftrightarrow |e\rangle$ transitions, with no peaks in Fourier transform power about other frequencies. The concentration of drive field power about the computing transitions and the lack of power about other transitions suggests that in this system, there is no benefit to driving transitions other than the computing transitions for the purposes of performing quantum gates.

Following this single-instance optimisation, an optimisation was performed with an ensemble of 500 ions with 100 kHz of optical inhomogeneous broadening using the single-instance solution as a starting value.

The Krotov method operates over a fixed number of time segments with constant duration. Due to this, if the chosen time window for the pulse is longer than is necessary to minimise gate error, the optimised solution will have blank time windows in which the qubits are not being acted on. These unused time windows increase the apparent gate error as they do not contribute to the operation of the gate and allow the qubits to decohere, hence they should be removed in the final pulse sequence. The pulse solutions obtained for single instance systems also had these unnecessary time windows; however, these windows were not removed until the ensemble optimisation to allow for a potential broadening of pulses in the time-domain. The optimised solutions with the unused time removed are displayed in Figure 6.6 for the 10 MHz maximum Rabi frequency case and Figure 6.7 for the unconstrained case.

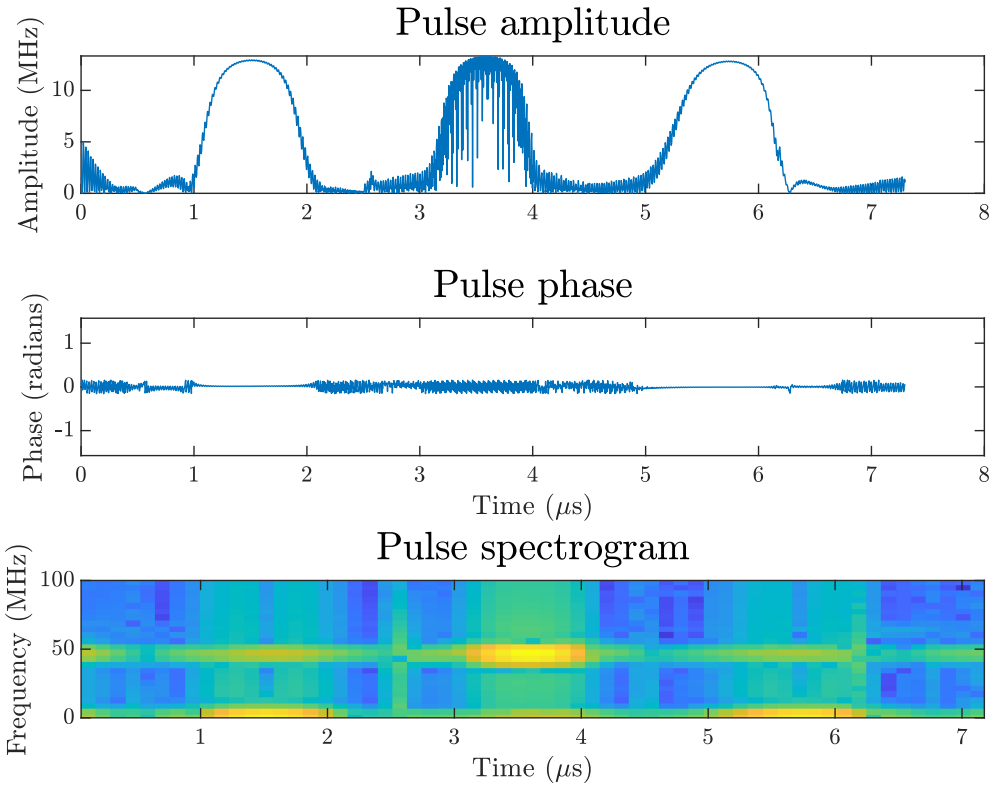

Figure 6.6: Optimised pulse solution for performing a NOT gate with Rabi frequency constrained to 10 MHz. Simulation was performed in a 100 kHz ensemble system at the 8T field value. This optimised sequence gave an error value of 0.00235. The Rabi frequency displayed is relative to a resonant transition with a unit relative oscillator strength.

The final optimised pulses in the ensemble system are very similar to those seen in the single-instance optimisation. As with the single-instance case, the pulses have a width between a hyperbolic secant and Gaussian pulse in both the time and frequency domains. These pulses also drive only the $|0\rangle \leftrightarrow |e\rangle$ and $|1\rangle \leftrightarrow |e\rangle$ computing transitions as in the single-instance case.

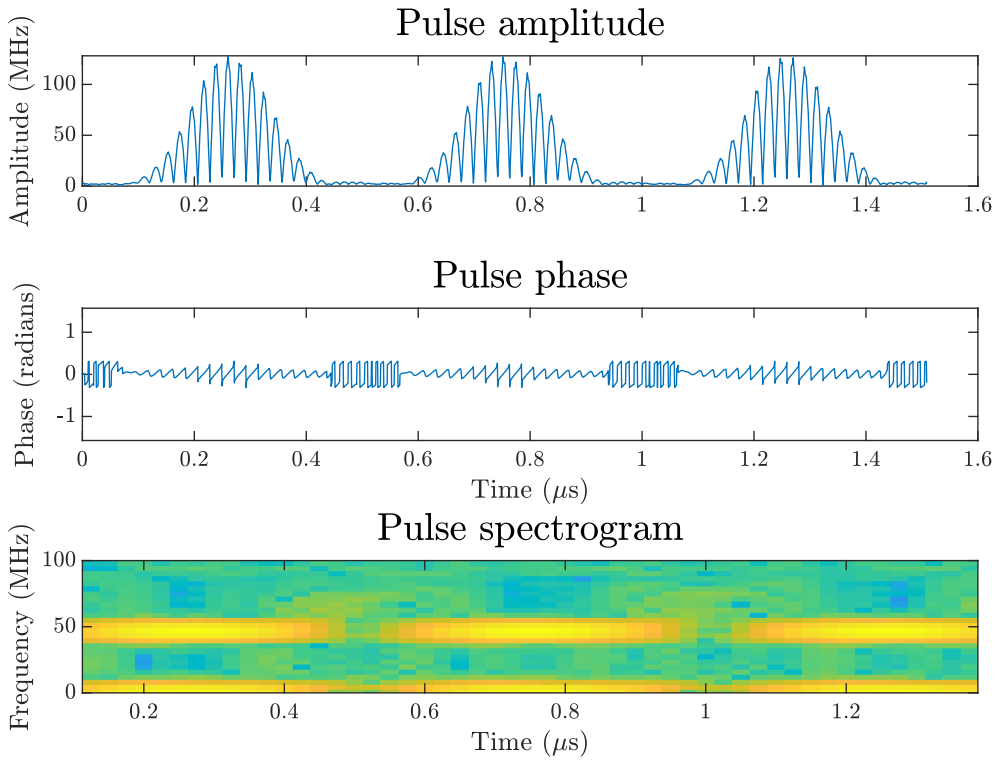

Figure 6.7: Optimised pulse solution with unconstrained Rabi frequency for performing a NOT gate in a 100 kHz ensemble system at the 8T field value. This optimised sequence gave an error value of 0.00091. The Rabi frequency displayed is relative to a resonant transition with a unit relative oscillator strength. Large Rabi frequencies can be used in this solution without driving neighbouring hyperfine levels due to small relative oscillator strengths for non-computing levels and hyperfine spacings of tens of MHz. This results in transitions other than the computing transitions experiencing small generalised Rabi frequencies.

Following the full optimisation sequence, the QGE of the unconstrained arbitrary pulse was 0.00235, which is 37% lower than the error of 0.0037 achieved using an optimised Gaussian pulse. For the purpose of comparison, a two-colour Gaussian pulse implementing the same gate operation was optimised. This pulse sequence was found to have a minimum QGE of 0.0029, 23% higher than the arbitrary sequence. The shape of two-colour Gaussian pulses is very similar to this optimised solution, with the optimised pulses slightly narrower in the time domain. The narrower time-domain profile slightly reduces the QGE due to decoherence while increasing the QGE due to off-resonant excitation of other hyperfine levels. In this specific case, this results in a net decrease in QGE.

In the case of a pulse constrained to a Rabi frequency of 10 MHz, the optimised error value was 0.014. This optimised pulse is displayed in Figure 6.6. The error of this constrained pulse is higher than the error for a Gaussian pulse displayed in Table 6.1 as the Rabi frequency of those pulses was unconstrained, with the Gaussian pulse

example using Rabi frequencies of 47.4 MHz and 28.7 MHz for the $|0\rangle \leftrightarrow |e\rangle$ and $|1\rangle \leftrightarrow |e\rangle$ transitions respectively. The amplitude and phase noise on these optimised sequences is visibly much lower than in the single-instance pulses. The remaining oscillation that can be seen on the phase noise is due to the time discretisation of these optimised pulses and driving the $EuCl_3{\cdot}6D_2O$ system in this manner is not advantageous.

The convergence of the Krotov optimisation was dependent on the initial guess solution. For initial guesses that were insufficiently smooth, the optimisation failed to converge to the discrete pulses seen in Figures 6.5 and 6.4, converging instead on solutions with oscillation over the entire time window. These apparent solutions were found to be a consequence of the way that the optimisation was discretised. Discretisation was identified as the source of these erroneous solutions by doubling the simulation time step and interpolating the driving field over this new interval - with this smaller time step, the QGE increased by orders of magnitude.

Figure 6.8 shows an example of these erroneous solutions. In order to avoid these erroneous solutions, a spline interpolation was used to define a smooth starting condition. Twenty random Rabi frequencies with a maximum frequency of 10 MHz were generated at an evenly spaced time interval in the 20μs window and a spline interpolation was then used to define the initial driving field.

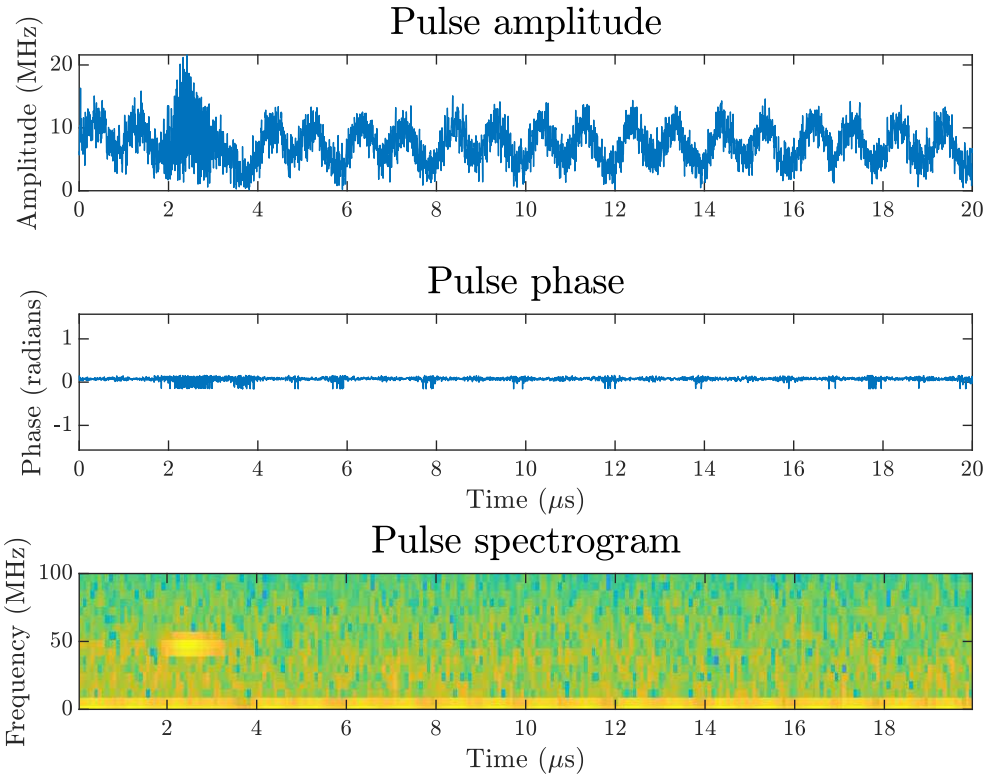

Figure 6.8: Example of erroneous solutions that arise when the initial conditions of the Krotov optimisation are rapidly varying.

The modest reduction in QGE of the optimised pulse sequence as compared to both regular Gaussian pulses (0.0037) and two-colour Gaussian pulses (0.0029) indicates that the potential benefit from implementing sophisticated pulse schemes in this system is limited. In $EuCl_3 \cdot 6D_2O$, QGE is primarily limited by optical decoherence over the course of the pulse rather than the properties of the specific pulses used to drive the system. Substantial decreases in error in rare-earth satellite systems are likely to come from identifying systems with more favourable properties instead of optimising the operation of current systems.

6.4 Gate modifications

In addition to optimising the performance of the constituent pulses used to perform quantum gates, the sequence of pulses itself can be modified to account for system properties. A quantum gate dictates an action on a quantum state and does not specify how the action is implemented. To implement a quantum gate, a sequence of more basic system operations are applied to the system. In a naive implementation of a quantum circuit, the action of each gate is considered separately from the rest of the circuit, with all of the underlying operations for each gate applied. Applying each gate without consideration for the rest of the circuit could result in potentially suboptimal operation because there may be redundant operations, or operations may be able to run in parallel. The optimisation of quantum gate sequences so as to minimise the size of the quantum circuit is a well-studied area [138–142], with demonstrations of the implementation of these compiled sequences [143, 144].

As an example of pulse optimisation in a rare-earth system, we will consider the ensemble three-qubit bit-flip correction sequence, introduced in Chapter 3. A direct implementation of this sequence requires 27 pulses, with eleven on the data qubit and eight on each of the ancilla qubits. The circuit diagram for this three-qubit code is given in the following circuit diagram:

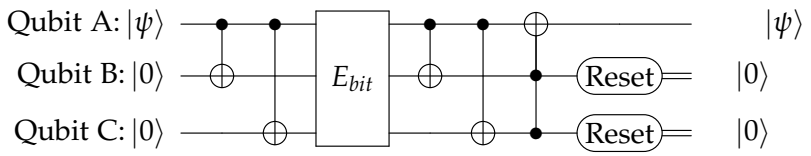

If the three-qubit code is decomposed into the applied π pulses, we arrive at the pulse sequence given in Figure 6.9.

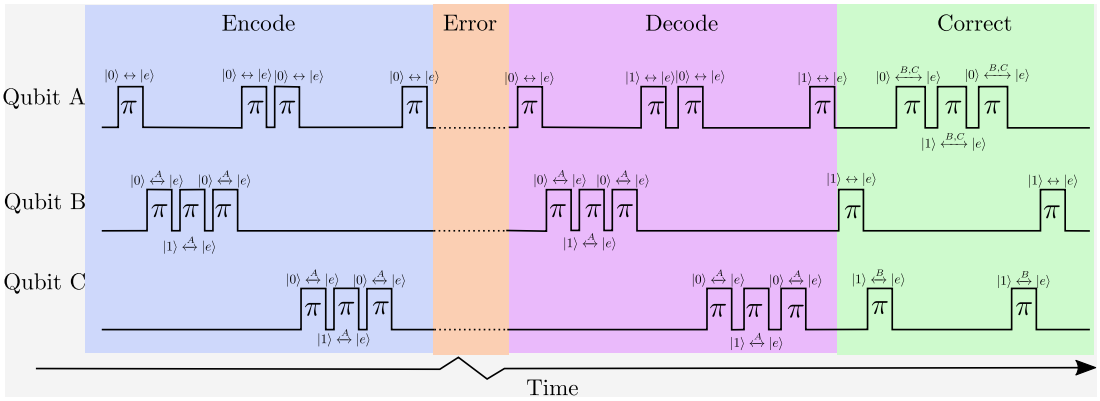

Figure 6.9: Pulse sequence to implement the three-qubit bit-flip protocol. Qubit A is the memory qubit and Qubits B and C are the ancilla qubits. Overset letters are used to indicate shifted transitions. For example, a $|1\rangle \overset{A}{\leftrightarrow} |e\rangle$ pulse on qubit B means the $|1\rangle \leftrightarrow |e\rangle$ transition driven at the resonant frequency when qubit A is excited.

The first optimisation that can be made in this pulse sequence is to reduce the number of pulses used for the controlled gates on the ancilla qubits. At the beginning of this sequence, the ancilla qubits are in the $|0\rangle$ state and, hence, in the initial CNOT gates on Qubits B and C, only the $|0\rangle \overset{A}{\leftrightarrow} |e\rangle$, $|1\rangle \overset{A}{\leftrightarrow} |e\rangle$ pulses are needed. These two CNOT gates can be modified further by combining them to remove the two pulses that return the data qubit to the ground-state and then immediately excite it again. A similar analysis allows for a reduction in the number of pulses needed in the decoding stage of the algorithm. The final modification that we can make is removing the $|0\rangle \leftrightarrow |e\rangle$ pulses applied to the ancilla qubits during the correction phase, as these qubits will be reset following the conclusion of this sequence. The resulting 17 pulse sequence, which was first introduced in Chapter 5, is displayed again in Figure 6.10

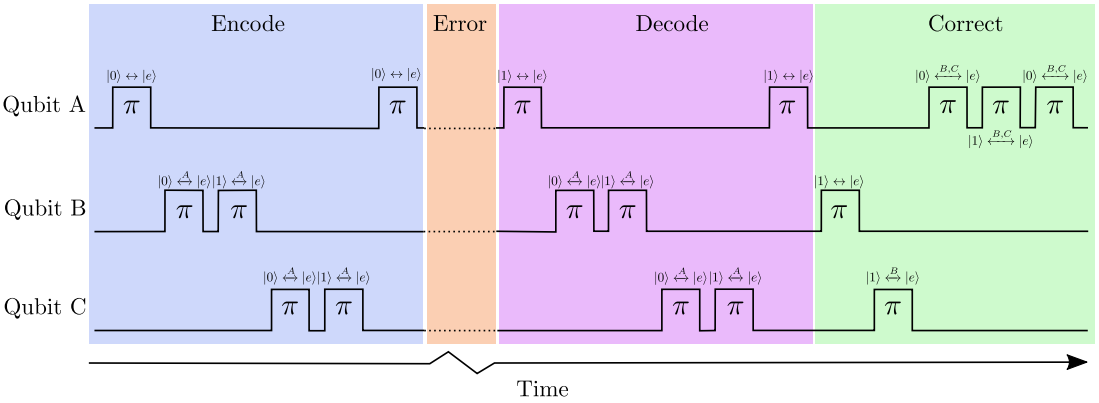

Figure 6.10: Three-qubit bit-flip protocol with the number of pulses applied to qubits minimised. Qubit A is the memory qubit and Qubits B and C are the ancilla qubits. Figure reproduced from [96].

This simple example provides only a demonstration of the optimisations that

can be performed for a rare-earth system. The choice for the satellite feature that corresponds to each qubit in the quantum circuit will also make a difference to the error in this system. The implementation of controlled gates in the $EuCl_3{\cdot}6D_2O$ relies on a shift in optical transition frequency from optical excitation of nearby qubits. The size of this optical qubit shift depends on the position of the ion relative to the excited qubit. To minimise error, it is desirable to choose qubits such that qubit pairs that have a controlled gate applied to them have a large optical shift that is not close in frequency to any of the other hyperfine levels in either ion.

To demonstrate the effect of qubit choice, the error due to exciting off-resonant qubit states when performing the 17 π pulse bit-flip sequence was simulated for the known satellite lines [97]. It was found that systems using the D satellite as the data qubit with I, J satellites as the ancillas and J as the data qubit with B, D as the ancillas had the lowest error, with errors of 1.7×10^{-3} and 1.5×10^{-3} respectively. The error due to exciting states that are not resonant is significantly lower for this correction sequence than the single-qubit error rates of 3.7×10^{-3} and 2.4×10^{-3} seen in the Gaussian and optimised cases, respectively. This indicates that the single-qubit error rate is the dominant source of error in this system. Figure 6.11 displays the error due to off-resonant excitation of qubit transitions for different possible satellite detunings.

There are other potential considerations for the assignment of system qubits and the applied optical pulses. One such consideration is whether multi-qubit systems exhibit an increased decoherence rate, as is commonly seen in the NMR literature [145]. Additionally, it has not been confirmed that satellite lines all have the same coherence time. To determine whether there are additional multi-qubit decay processes and if satellites exhibit different coherence times will require additional characterisation of this system, with no such measurements having been taken to date.

In addition to the optical inhomogeneous broadening on system qubits, there is $\mathcal{O}(5\text{kHz})$ of broadening on the hyperfine transitions [21]. The broadening of the hyperfine transitions will lead to ions in the system qubits dephasing over time. In order to perform quantum operations, the superposition state must be the same across the ensemble, so the ensemble must be rephased prior to performing gate operations. Rephasing pulses do not require conditional logic, so they may be performed via a direct RF pulse. In systems with more than a single qubit, the constituent ions of multiple qubits must be rephased. The hyperfine frequencies of satellite qubits differ by $\mathcal{O}(0.5\text{ MHz})$ which precludes using a single frequency RF pulse to rephase all qubits simultaneously, as such a pulse would have to have a $\mathcal{O}(20\text{ MHz})$ Rabi frequency, which would cause significant off-resonant excitation to other hyperfine levels. Rephasing of multiple qubits could be achieved by two methods, either sequential rephasing of qubits or the use of a spectrally tailored pulse optimised to drive every qubit equally. In a sequential rephasing scheme, rephasing pulses would be applied sequentially to each of the relevant satellite site hyperfine transitions. The pulses in such a scheme would have a low Rabi frequency (50 KHz or less) so as to avoid driving of other satellite sites. In a spectrally tailored pulse scheme, a single pulse would be applied with frequency components targeting all relevant

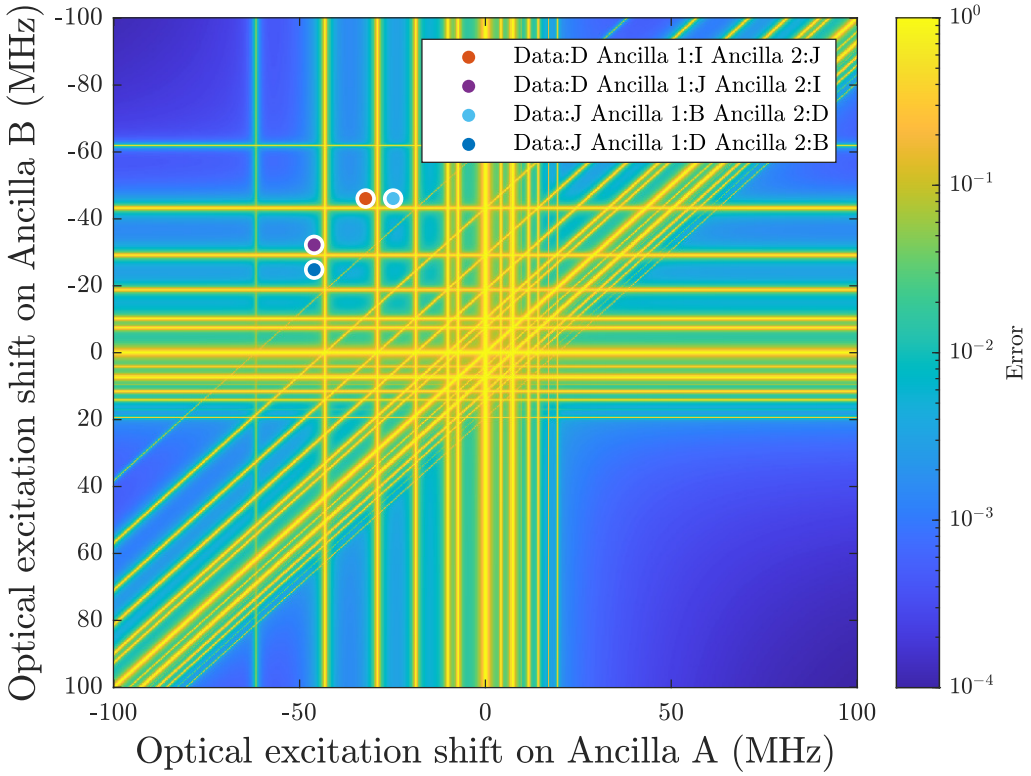

Figure 6.11: Error due to off-resonant excitation of ancilla qubits when performing controlled gates in the 17π pulse error correction sequence. The error when performing a CNOT gate is high for optical interaction shifts that are small or close to other hyperfine transitions due to off-resonant excitation. The satellite line combinations with the four lowest errors are displayed as dots.

hyperfine frequencies. The magnitudes of the frequency components of such a pulse would be selected so as to equally drive all of the relevant transitions. The Rabi frequencies needed for such a pulse scheme will ultimately depend on the number of satellite qubits and the hyperfine structure, however would still be at most $\mathcal{O}(100KHz)$. Use of a multi-frequency tailored pulse has the potential to enable more complete rephasing of the multi-qubit system, as the qubits do not have time to independently dephase between pulses, however this comes at the expense of increased complexity. One potential avenue for finding such a tailored optical pulse may be the use of neural network techniques similar to those used in [146] for the initialisation of a magneto-optical trap.

6.5 Summary

This chapter discussed the manipulation of the optical driving fields and pulse sequences so as to minimise the error of quantum processes in this system. Of the

standard pulse types used to drive this system, it was found that Gaussian pulses gave the lowest error for implementation of a NOT gate, with a QGE of 0.58 at zero-field and 0.0037 at the 8T point.

The use of compensated pulses to evenly drive an ensemble was then investigated and simulations were performed comparing the performance of a compensated pulse under the Roos and Mølmer dark-state scheme to direct Gaussian pulses. It was found that this scheme does not give an advantage over direct Gaussian pulses for the ensemble widths that were considered (< 250 kHz), with the compensated pulse giving an approximately three times greater error even with an ensemble width of 250 kHz.

The use of arbitrary pulse shapes in this system was investigated and it was found that a QGE of 2.4×10^{-3} could be achieved at the 8T point using an optimised sequence. This is approximately 37% lower than the error that can be obtained with an optimised Gaussian pulse and indicates that the use of optimised pulse shapes is of moderate importance when performing quantum computing.

This was followed by a discussion of the ways that the pulse sequences used to implement quantum circuits can be modified to reduce the number of pulses and total execution time. The importance of considering qubit-qubit interaction strengths in satellite systems was then discussed, with a demonstration of error rates for different qubit interaction shifts when implementing a bit-flip code. The chapter concluded with a discussion on the need to perform RF rephasing pulses in this system due to the hyperfine broadening and potential routes for optimisation of these pulses.

This chapter has implications for how to efficiently drive a $EuCl_3{\cdot}6D_2O$ system for quantum computing demonstrations. A low QGE can be accomplished using purely Gaussian pulse shapes, although there is some benefit to using optimised pulse sequences. There appears to be no benefit to driving transitions other than the $|0\rangle \leftrightarrow |e\rangle$ and $|1\rangle \leftrightarrow |e\rangle$ transitions for the purposes of performing quantum gates. Lower QGE is possible using very high Rabi frequencies, with acceptable performance using Rabi frequencies accessible using standard dye lasers. Broadening on the hyperfine transition causes dephasing between members of the ensemble between pulses and during storage of quantum states. Due to this, it will be necessary to apply RF rephasing pulses before every application of an optical gate. The choice of satellite lines in a computing system is also important to consider, with satellites needing to be chosen such that the optical transition shift used during a controlled gate is not close to any of the hyperfine levels. Only a small number of satellite interactions have been measured to date and more measurements of the satellite interactions will need to be obtained before definitive statements can be made as to the best choice of satellite lines.

Chapter 7

Conclusion

Quantum computing has the potential to make the solution of several classes of problems possible, which have been intractable on classical computers. An essential component of any future large quantum computing system will be the ability to perform reliable error correction during computation and storage. Implementation of reliable error correction requires knowledge of the kinds of errors that can occur to a computing system. One potential tool for studying real-world errors in a quantum system is a small quantum processor with a low error rate. Stoichiometric rare-earth ion systems are one potential candidate for the construction of such a small quantum processor.

This thesis investigated the implementation of quantum computing in stoichiometric rare-earth systems, using $EuCl_3{\cdot}6D_2O$ as an example system. The manipulation of system parameters and implementation of quantum operations were examined in order to develop a guide to the regimes necessary for the implementation of quantum computing in $EuCl_3{\cdot}6D_2O$ and other stoichiometric rare-earth systems.

At zero-field, the oscillator strengths of $EuCl_3{\cdot}6D_2O$ are too unequal to be able to perform low error quantum operations, with one of the transitions between the ground hyperfine and excited optical state necessarily having a very high error. The oscillator strengths and hyperfine splittings of $EuCl_3{\cdot}6D_2O$ can be manipulated to be closer to an ideal Λ system through the application of magnetic fields. Through the use of an 8T magnetic field, a bit-flip error correction sequence can potentially be implemented with an error as low as 0.022. However, fields as low as 2T can also be utilised to substantially improve the computing system, with an error of 0.065 the lowest possible sequence error below 2T. For applied fields of $<\approx$ 15T the ^{151}Eu isotope is preferable for computing applications as it has larger Zeeman coefficients and, hence, the potential for better state mixing. For fields $>\approx$ 15T, the larger hyperfine splittings of ^{153}Eu lead to lower QGE.

It was established that standard Gaussian pulses are sufficient to perform low error quantum gates. The QGE can be reduced by $\approx 37\%$ through the use of optimised pulses of an arbitrary shape. There appears to be no benefit of driving transitions other than the $|0\rangle \leftrightarrow |e\rangle$ and $|1\rangle \leftrightarrow |e\rangle$ transitions, with the optimised sequences driving only these frequencies.

There is $\mathcal{O}(5\text{kHz})$ broadening on the hyperfine transitions in $EuCl_3{\cdot}6D_2O$ which will lead to dephasing of members of the ensemble; as such, it is advisable that RF

rephasing gates are applied before application of any optical gate to this system. This will require individually driving the unique RF transitions between the computing levels for each of the satellite lines in this system. In addition to the need to rephase individual satellite RF transitions, the choice of satellite lines can have a large effect on the system error. As demonstrated in Section 6.4 qubits must be chosen such that satellite line shifts do not overlap with resonant qubit transitions; otherwise, qubit states that were supposed to be non-resonant will be driven, greatly increasing the error when quantum gates are applied. The current measurements of satellite interactions in $EuCl_3 \cdot 6D_2O$ are incomplete, and further research will need to be undertaken before a definitive choice of satellite lines with the lowest error can be made.

It was determined that the QGE in europium systems is fundamentally limited by the size of the europium hyperfine splitting relative to the optical coherence time. The rare-earth species erbium and holmium were proposed for computing due to their large hyperfine structure, and it was established that there is potential for up to a 100-fold reduction in QGE by moving to these host ions. These materials have largely not been studied at stoichiometric concentrations, and so much further research is needed to determine if satellite quantum computing can be performed using these rare-earth ions.

This thesis has shown that stoichiometric $EuCl_3 \cdot 6D_2O$ has potential as a testbed system for implementing quantum logic in a rare-earth system. The rare-earths have traditionally been seen as a system for purely quantum memory applications, with quantum computing the domain of single-instance systems such as superconducting microwave qubits. It is hoped that this thesis will begin to change the conventional wisdom of what is possible in rare-earth systems.

Bibliography

[1] G. Kirchoff, "Abhandlungen über emission und absorption", W. Engelmann **1** (1898).

[2] L. Boltzmann, *Über die Beziehung zwischen dem zweiten Hauptsatze des mechanischen Wärmetheorie und der Wahrscheinlichkeitsrechnung, respective den Sätzen über das Wärmegleichgewicht* (Kk Hof-und Staatsdruckerei, 1877).

[3] H. Hertz, "Ueber einen Einfluss des ultravioletten Lichtes auf die electrische Entladung", Annalen der Physik **267**, 983–1000 (1887).

[4] M. Planck, "On the theory of the energy distribution law of the normal spectrum", Verhandlungen der Deutschen Physikalischen Gesellschaft **2**, 237–245 (1900).

[5] A. Einstein, "Über einem die Erzeugung und Verwandlung des Lichtes betreffenden heuristischen Gesichtspunkt", Annalen der Physik **4** (1905).

[6] L. d. Broglie, "Ondes et quanta", Comptes rendus **177**, 507–510 (1923).

[7] L. d. Broglie, "Quanta de lumiére, diffraction et interférences", Comptes rendus **177**, 548–551 (1923).

[8] L. d. Broglie, "Les quanta, la théorie cinétique des gaz et le principe de Fermat", Comptes rendus **177**, 630–632 (1923).

[9] R. P. Feynman, "Simulating physics with computers", International Journal of Theoretical Physics **21**, 467–488 (1982).

[10] P. Shor, "Algorithms for quantum computation: discrete logarithms and factoring", in Proceedings 35th Annual Symposium on Foundations of Computer Science (1994), pp. 124–134.

[11] P. W. Shor, "Scheme for reducing decoherence in quantum computer memory", Physical Review A **52**, R2493 (1995).

[12] C. H. Bennett, F. Bessette, G. Brassard, L. Salvail, and J. Smolin, "Experimental quantum cryptography", Journal of Cryptology **5**, 3–28 (1992).

[13] P. W. Shor, "Polynomial-time algorithms for prime factorization and discrete logarithms on a quantum computer", SIAM review **41**, 303–332 (1999).

[14] L. K. Grover, "Quantum mechanics helps in searching for a needle in a haystack", Physical Review Letters **79**, 325 (1997).

[15] F. Arute et al., "Quantum supremacy using a programmable superconducting processor", Nature **574**, 505–510 (2019).

[16] T. Patel, B. Li, R. B. Roy, and D. Tiwari, "UREQA: Leveraging Operation-Aware Error Rates for Effective Quantum Circuit Mapping on NISQ-Era Quantum Computers", in 2020 USENIX Annual Technical Conference (USENIX ATC 20) (July 2020), pp. 705–711.

[17] L. Rippe, M. Nilsson, S. Kröll, R. Klieber, and D. Suter, "Experimental demonstration of efficient and selective population transfer and qubit distillation in a rare-earth-metal-ion-doped crystal", Physical Review A **71**, 062328 (2005).

[18] L. Rippe, B. Julsgaard, A. Walther, Y. Ying, and S. Kröll, "Experimental quantum-state tomography of a solid-state qubit", Physical Review A **77**, 022307 (2008).

[19] Y. Yan, C. Shi, A. Kinos, H. Syed, S. Horvath, A. Walther, L. Rippe, X. Chen, and S. Kröll, "Experimental implementation of precisely tailored light-matter interaction via inverse engineering", arXiv preprint arXiv:2101.12461 (2021).

[20] A. Kinos, L. Rippe, S. Kröll, and A. Walther, "Designing gate operations for single ion quantum computing in rare-earth-ion-doped crystals", arXiv preprint arXiv:2108.04498 (2021).

[21] R. Ahlefeldt, "Evaluation of a stoichiometric rare earth crystal for quantum computing", PhD thesis (The Australian National University, 2013).

[22] J. Preskill, "Quantum Computing in the NISQ era and beyond", Quantum **2**, 79 (2018).

[23] M. Kjaergaard, M. E. Schwartz, J. Braumüller, P. Krantz, J. I.-J. Wang, S. Gustavsson, and W. D. Oliver, "Superconducting Qubits: Current State of Play", Annual Review of Condensed Matter Physics **11**, 10.1146/annurev-conmatphys-031119-050605 (2020).

[24] L. DiCarlo, J. M. Chow, J. M. Gambetta, L. S. Bishop, B. R. Johnson, D. Schuster, J. Majer, A. Blais, L. Frunzio, S. Girvin, et al., "Demonstration of two-qubit algorithms with a superconducting quantum processor", Nature **460**, 240–244 (2009).

[25] E. Lucero, R. Barends, Y. Chen, J. Kelly, M. Mariantoni, A. Megrant, P. O'Malley, D. Sank, A. Vainsencher, J. Wenner, et al., "Computing prime factors with a Josephson phase qubit quantum processor", Nature Physics **8**, 719–723 (2012).

[26] M. D. Reed, L. DiCarlo, S. E. Nigg, L. Sun, L. Frunzio, S. M. Girvin, and R. J. Schoelkopf, "Realization of three-qubit quantum error correction with superconducting circuits", Nature **482**, 382–385 (2012).

[27] A. D. Córcoles, E. Magesan, S. J. Srinivasan, A. W. Cross, M. Steffen, J. M. Gambetta, and J. M. Chow, "Demonstration of a quantum error detection code using a square lattice of four superconducting qubits", Nature Communications **6**, 1–10 (2015).

[28] J. Kelly, R. Barends, A. G. Fowler, A. Megrant, E. Jeffrey, T. C. White, D. Sank, J. Y. Mutus, B. Campbell, Y. Chen, et al., "State preservation by repetitive error detection in a superconducting quantum circuit", Nature **519**, 66–69 (2015).

[29] M. Zhong, M. P. Hedges, R. L. Ahlefeldt, J. G. Bartholomew, S. E. Beavan, S. M. Wittig, J. J. Longdell, and M. J. Sellars, "Optically addressable nuclear spins in a solid with a six-hour coherence time", Nature **517**, 177–180 (2015).

[30] M. P. Hedges, J. J. Longdell, Y. Li, and M. J. Sellars, "Efficient quantum memory for light", Nature **465**, 1052–1056 (2010).

[31] K. R. Ferguson, S. E. Beavan, J. J. Longdell, and M. J. Sellars, "Generation of light with multimode time-delayed entanglement using storage in a solid-state spin-wave quantum memory", Physical Review Letters **117**, 020501 (2016).

[32] R. Macfarlane, A. Arcangeli, A. Ferrier, and P. Goldner, "Optical measurement of the effect of electric fields on the nuclear spin coherence of rare-earth ions in solids", Physical Review Letters **113**, 157603 (2014).

[33] N. Ohlsson, R. K. Mohan, and S. Kröll, "Quantum computer hardware based on rare-earth-ion-doped inorganic crystals", Optics communications **201**, 71–77 (2002).

[34] J. Longdell, "Quantum Information Processing in Rare Earth Ion Doped Insulators", PhD thesis (The Australian National University, 2003).

[35] Y. Yan, Y. Li, A. Kinos, A. Walther, C. Shi, L. Rippe, J. Moser, S. Kröll, and X. Chen, "Inverse engineering of shortcut pulses for high fidelity initialization on qubits closely spaced in frequency", Optics Express **27**, 8267–8282 (2019).

[36] A. J. Freeman and R. Watson, "Theoretical investigation of some magnetic and spectroscopic properties of rare-earth ions", Physical Review **127**, 2058 (1962).

[37] G. Liu and B. Jacquier, *Spectroscopic Properties of Rare Earths in Optical Materials* (Springer, 2005), pp. 1–94.

[38] G. Imbusch and R. Kopelman, "Optical spectroscopy of electronic centers in solids", in *Laser spectroscopy of solids* (Springer, 1981), pp. 1–37.

[39] W. Fricke, "Satellite lines in the optical absorption spectra of doped (La, Pr) Cl_3-crystals", Zeitschrift für Physik B Condensed Matter **33**, 261–269 (1979).

[40] R. Cone, R. Harley, and M. Leask, "Nuclear quadrupole optical hole-burning in stoichiometric $EuVO_4$", Journal of Physics C: Solid State Physics **17**, 3101 (1984).

[41] M. Yamaguchi, K. Koyama, T. Suemoto, and M. Mitsunaga, "Mapping of site distribution in Eu^{3+}: $YAlO_3$ on RF-optical frequency axes by using double-resonance spectroscopy", Journal of Luminescence **76**, 681–684 (1998).

[42] M. Yamaguchi, K. Koyama, and T. Suemoto, "Three-parameter mapping of site distribution by optical-RF double resonance in Eu^{3+}:Y_2O_3 crystals", Journal of Luminescence **87-89**, 1099–1101 (2000).

[43] J. P. D. Martin, M. J. Sellars, P. Tuthill, N. B. Manson, G. Pryde, and T. Dyke, "Resolved Isotopic Energy Shift and Hole Burning in $EuCl_3 \cdot 6H_2O$", Journal of Luminescence **78**, 19–24 (1998).

[44] R. Ahlefeldt, M. Zhong, J. Bartholomew, and M. Sellars, "Minimizing Zeeman sensitivity on optical and hyperfine transitions in $EuCl_3 \cdot 6H_2O$ to extend coherence times", Journal of Luminescence **143**, 193–200 (2013).

[45] J. Harrowfield, D. Kepert, J. M. Patrick, and A. H. White, "Structure and stereochemistry in 'f-block' complexes of high coordination number. VIII. The $[M(\text{unidentate})_9]$ system. Crystal structures of $[M(OH_2)_9][CF_3SO_3]_3$, M = La, Gd, Lu, Y", Australian Journal of Chemistry **36**, 483–492 (1983).

[46] R. M. Macfarlane, R. S. Meltzer, and B. Z. Malkin, "Optical measurement of the isotope shifts and hyperfine and superhyperfine interactions of Nd in the solid state", Physical Review B **58**, 5692–5700 (1998).

[47] R. Ahlefeldt, M. R. Hush, and M. Sellars, "Ultranarrow optical inhomogeneous linewidth in a stoichiometric rare-earth crystal", Physical Review Letters **117**, 250504 (2016).

[48] R. Ahlefeldt, N. Manson, and M. Sellars, "Optical lifetime and linewidth studies of the $^7F_0 \rightarrow {}^5D_0$ transition in $EuCl_3 \cdot 6H_2O$: A potential material for quantum memory applications", Journal of Luminescence **133**, 152–156 (2013).

[49] G. W. Robinson, "Spectra and energy transfer phenomena in crystalline rare gas solvents", Journal of Molecular Spectroscopy **6**, 58–83 (1961).

[50] J. L. Kropp and M. W. Windsor, "Enhancement of Fluorescence Yield of Rare-Earth Ions by Heavy Water", The Journal of Chemical Physics **39**, 2769–2770 (1963).

[51] A. Heller, "Formation of hot OH Bonds in the radiationless relaxations of excited rare earth ions in aqueous solutions", Journal of the American Chemical Society **88**, 2058–2059 (1966).

[52] J. Freeman, G. Crosby, and K. Lawson, "The effect of deuterium on the luminescence decay times of solvated rare earth chlorides", Journal of Molecular Spectroscopy **13**, 399–406 (1964).

[53] J. L. Kropp and M. W. Windsor, "Luminescence and energy transfer in solutions of rare-earth complexes. I. Enhancement of fluorescence by deuterium substitution", The Journal of Chemical Physics **42**, 1599–1608 (1965).

[54] G. Stein and E. Würzberg, "Energy gap law in the solvent isotope effect on radiationless transitions of rare earth ions", The Journal of Chemical Physics **62**, 208–213 (1975).

[55] R. Ahlefeldt, D. McAuslan, J. Longdell, N. Manson, and M. Sellars, "Precision Measurement of Electronic Ion-Ion Interactions between Neighboring Eu^{3+} Optical Centers", Physical Review Letters **111**, 240501 (2013).

[56] J. Longdell, M. Sellars, and N. Manson, "Demonstration of conditional quantum phase shift between ions in a solid", Physical Review Letters **93**, 130503 (2004).

[57] Y. Yan, J. Karlsson, L. Rippe, A. Walther, D. Serrano, D. Lindgren, M.-e. Pistol, S. Kröll, P. Goldner, L. Zheng, et al., "Measurement of linewidths and permanent electric dipole moment change of the Ce $4f - 5d$ transition in Y_2SiO_5 for qubit readout scheme in rare-earth ion based quantum computing", Physical Review B **87**, 184205 (2013).

[58] L. Childress, M. G. Dutt, J. Taylor, A. Zibrov, F. Jelezko, J. Wrachtrup, P. Hemmer, and M. Lukin, "Coherent dynamics of coupled electron and nuclear spin qubits in diamond", Science **314**, 281–285 (2006).

[59] M. G. Dutt, L. Childress, L. Jiang, E. Togan, J. Maze, F. Jelezko, A. Zibrov, P. Hemmer, and M. Lukin, "Quantum register based on individual electronic and nuclear spin qubits in diamond", Science **316**, 1312–1316 (2007).

[60] P. Neumann, N. Mizuochi, F. Rempp, P. Hemmer, H. Watanabe, S. Yamasaki, V. Jacques, T. Gaebel, F. Jelezko, and J. Wrachtrup, "Multipartite entanglement among single spins in diamond", Science **320**, 1326–1329 (2008).

[61] D. G. Cory, A. F. Fahmy, and T. F. Havel, "Ensemble quantum computing by NMR spectroscopy", Proceedings of the National Academy of Sciences **94**, 1634–1639 (1997).

[62] N. A. Gershenfeld and I. L. Chuang, "Bulk spin-resonance quantum computation", Science **275**, 350–356 (1997).

[63] F. Yamaguchi and Y. Yamamoto, "Crystal lattice quantum computer", Applied Physics A **68**, 1–8 (1999).

[64] C. Negrevergne, R. Somma, G. Ortiz, E. Knill, and R. Laflamme, "Liquid-state NMR simulations of quantum many-body problems", Physical Review A **71**, 032344 (2005).

[65] H. Bernien, B. Hensen, W. Pfaff, G. Koolstra, M. S. Blok, L. Robledo, T. Taminiau, M. Markham, D. J. Twitchen, L. Childress, et al., "Heralded entanglement between solid-state qubits separated by three metres", Nature **497**, 86–90 (2013).

[66] G. Waldherr, Y. Wang, S. Zaiser, M. Jamali, T. Schulte-Herbrüggen, H. Abe, T. Ohshima, J. Isoya, J. Du, P. Neumann, et al., "Quantum error correction in a solid-state hybrid spin register", Nature **506**, 204–207 (2014).

[67] J. A. Jones, "Quantum computing and nuclear magnetic resonance", PhysChemComm **4**, 49–56 (2001).

[68] H. G. Krojanski and D. Suter, "Scaling of decoherence in wide NMR quantum registers", Physical Review Letters **93**, 090501 (2004).

[69] D. P. DiVincenzo, "The physical implementation of quantum computation", Fortschritte der Physik: Progress of Physics **48**, 771–783 (2000).

[70] W. G. Unruh, "Maintaining coherence in quantum computers", Physical Review A **51**, 992 (1995).

[71] W. K. Wootters and W. H. Zurek, "A single quantum cannot be cloned", Nature **299**, 802–803 (1982).

[72] A. M. Steane, "Error correcting codes in quantum theory", Physical Review Letters **77**, 793 (1996).

[73] A. R. Calderbank and P. W. Shor, "Good quantum error-correcting codes exist", Physical Review A **54**, 1098 (1996).

[74] R. Laflamme, C. Miquel, J. P. Paz, and W. H. Zurek, "Perfect quantum error correcting code", Physical Review Letters **77**, 198 (1996).

[75] C. H. Bennett, D. P. DiVincenzo, J. A. Smolin, and W. K. Wootters, "Mixed-state entanglement and quantum error correction", Physical Review A **54**, 3824 (1996).

[76] J. Johnson, C. Macklin, D. Slichter, R. Vijay, E. Weingarten, J. Clarke, and I. Siddiqi, "Heralded state preparation in a superconducting qubit", Physical Review Letters **109**, 050506 (2012).

[77] R. Barends, J. Kelly, A. Megrant, A. Veitia, D. Sank, E. Jeffrey, T. C. White, J. Mutus, A. G. Fowler, B. Campbell, et al., "Superconducting quantum circuits at the surface code threshold for fault tolerance", Nature **508**, 500–503 (2014).

[78] S. Sheldon, E. Magesan, J. M. Chow, and J. M. Gambetta, "Procedure for systematically tuning up cross-talk in the cross-resonance gate", Physical Review A **93**, 060302 (2016).

[79] S. S. Hong, A. T. Papageorge, P. Sivarajah, G. Crossman, N. Didier, A. M. Polloreno, E. A. Sete, S. W. Turkowski, M. P. da Silva, and B. R. Johnson, "Demonstration of a parametrically activated entangling gate protected from flux noise", Physical Review A **101**, 012302 (2020).

[80] R. Harper, S. T. Flammia, and J. J. Wallman, "Efficient learning of quantum noise", Nature Physics, 1–5 (2020).

[81] J. M. Martinis, "Qubit metrology for building a fault-tolerant quantum computer", npj Quantum Information **1**, 1–3 (2015).

[82] C. Riofrio, D. Gross, S. T. Flammia, T. Monz, D. Nigg, R. Blatt, and J. Eisert, "Experimental quantum compressed sensing for a seven-qubit system", Nature Communications **8**, 1–8 (2017).

[83] J. Chiaverini, D. Leibfried, T. Schaetz, M. D. Barrett, R. Blakestad, J. Britton, W. M. Itano, J. D. Jost, E. Knill, C. Langer, et al., "Realization of quantum error correction", Nature **432**, 602–605 (2004).

[84] T. H. Taminiau, J. Cramer, T. van der Sar, V. V. Dobrovitski, and R. Hanson, "Universal control and error correction in multi-qubit spin registers in diamond", Nature Nanotechnology **9**, 171 (2014).

[85] J. Cramer, N. Kalb, M. A. Rol, B. Hensen, M. S. Blok, M. Markham, D. J. Twitchen, R. Hanson, and T. H. Taminiau, "Repeated quantum error correction on a continuously encoded qubit by real-time feedback", Nature Communications **7**, 1–7 (2016).

[86] D. Riste, S. Poletto, M.-Z. Huang, A. Bruno, V. Vesterinen, O.-P. Saira, and L. DiCarlo, "Detecting bit-flip errors in a logical qubit using stabilizer measurements", Nature Communications **6**, 1–6 (2015).

[87] P. Schindler, J. T. Barreiro, T. Monz, V. Nebendahl, D. Nigg, M. Chwalla, M. Hennrich, and R. Blatt, "Experimental repetitive quantum error correction", Science **332**, 1059–1061 (2011).

[88] M. A. Nielsen and I. L. Chuang, *Quantum computation and quantum information* (Cambridge University Press, Cambridge, 2000).

[89] T. J. Yoder and I. H. Kim, "The surface code with a twist", Quantum **1**, 2 (2017).

[90] R. Chao and B. W. Reichardt, "Quantum error correction with only two extra qubits", Physical Review Letters **121**, 050502 (2018).

[91] N. Ofek, A. Petrenko, R. Heeres, P. Reinhold, Z. Leghtas, B. Vlastakis, Y. Liu, L. Frunzio, S. Girvin, L. Jiang, et al., "Extending the lifetime of a quantum bit with error correction in superconducting circuits", Nature **536**, 441–445 (2016).

[92] T. Monz, P. Schindler, J. T. Barreiro, M. Chwalla, D. Nigg, W. A. Coish, M. Harlander, W. Hänsel, M. Hennrich, and R. Blatt, "14-Qubit Entanglement: Creation and Coherence", Physical Review Letters **106**, 130506 (2011).

[93] G. J. Pryde, M. J. Sellars, and N. B. Manson, "Solid state coherent transient measurements using hard optical pulses", Physical Review Letters **84**, 1152 (2000).

[94] J. H. Wesenberg, "Quantum Information Processing in Rare-Earth-Ion Doped Crystals", PhD thesis (University of Aarhus, 2004).

[95] M. Nilsson, "Coherent interactions in rare-earth-ion-doped crystals for applications in quantum information science", PhD thesis (Lund University, 2005).

[96] R. Ahlefeldt, M. Pearce, M. Hush, and M. Sellars, "Quantum processing with ensembles of rare-earth ions in a stoichiometric crystal", Physical Review A **101**, 012309 (2020).

[97] R. L. Ahlefeldt, W. Hutchison, N. Manson, and M. J. Sellars, "Method for assigning satellite lines to crystallographic sites in rare-earth crystals", Physical Review B **88**, 184424 (2013).

[98] P. C. Nagler, M. A. Greenhouse, S. H. Moseley, B. J. Rauscher, and J. E. Sadleir, "Development of transition edge sensor detectors optimized for single-photon spectroscopy in the optical and near-infrared", in High Energy, Optical, and Infrared Detectors for Astronomy VIII, Vol. 10709, edited by A. D. Holland and J. Beletic (International Society for Optics and Photonics, 2018), pp. 719–727.

[99] A. Walther, L. Rippe, Y. Yan, J. Karlsson, D. Serrano, A. Nilsson, S. Bengtsson, and S. Kröll, "High-fidelity readout scheme for rare-earth solid-state quantum computing", Physical Review A **92**, 022319 (2015).

[100] M. Raha, S. Chen, C. M. Phenicie, S. Ourari, A. M. Dibos, and J. D. Thompson, "Optical quantum nondemolition measurement of a single rare earth ion qubit", Nature Communications **11**, 1–6 (2020).

[101] J. M. Kindem, A. Ruskuc, J. G. Bartholomew, J. Rochman, Y. Q. Huan, and A. Faraon, "Control and single-shot readout of an ion embedded in a nanophotonic cavity", Nature **580**, 201–204 (2020).

[102] M. Yamaguchi, K. Koyama, T. Suemoto, and M. Mitsunaga, "Perturbed ion sites in Eu^{3+}: $YAlO_3$ studied by optical-rf double-resonance spectroscopy", Physical Review B **59**, 9126 (1999).

[103] T. Izawa, N. Shibata, and A. Takeda, "Optical attenuation in pure and doped fused silica in the IR wavelength region", Applied Physics Letters **31**, 33–35 (1977).

[104] P. Siyushev, K. Xia, R. Reuter, M. Jamali, N. Zhao, N. Yang, C. Duan, N. Kukharchyk, A. Wieck, R. Kolesov, et al., "Coherent properties of single rare-earth spin qubits", Nature Communications **5**, 1–6 (2014).

[105] J. H. Wesenberg, K. Mølmer, L. Rippe, and S. Kröll, "Scalable designs for quantum computing with rare-earth-ion-doped crystals", Physical Review A **75**, 012304 (2007).

[106] J. Wesenberg and K. Moelmer, "Robust quantum gates and a bus architecture for quantum computing with rare-earth-ion-doped crystals", Physical Review A **68**, 012320 (2003).

[107] K. Debnath, A. H. Kiilerich, and K. Mølmer, "Ancilla-mediated qubit readout and heralded entanglement between rare-earth dopant ions in crystals", Physical Review A **103**, 043705 (2021).

[108] L. Allen and J. H. Eberly, *Optical resonance and two-level atoms* (Wiley, New York, 1975).

[109] P. Goldner and O. Guillot-Noël, "Magnetic interactions in Pr^{3+}: $LiYF_4$ for quantum manipulation: search for an efficient three-level Λ system", Molecular Physics **102**, 1185–1192 (2004).

[110] P. Goldner and O. Guillot-Noël, "Magnetic interactions in Pr^{3+} and Tm^{3+} doped crystals for quantum manipulation", Optical Materials **28**, 21–25 (2006).

[111] J. Almlöf and G. Björk, "Fidelity as a figure of merit in quantum error correction", Quantum Information & Computation **13**, 9–20 (2013).

[112] Y. R. Sanders, J. J. Wallman, and B. C. Sanders, "Bounding quantum gate error rate based on reported average fidelity", New Journal of Physics **18**, 012002 (2015).

[113] C. A. Fuchs and J. Van De Graaf, "Cryptographic distinguishability measures for quantum-mechanical states", IEEE Transactions on Information Theory **45**, 1216–1227 (1999).

[114] H.-P. Breuer and F. Petruccione, *The Theory of Open Quantum Systems* (Oxford, Jan. 2006).

[115] J. G. Bartholomew, R. L. Ahlefeldt, and M. J. Sellars, "Engineering closed optical transitions in rare-earth ion crystals", Physical Review B **93**, 014401 (2016).

[116] R. Yano, M. Mitsunaga, and N. Uesugi, "Nonlinear laser spectroscopy of Eu^{3+}:Y_2SiO_5 and its application to time-domain optical memory", JOSA B **9**, 992–997 (1992).

[117] C. Gorller-Walrand, K. Binnemans, and L. Fluyt, "Crystal-field analysis of Eu^{3+} in $LiYF_4$", Journal of Physics: Condensed Matter **5**, 8359 (1993).

[118] R. W. Equall, Y. Sun, R. Cone, and R. Macfarlane, "Ultraslow optical dephasing in Eu^{3+}:Y_2SiO_5", Physical Review Letters **72**, 2179 (1994).

[119] R. W. Equall, R. L. Cone, and R. M. Macfarlane, "Homogeneous broadening and hyperfine structure of optical transitions in Pr^{3+}:Y_2SiO_5", Physical Review B **52**, 3963–3969 (1995).

[120] C. Thiel, T. Böttger, and R. Cone, "Rare-earth-doped materials for applications in quantum information storage and signal processing", Journal of Luminescence **131**, 353–361 (2011).

[121] M. Rančić, M. P. Hedges, R. L. Ahlefeldt, and M. J. Sellars, "Coherence time of over a second in a telecom-compatible quantum memory storage material", Nature Physics **14**, 50–54 (2018).

[122] H. Rahman, "Optical intensities of trivalent erbium in various host lattices", Journal of Physics C: Solid State Physics **5**, 306 (1972).

[123] T. Böttger, C. Thiel, R. Cone, and Y. Sun, "Effects of magnetic field orientation on optical decoherence in Er^{3+}: Y_2SiO_5", Physical Review B **79**, 115104 (2009).

[124] M. Berrington, Personal Communication, 2021.

[125] G. Matmon, S. A. Lynch, T. F. Rosenbaum, A. J. Fisher, and G. Aeppli, "Optical response from terahertz to visible light of electronuclear transitions in $LiYF_4$: Ho^{3+}", Physical Review B **94**, 205132 (2016).

[126] J.-P. R. Wells, G. D. Jones, M. F. Reid, M. N. Popova, and E. P. Chukalina, "Hyperfine patterns of infrared absorption lines of Ho^3+ C_{4v} centres in CaF_2", Molecular Physics **102**, 1367–1376 (2004).

[127] J. Pelzl, S. Hüfner, and S. Scheller, "Hyperfine structure in holmium ethylsulfate and holmium trichloride", Zeitschrift für Physik A Hadrons and nuclei **231**, 377–396 (1970).

[128] D. S. P. Bunbury, C. Carboni, and M. McCausland, "Field dependence of the hyperfine splitting of holmium in holmium hydroxide", Journal of Physics: Condensed Matter **1**, 1309 (1989).

[129] D. P. McLeod and M. F. Reid, "Intensities of hyperfine transitions of Pr^{3+} and Ho^{3+} in CaF_2", Journal of Alloys and Compounds **250**, 302–305 (1997).

[130] R. M. Macfarlane, "High-resolution laser spectroscopy of rare-earth doped insulators: a personal perspective", Journal of Luminescence **100**, 1–20 (2002).

[131] N. Agladze and M. Popova, "Hyperfine structure in optical spectra of $LiYF_4$-Ho", Solid State Communications **55**, 1097–1100 (1985).

[132] M. Weber, B. Matsinger, V. Donlan, and G. Surratt, "Optical transition probabilities for trivalent holmium in LaF_3 and $YAlO_3$", The Journal of Chemical Physics **57**, 562–567 (1972).

[133] E. Baldit, K. Bencheikh, P. Monnier, S. Briaudeau, J. Levenson, V. Crozatier, I. Lorgeré, F. Bretenaker, J. Le Gouët, O. Guillot-Noël, et al., "Identification of Λ-like systems in Er^{3+}:Y_2SiO_5 and observation of electromagnetically induced transparency", Physical Review B **81**, 144303 (2010).

[134] S. L. McCall and E. L. Hahn, "Self-Induced Transparency", Physical Review **183**, 457–485 (1969).

[135] M. H. Levitt, "Composite pulses", Progress in Nuclear Magnetic Resonance Spectroscopy **18**, 61–122 (1986).

[136] I. Roos and K. Mølmer, "Quantum computing with an inhomogeneously broadened ensemble of ions: Suppression of errors from detuning variations by specially adapted pulses and coherent population trapping", Physical Review A **69**, 022321 (2004).

[137] O. V. Morzhin and A. N. Pechen, "Krotov method for optimal control of closed quantum systems", Russian Mathematical Surveys **74**, 851–908 (2019).

[138] M. Amy, D. Maslov, and M. Mosca, "Polynomial-time T-depth optimization of Clifford+ T circuits via matroid partitioning", IEEE Transactions on Computer-Aided Design of Integrated Circuits and Systems **33**, 1476–1489 (2014).

[139] Y. Nam, N. J. Ross, Y. Su, A. M. Childs, and D. Maslov, "Automated optimization of large quantum circuits with continuous parameters", npj Quantum Information **4**, 1–12 (2018).

[140] D. Maslov, G. W. Dueck, D. M. Miller, and C. Negrevergne, "Quantum circuit simplification and level compaction", IEEE Transactions on Computer-Aided Design of Integrated Circuits and Systems **27**, 436–444 (2008).

[141] A. K. Prasad, V. V. Shende, I. L. Markov, J. P. Hayes, and K. N. Patel, "Data structures and algorithms for simplifying reversible circuits", ACM Journal on Emerging Technologies in Computing Systems (JETC) **2**, 277–293 (2006).

[142] M. Saeedi and I. L. Markov, "Synthesis and optimization of reversible circuits—a survey", ACM Computing Surveys (CSUR) **45**, 1–34 (2013).

[143] K. Wright, K. Beck, S. Debnath, J. Amini, Y. Nam, N. Grzesiak, J.-S. Chen, N. Pisenti, M. Chmielewski, C. Collins, et al., "Benchmarking an 11-qubit quantum computer", Nature Communications **10**, 1–6 (2019).

[144] N. M. Linke, D. Maslov, M. Roetteler, S. Debnath, C. Figgatt, K. A. Landsman, K. Wright, and C. Monroe, "Experimental comparison of two quantum computing architectures", Proceedings of the National Academy of Sciences **114**, 3305–3310 (2017).

[145] A. Kumar, R. C. R. Grace, and P. Madhu, "Cross-correlations in NMR", Progress in Nuclear Magnetic Resonance Spectroscopy **37**, 191–319 (2000).

[146] A. D. Tranter, H. J. Slatyer, M. R. Hush, A. C. Leung, J. L. Everett, K. V. Paul, P. Vernaz-Gris, P. K. Lam, B. C. Buchler, and G. T. Campbell, "Multiparameter optimisation of a magneto-optical trap using deep learning", Nature Communications **9**, 1–8 (2018).